IJCESEN

ISSN : 2149-9144

International Journal of Computational and Experimental Science and ENgineering

ijcesen@gmail.com

dergipark.ulakbim.gov.tr/ijcesen

Founder-Editor-in-Chief : Prof.Dr. İskender AKKURT

Volume: 2 - No:1 - 2016

Preface

I am happy that *International Journal of Computational and Experimental Science and Engineering (IJCESEN)* published its third issue (2-1;2016). There are 10 papers in this issue. All manuscripts were subjected to the peer review procedure. We appreciate all the authors and reviewers for their valuable contribution in order to achieve a publication of high scientific quality.

Prof.Dr. İskender AKKURT
Founder-Editor-in-Chief

Table of contents

International Journal of Computational and Experimental Science and Engineering (IJCESEN)
Vol. 2-No.1 (2016) pp. 1-3
http://dergipark.ulakbim.gov.tr/ijcesen

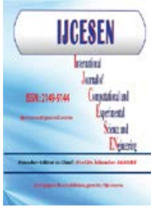

***ISSN:* 2149-9144**

Copyright © IJCESEN

Research Article

Fabrications of Surface Plasmon Resonance (SPR) on Tapered Fiber Structure for Optical Sensor[#]

Nina Siti Aminah[1]*, Rahmat Hidayat[2] and Mitra Djamal[1,3]

[1]Theoretical High Energy Physics and Instrumentation Research Group, Institut Teknologi Bandung, Indonesia
[2]Magnetic and Photonics Physics Group, Institut Teknologi Bandung, Indonesia
[3]Institut Teknologi Sumatera, Lampung, Indonesia

* Corresponding Author : nina@fi.itb.ac.id

[#] Presented in "2nd International Conference on Computational and Experimental Science and Engineering (ICCESEN-2015)"

Keywords
Fiber optic sensors
Surface plasmon resonance
Taper

Abstract: Improvement of tapered fiber sensor by introducing gold thin layer for facilitating surface plasmon resonance (SPR) generation has been studied. The particular interest in this problem is the conditions that determine the formation of evanescent field and the interrogation of the transmission intensity change due to the evanescent field absorption. The fabrication of the tapered fiber was conducted by a technique based on flame brushing using a homemade fiber tapering rig. The heat source comes from an oxy-butane torch. The gold nanolayer was then deposited onto the surface of tapered fiber by sputtering technique. The results suggest that a compact sensor based on this structure may be useful for biochemical sensors.

1. Introduction

Surface Plasmon Resonance (SPR) is a common method for the analysis of biomolecular interaction. SPR is sensitive to the changes in the refractive index occurring at the interface between a thin metal film and a dielectric medium. Binding events are detected as changes in the solute concentration in proximity to the sensor surface, e.g. for binding to a surface immobilized protein. Surface plasmon resonance takes place if the wave vector of the incident light parallel to the conductor surface k_x matches the wave vector of the surface plasmon k_{sp}, whereas the wave vector of the surface plasmon k_{sp} is sensitive to the refractive index of the dielectric medium in contact with the sensor surface[1]. Therefore the wave vector of the light k_x can be approximated by

$$K_{SP} = \frac{\omega}{c}\left(\frac{\varepsilon_m \varepsilon_s}{\varepsilon_m + \varepsilon_s}\right)^{1/2} \quad (1)$$

where ε_s is the dielectric constants of the dielectric medium, whereas ε_m is the real part of the dielectric permittivity of the metal. If excitation of surface plasmons occurs, it will resulting a dip in the intensity of the reflected light. Therefore, this dip varies approximately with the refractive index of the dielectric medium in contact with the sensor surface. When molecules in the sample binding to the sensor surface, the concentration, and therefore the refractive index, at the surface changes and the shift of the SPR dip suited to provide information is detected.

In the past few years, the collaboration of optical fiber technology and SPR has been a subject of intensive research. Importantly, the sensitivity enhancement has been a critical research issue in the area of fiber optic SPR based sensor. Several theoretical as well as experimental studies have been carried out. Tapered fiber offer an advantage of the ease of integration with conventional single mode fiber (SMF) as well as the access to the evanescent field provided by tapering since the light is guided by the boundary between the taper and the external environment. Also its because fast, highly sensitive and low cost tapered optical fiber biosensor that enables the label free detection of biomolecules[2]. This is owing to their unique optical guidance properties that include a relatively low loss, strong evanescent fields, tight optical confinement, and controllable waveguide dispersion. They possess large refractive index contrast which is able to provide tight field confinement that makes tapered fibers particularly suitable for nonlinear optical applications[3].

In the present instrument the dip is detected by the use of a convergent light from Reflectometry System (Nanocalc

2000 Ocean optics). What the SPR instrument actually measures is reflected light intensity that corresponds to the energy gets adsorbed by the plasmons.

2. Experimental Details

Tapered fiber fabrications have been demonstrated by using a wide range of techniques, in this paper we use the flame heating technique which has proven to be one of the most versatile, which can fabricate tapered fiber with good physical properties. The fabrication employs an oxy-butane torch. Fiber optic heated while being pulled slowly. Since borosilicate glass melts at a high temperature we are using oxy-butane torch at 800℃.

Figure 1. *Tapered fiber.*

Figure 1 shows a picture of tapered fiber produced by this method taken with Dino capture 2.0 microscope. Next we try to give metal layer of thickness 50 nm to the tapered fiber. We try using sputtering methods. Sputtering is a process where particles are ejected from a solid target material because of bombardment of the target by high-energy particles.

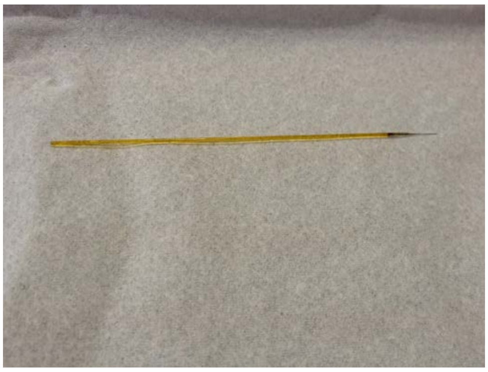

Figure 2. *Tapered fiber with 50 nm gold layer.*

Figure 2 shows tapered fiber made by flame brushing technique and metal layer deposited using sputtering technique.

The Reflectometry System (Nanocalc 2000 Ocean optics) was used to excite light into one end of the tapered fiber sensor and monitor the reflection spectrum from the same end of the tapered fiber. For a typical test, air was used to evaluate the performance of the tapered fiber. The intensity of light reflected internally from the metal film was measured. Experimental SPR set-up can be seen in Figure 3. The reflection spectrum of air was recorded for comparison.

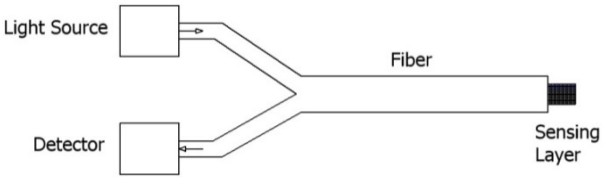

Figure 3. *Experimental SPR set-up.*

The comparison between the initial reflection spectrum on air (red), reflection spectrum dipped in ethanol (blue), and reflection spectrum dipped in sugar solution (black) was shown in figure 4. There was an obvious shift. A change in refractive index at the surface of the gold layer causes the shift. At 589 nm standard refractive index measurements taken, refractive index of water is 1.00, refractive index of 10% glucose solution in water is 1.33, and refractive index of ethanol is 1.36. It was found experimentally that the bigger the refractive index could shift reflection spectrum to the right and it matches our experiment result.

However, the experimental result showed small changes in profile and intensity. There might be some reasons for this. First, the tested tapered fiber sensor was not as ideal as we hoped for. Second, there might be physically adsorbed solution which also changed the properties of the tapered waveguide.

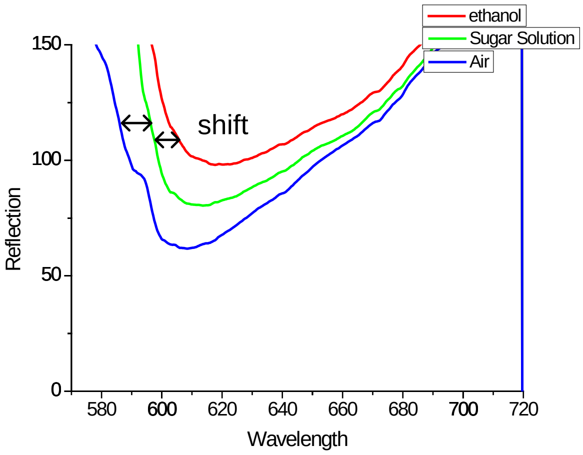

Figure 4. *A shift in SPR dip caused by changes in refractive index.*

3. Conclusion

The excitation of surface plasmon waves in the gold metal-air interface was examined, and a dip in reflected intensity was observed. The performance of SPR refractive index sensor was investigated by using air, ethanol, and sugar solutions. It is noted that the SPR reflectance curve shifts. It is inferred that if the SPR dip in the reflectance is used as a basis for the detection of variation in solution, a reasonably high sensitivity is achieved over a wide range of refractive index measurement.

Acknowledgement

The authors are grateful to Dr. Herman and Dr. Hendro for fruitful discussions. The authors are thankful to Program Riset Kelompok Keahlian ITB 2013 for financial assistance with contract no. 122.57/AL-J/DIPA/PN/SPK/2013.

References

[1] Probing the structure and activity of proteins by surface plasmon resonance (SPR), Lecture Notes, Biozentrum, University of Basel, Klingelbergstrasse 50-70, 4056 Basel, Switzerland

[2] Y. Tian, W. Wang, N. Wu, X. Zou, and X. Wang, “Tapered optical fiber sensor for label-free detection of biomolecules,” Sensors (Basel) 11(12), 3780–3790 (2011)

[3] S. W. Harun, K. S. Lim, C. K. Tio, K. Dimyati, and H. Ahmad, “Theoretical analysis and fabrication of tapered fiber,” Optik, vol. 124, no. 6, pp. 538–543, 2013.I. Akkurt, A. Elkhayat, The effect of barite proportion on neutron and gamma-ray shielding, Annals of Nuclear Energy 51 (2013) 5-9. DOI:10.1016/j.anucene.2012.08.026

[4] Fang, Z., Chin, K. K., Qu, R. and Cai, H., [Fundamentals of Optical Fiber Sensors], Wiley, New Jersey, 395-426, (2012).I. Akkurt, Nuclear Physics, 2nd ed., Prentice-Hall, Englewood Cliffs, NJ, 2014

[5] El-Sherif mahmoud, Bangsal Lalitkumar, Yuan Jianming, “Fiber Optic Sensors for Detection of Toxin and Biological Threats” Sensors 12/2007; 7(12). DOI:10.3390/s7123100

[6] Navina Mehan, Vinay Gupta, K Sreenivas & Abhai Mansingh, “Surface plasmon resonance based refractive index sensor for liquids” Indian Journal of Pure & Applied Physics Vol. 43, November 2005, pp. 854-858

[7] A.A. Jasim, K.S. Lim, M.Z. Muhammad, H. Arof, H. Ahmad, S.W. Harun “Transmission characteristic of multi-turn microfiber coil resonator” Optics & Laser Technology 44 (2012) 1791–1795

[8] Karlsson, Olof (GE Healthcare Bio-Sciences AB, Bjorkgatan 30, Uppsala, S-751 84, SE); BERLING, Henrik (GE Healthcare Bio-Sciences AB, Bjorkgatan 30, Uppsala, S-751 84, SE) 2016 Method to Determine Solvent Correction Curves GE Healthcare Bio-Sciences AB (Bjorkgatan 30, Uppsala, S-751 84, SE) WO/2016/066591

[9] Fabio Vega ; Cesar Torres ; Leonardo Diaz and L. Mattos " Simple method of fabrication tapered fiber ", Proc. SPIE 8785, 8th Iberoamerican Optics Meeting and 11th Latin American Meeting on Optics, Lasers, and Applications, 87852D (November 18, 2013); doi:10.1117/12.2025275

[10] Hsing-Ying Lin, Chen-Han Huang, Gia-Ling Cheng, Nan-Kuang Chen, and Hsiang-Chen Chui, "Tapered optical fiber sensor based on localized surface plasmon resonance," Opt. Express 20, 21693-21701 (2012)

[11] Rajneesh K. Verma, Anuj K. Sharma, B.D. Gupta “Surface Plasmon Resonance Based Taper Fiber optic Sensor with Different Taper Profiles” Optics Communications Volume 281, Issue 6, 15 March 2008, Pages 1486–1491

[12] F. Gao, H. Liu, C. Sheng, C. Zhu and S. N. Zhu “A refractive index sensor based on the leaky radiation of a microfiber” Optics Express 05/2014; 22(10). DOI: 10.1364/OE.22.012645

International Journal of Computational and Experimental Science and Engineering (IJCESEN)
Vol. 2-No.1 (2016) pp. 4-8
http://dergipark.ulakbim.gov.tr/ijcesen

***ISSN:* 2149-9144**

Copyright © IJCESEN

Research Article

A comparative analysis of force-density based form-finding software to minimal surface equation[#]

Jana LIPKOVSKI[1]✉, Florian WEINMANN[2]

[1] PhD candidate, University of Belgrade, Faculty of Architecture, Serbia
[2] Florian Weinmann Modelle, Stuttgart, Germany

* Corresponding Author : j.lipkovski@gmx.de

[#] Presented in ”2nd International Conference on Computational and Experimental Science and Engineering (ICCESEN-2015)”

Keywords
Tensile structures
Formfinding
Numerical Methods
Force-density
Minimal surface

Abstract: The shape of membrane and cable-net structures is usually modeled by geometry of minimal surfaces and its approximations. After experimenting with physical models during 1960s, computational methods were developed to find the initial geometry of tensile structures. Among the early numerical methods applied on form-finding of tensile structures was the finite difference method. An algorithm based on central finite differences combined with a nonlinear iterative process for finding the minimal surface over given stiff boundary conditions is developed and implemented in Mathematica®. The explicit 2-variable formulation as a second order quasi-linear partial differential equation with boundary condition, arising from the Euler-Lagrange area-minimizing condition, has been used for obtaining the soap film geometry. The force-density method, developed in 1970s by Linkwitz and Schek for the roof of the Olympia Stadium in Munich, found its implementation in commercial software EASY®, made by Technet GmbH, Germany. The commercial software used generates a surface which corresponds to the solution of the Laplace's equation. The form finding results obtained by these two methods are compared on some typical examples: the asymmetric hyperboloid membrane, the Concus' sine arc example and a saddle-like structure example.

1. Introduction

Membrane structures and cable nets are a very attractive choice for long-span roof structures especially in climates with low snow loads. Because of their optimum stress distribution, tensile structures use less building materials then conventional structures.

Tensile structures need to be “form-find” - their form is not an arbitrary one. During the second half of the 20th century, as engineers and architects experimented with the new type of structures, physical modeling was of great importance. The experiments were documented very detailed in [3] shown in Fig. 1 left. The shape of tensile structures corresponds to the geometry of minimal surfaces, which is a double curved surface that occupies the smallest area under certain boundary conditions - a particular form of boundary curves.

Figure 1. *Soap film experiments (left) in [3], ILEK Stuttgart (right)*

As a result of these experimental research a few experimental buildings were built, like the building of the Institute in Vaihingen – Stuttgart, Germany – a cable-net structure shown in Fig. 1 right. The experimental form finding methods reached their limits very fast – a change of scale to match the “real” structure was almost impossible without the loss of reliability of the results. In building practice, minimal surfaces have been used because of their characteristics of a soap-film: constant stress field in all directions over the surface (isotropic stress). A soap film is from the mathematical point of view a minimal surface that can be described in variational, differential-geometric and complex analytic mathematical settings. The classical textbook on this matter is [1].

The double-curved geometry is the precondition of the membrane construction characteristics Due to its lack of stiffness, it cannot provide resistance to other loads than tension. Thanks to the special geometry of membrane structures, the membrane resists loads from every direction by increasing its pre-tension when loaded.

Wüchner and Bletzinger in [9] discuss the use of minimal surfaces as the optimal geometry in form-finding of tensile structures. They point out, that for architects, the minimal surface is favorable, because of the clear mathematical principles that these surfaces obey to. From engineering point of view, the material characteristics have to be taken in account. The membrane material is anisotropic and non-elastic, so the soap-film model has been doubted.

For these reasons, multidisciplinary research groups formulated methods that would offer a faster way to form-find tensile structures that could be used for structural analysis and implemented in commercial software. Veenendaal and Block in [4] and Lewis [10] gave an overview of the methods commonly used for form-finding of membranes and cable-nets. Most of them found their application in commercial form-finding software, e.g. the force-density method was implemented in EASY Software package that was used for obtaining the results in this work. Due to differences in their mathematical background and solution methods, the results vary. In [5], a visual comparison of the results of different form finding methods for the IL building in Stuttgart (Fig. 3) has been given. The differences are very noticeable.

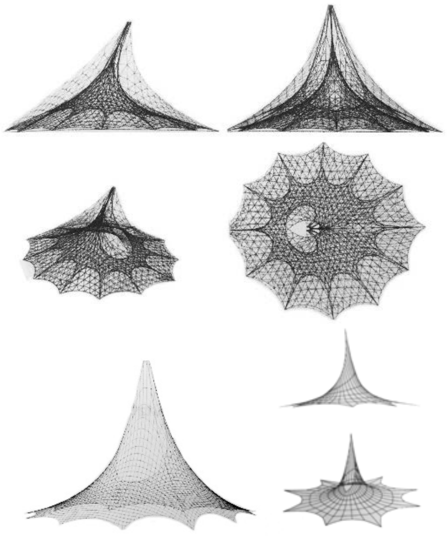

Figure 2. *Different geometries generated with several form-finding methods during the form-finding process of ILEK, Stuttgart ([5])*

2. Force-density based solution

The first solution was obtained by EASY®, software based on the Force Density Method. The method has been developed by Linkwitz and Schek in 1971 in the University of Stuttgart. A detailed description of the software package can be found in [8]. Here we give a brief explanation of the method.

The initial point for all form finding methods is the net structure of nodes and branches whose topology is described by matrix ***C**, branch-node matrix*. Nodes can be of two types: fixed (boundary) and free (interior). Nodes' coordinates form a coordinate vector $\boldsymbol{x}$, and the product $\boldsymbol{u} = \boldsymbol{Cx}$ represents the branches' coordinate vector, obtained as differences of coordinates of the branch ends for every rod. Branch lengths are calculated as $l = (\boldsymbol{u}^T\boldsymbol{u})^{1/2}$. Total matrices of the cable network which contain coordinates of nodes, branches and their lengths will be denoted by ***X, U*** and ***L,*** respectively. The network is in the state of equilibrium, if in each node inner forces are balanced with external loads $\boldsymbol{p}$. For a chosen node i in the network, let j, k, l, m be its neighbouring nodes, a, b, c, d branches determined by pairs of nodes i-j, i-k, i-l, i-m respectively. The equilibrium is expressed by:

$$\overrightarrow{f_a} + \overrightarrow{f_b} + \overrightarrow{f_c} + \overrightarrow{f_d} = \vec{p} \quad (1)$$

If we notice that

$$\overrightarrow{f_a} = f_a \cdot \frac{\overrightarrow{u_a}}{l_a} \quad (2)$$

Where

$$\overrightarrow{u_a} = \frac{\boldsymbol{u_a}}{l_a} \quad (3)$$

$$\overrightarrow{u_a} = (x_j - x_i)\vec{\imath} + (y_j - y_i)\vec{\jmath} + (z_j - z_i)\vec{k} \quad (4)$$

and $\overrightarrow{u_a}/l_a$ is the unit vector of the branch a, we can write the equation of the equilibrium in the form

$$q_a\overrightarrow{u_a} + q_b\overrightarrow{u_b} + q_c\overrightarrow{u_c} + q_d\overrightarrow{u_d} = \vec{p} \quad (5)$$

where the new quantities $q_a = f_a/l_a$, $q_b = f_b/l_b$, $q_c = f_c/l_c$, $q_d = f_d/l_d$ form a vector $\boldsymbol{q}$. This quantity represents the force on the unit length of the branch, known as the force density (Schek [6]). The equilibrium of the whole cable network can be written in the following form:

$$\boldsymbol{P}_i - \boldsymbol{C}_i{}^T\boldsymbol{g}(u) = 0 \quad (6)$$

$\boldsymbol{P}_i$ contains the vectors of external forces in all interior nodes, and $\boldsymbol{C}_i{}^T$ represents the vector of internal equivalent nodal forces for the whole network. Applying Taylor expansion to the second term, the system becomes linear, with unknown coordinates of the interior nodes

$$\boldsymbol{K}_T\Delta x = \boldsymbol{r} \quad (7)$$

where $\boldsymbol{K}_T$ is the tangential stiffness matrix of the cable network, and ***r(u) = r(x)*** is non-balanced load in the network nodes in arbitrary iteration step.

$$\boldsymbol{K}_T = \boldsymbol{C}_i^T \left(\frac{\partial \boldsymbol{g}(\boldsymbol{u})}{\partial \boldsymbol{u}}\right)_{\boldsymbol{u}^i=\boldsymbol{u}_0} \qquad (8)$$

Vector $\boldsymbol{u} = \boldsymbol{u}_0$ contains branch coordinates of the preceding equilibrium state of the network. System in Eq. 8 leads to an iterative process:

$$\boldsymbol{K}_T^{(i)} \Delta \boldsymbol{x}^{(i+1)} = \boldsymbol{r}^{(i)} \qquad (9)$$

The iteration is continued until the residual load is zero $\boldsymbol{r}^{(i)} = 0$ up to a given precision, which leads to equilibrium state in all nodes of the cable network. To solve the system a standard or modified Newton-Raphson iterative method has being used.

3. Non-linear iterative solution of the minimal surface equation

In this analysis, the explicit 2-variable formulation as a second order quasi-linear partial differential equation with boundary condition, arising from the Euler-Lagrange area-minimizing condition, has been used. For a given domain $U \subset \mathbb{R}^2$ with a compact boundary $B = \partial U$ we are looking for a function $z = f(x,y): U \to \mathbb{R}$ which satisfies the equation

$$(1 + f_x^2) f_{yy} + \left(1 + f_y^2\right) f_{xx} - 2 f_x f_y f_{xy} = 0 \qquad (10)$$

As a model example, we take a rectangular domain $U = (a,b) \times (c,d)$ bounded by a rectangle $B = \{a\} \times (c,d) \cup \{b\} \times (c,d) \cup (a,b) \times \{c\} \cup (a,b) \times \{d\}$. An equidistant rectangular mesh with $n+1$ points along x-axis and $m+1$ points along y-axis, with steps h and k respectively, division points $x_i = a + ih, y_j = c + jk$ and mesh knots $P_{ij} = P_{ij}\left(x_i, y_j\right)$ $(i = 0, \dots, n,\ \ j = 0, \dots, m)$ has been layered over the domain. For approximation purposes of partial derivatives in the inner points central finite differences have been used:

$$\begin{aligned}
f_x\left(P_{ij}\right) &\approx \frac{1}{2h}\left(f_{i+1,j} - f_{i-1,j}\right) \\
f_y\left(P_{ij}\right) &\approx \frac{1}{2k}\left(f_{i,j+1} - f_{i,j-1}\right) \\
f_{xx}\left(P_{ij}\right) &\approx \frac{1}{h^2}\left(f_{i+1,j} - 2f_{i,j} + f_{i-1,j}\right) \\
f_{yy}\left(P_{ij}\right) &\approx \frac{1}{k^2}\left(f_{i,j+1} - 2f_{i,j} + f_{i,j-1}\right) \\
f_{xy}\left(P_{ij}\right) &\approx \tfrac{1}{4hk}\begin{pmatrix} f_{i+1,j+1} - f_{i-1,j+1} - \\ f_{i+1,j-1} + f_{i-1,j-1} \end{pmatrix} \qquad (11)
\end{aligned}$$

The subscripts represent the values of the function f in mesh points $f_{i,j} = f\left(P_{ij}\right) = f\left(x_i, y_j\right)$. The approximation error has second order with respect to h, k. This gives rise to a system of (not linear, but cubic) equations with $(n-1) \times (m-1)$ indeterminate values of f in the interior mesh points. Due to original approximation, this nonlinear system transforms into an iteration process

$$\begin{aligned}
f_{i,j} = {} & \frac{1}{2\left(4h^2 + \left(f_{i+1,j} - f_{i-1,j}\right)^2\right) + 2\left(4k^2 + \left(f_{i,j+1} - f_{i,j-1}\right)^2\right)} \\
& \times \Big[\left(4h^2 + \left(f_{i+1,j} - f_{i-1,j}\right)^2\right)\left(f_{i,j+1} + f_{i,j-1}\right) + \\
& \left(4k^2 + \left(f_{i,j+1} - f_{i,j-1}\right)^2\right)\left(f_{i+1,j} + f_{i-1,j}\right) - \\
& - \tfrac{1}{2}\left(f_{i+1,j} - f_{i-1,j}\right)\left(f_{i,j+1} - f_{i,j-1}\right)\left(f_{i+1,j+1} - f_{i-1,j+1} - \right. \\
& \left. f_{i+1,j-1} + f_{i-1,j-1}\right)\Big] \qquad (12)
\end{aligned}$$

To find the value in one mesh point, 8 neighboring mesh points are being used (horizontal, vertical and diagonal points). Although this is in the spirit of the method used in [2], this method is a non-linear, non-Newton iteration method.

As the initial value $f^{(0)}$ for f in the iterative process the solution of the Laplace's equation with the same boundary condition has been used. Using the central difference formulas, this equation converts to a simple linear system in the standard iterative form:

$$\begin{aligned}
& f_{xx} + f_{yy} = 0 \to \\
& f_{ij} = \tfrac{1}{4}\left(f_{i+1,j} + f_{i-1,j} + f_{i,j+1} + f_{i,j-1}\right) \qquad (13)
\end{aligned}$$

The boundary conditions (BC) used in calculated examples are linear. The value $f(x,y)$ is interpreted as the height of the spatial point over $(x,y) \in B$.

4. Results

The first example is an asymmetric surface over $U = (-1,1) \times (-1,1)$. High points of the membrane modelled have different heights: $z = 8$ and $z = 16$, divided into rectangular mesh with $n = m = 21$. The process described in 3 was programmed in Mathematica® and it converges to a solution of the minimal surface equation. The initial approximation $f^{(0)}$ is a hyperbolic-paraboloid -the solution of the Laplace's equation obtained in 761 iterations with precision of $\varepsilon = 10^{-5}$.

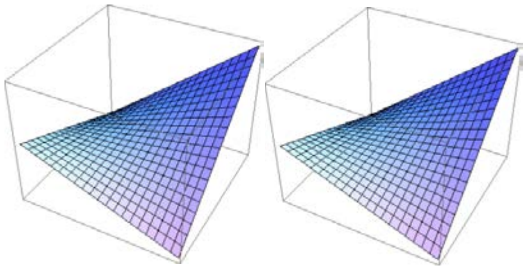

Figure 3. *The initial approximation $f^{(0)}$ (left) and the minimal surface f (right)*

After obtaining the initial shape approximation $f^{(0)}$, the minimal surface f generated is shown in Fig. 5, obtained in 427 iterations with iteration precision of $\varepsilon = 10^{-5}$. The maximum of the difference between $f^{(0)}$ and $f$over the given domain is $\max_U \left|f - f^{(0)}\right| = 0.2390$ (Fig. 6 left). Using the commercial software EASY®, in the same example (same boundary conditions without external loads), the surface g is obtained. This surface is practically the same as $f^{(0)}$ (see Fig. 5 left) obtained by solution of the Laplace's equation. The difference of the two over the given domain is $\max_U |g - f^{(0)}| = 0.00789$.

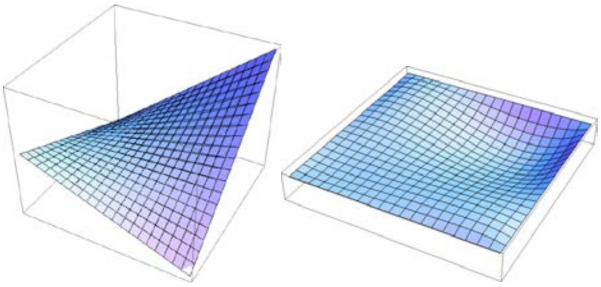

Figure 4. *The minimal surface f and surface g obtained by FD-method (left) and their difference $f - g$ (right)*

Fig. 6 left shows both the minimal surface $f$and the surface g found by EASY® - based on Force-density on the same graph. As it is seen, there are differences between these solutions, which can be noted especially in the region of the higher curvature - close to the higher corner. Fig. 6 right shows the difference between the minimal surface f found by the method described in 3 and the surface g. The maximum difference of the two solutions over the given domain is $\max_U |f - g| = 0.23942$. This is approximately 1.50% of the height.

The second example is a model example from [2] - all boundary lines are equal zero, except one - a sinusoidal arc. The approximation $f^{(0)}$ is obtained in 670 iterations with iteration precision of $\varepsilon = 10^{-5}$, and the minimal surface f in 620 iterations with the same precision. The maximum of the difference between $f^{(0)}$ and $f$over the given domain is $\max_U |f - f^{(0)}| = 0.1990$, which is shown in Fig. 7, the difference between them multiplied by factor 10.0.

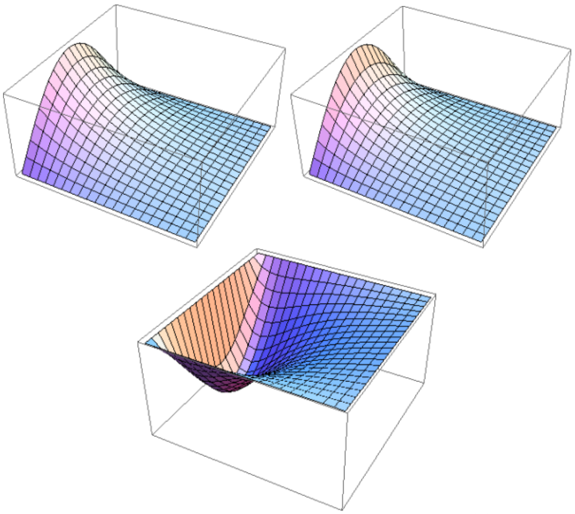

Figure 5. *Example from [2] (left to right): $f^{(0)}$, f, and $f - f^{(0)}$.*

In the third example we examined a saddle-like structure. The initial approximation $f^{(0)}$ (the solution of the Laplace's equation) is obtained in 726 iterations with iteration precision of $\varepsilon = 10^{-5}$, and the minimal surface f in 761 iterations with the same precision. The maximum of the difference between $f^{(0)}$ and f over the given domain is $\max_U |f - f^{(0)}| = 0.2011$. (shown in Fig. 8).

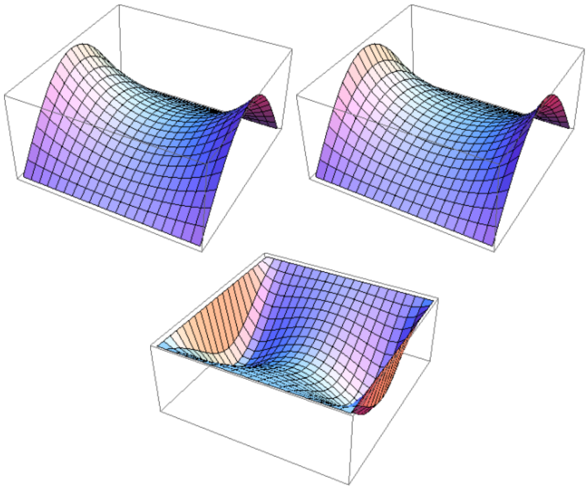

Figure 5. *A saddle-like structure with sinusoidal boundaries (left to right): $f^{(0)}$, f and $f - f^{(0)}$.*

5. Conclusion

The standard model of the soap film surface developed in architecture by Frei Otto led to a widely spread belief that the best architectural model for a membrane structure is the minimal surface (soap-film). This turned out to be controversial and contemporary engineers and researchers discuss, trying to find the optimal mathematical model for form-finding of membrane structures.

In the present paper, a simple iterative nonlinear process was used to obtain the exact minimal surface over a fixed given quadrilateral domain. The commercial software used for the same purpose as its output usually does not give the minimal surface but the surface which corresponds to the solution of the Laplace's equation. Three analyzed examples are shown: the asymmetric hyperboloid, the Concus' sine arc example and a saddle-like structure example. The difference of the two approaches did not exceed 1.50% of the height in three analyzed examples. Under standard exploiting conditions, this is not a notable difference. Under heavy load circumstances, the difference might be considered notable. It would be of interest to examine the difference of the surfaces obtained under external load.

Acknowledgement

The author expresses her sincere gratitude to Jürgen Holl and Bernd Stary from Technet GmbH for time-limited free use of the software package EASY® for research purposes and she acknowledges the support of the Ministry of Education, Science and Technical Development of the Republic of Serbia under grant OI 174020.

References

[1] Osserman R., A Survey of Minimal Surfaces, Dover Publ NY, 2002 (ISBN 978-0486649986)

[2] Concus P., Numerical Solution of the Minimal Surface Equation. Math Comput 21, (1967), 340-350 (doi: 10.1090/S0025-5718-1967-0229394-6)

[3] Bach K., Burkhardt B., Otto F., IL 18 – Seifenblasen, FormingBubbles. Krämer Stuttgart, 1988 (ISBN 3782820185)

[4] Veenendaal D., Block Ph., "An Overview and Comparison of Structural Form Finding Methods for General Networks". Int J Solids Structures, 49 (2012),3741-3753 (doi:10.1016/j.ijsolstr.2012.08.008)

[5] Höller R., FormFindung: architektonische Grundlagen für den Entwurf von mechanisch vorgespannten Membranen und Seilnetzen. Balistier Mähringen, 1999 (ISBN 978-3980616898)

[6] Ströbel,D. Singer,P. "Computational Modelling of Lightweight Structures – Formfinding, Load Analysis and Cutting Pattern Generation"; www.technet-gmbh.com

[7] Lipkovski J., "Form-finding and Modeling of Membrane Structures based on Minimal Surfaces", Master thesis, University of Belgrade - Faculty of Civil Engineering, 2013

[8] Schek H.-J., "The force density method for form finding and computation of general networks", Computer methods in applied mechanics and engineering, 3: 115-134, 1974 (doi: 10.1016/0045-7825(74)90045-0)

[9] Wüchner R., Bletzinger K.-U., "Stress-adapted numerical form finding of pre-stressed surfaces by the updated reference strategy", International Journal for Numerical Methods in Engineering 64 (143–166), 2005 (doi: 10.1002/nme.1344)

[10] Lewis W., Tension Structures – Form and Behaviour. London, Thomas Telford, 2003 (ISBN 9780727732361)

International Journal of Computational and Experimental Science and Engineering (IJCESEN)
Vol. 2-No.1 (2016) pp. 9-18
http://dergipark.ulakbim.gov.tr/ijcesen

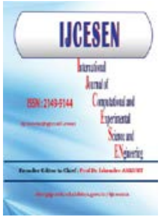

Copyright © IJCESEN

***ISSN:* 2149-9144**

Research Article

Improved K-means Clustering Algorithm for Biological Data using Voronoi Diagram[#]

Damodar REDDY[1]*, Pravin PAWAR[1]

[1]National Institute of Technology Goa, Farmagudi, Goa, India

* Corresponding Author : dr.reddy@nitgoa.ac.in

[#] Presented in "2nd International Conference on Computational and Experimental Science and Engineering (ICCESEN-2015)"

Keywords
Clustering
K-means
Voronoi Diagram
Biological Data

Abstract: As a simple clustering method K-means is known as an algorithm of choice for many clustering challenges due to its performance of clustering large data sets. However, it has two major drawbacks, the random selection of initial cluster centers and the pre estimation of 'K' value in advance. Here, we propose a method that overcomes these problems with the help of Voronoi diagram. To resolve the random selection of initial cluster centers, we use Voronoi diagram. The vertices in the Voronoi diagram are located first and then merged iteratively to converge to 'k' number of points which can be treated as initial cluster centers for K-means. The second problem of inputting 'K' value in advance is enhanced by taking a limit on the radius of Voronoi circle. The experimental results carried out on various synthetic and biological data sets are proved the efficiency of the proposed method..

1. Introduction

Data mining, or knowledge discovery in databases is the technique of analysing data to discover previously unknown information. Clustering [1] is one of the primary data analysis methods refers to a task of partitioning the given set of patterns into homogeneous disjoint groups called clusters and can be defined as regions in which the density of the objects is locally higher than in other regions. Therefore, a cluster is a collection of objects that are similar among themselves and dissimilar to the objects belonging to other clusters. Clustering do not make any statistical assumptions to data. Hence it is an example of unsupervised classification. It helps in finding hidden patterns and describes the underlying knowledge form a large data set. Various algorithms have been developed to solve different type of clustering problems. As a result clustering has variety of applications in various domains such as image processing [2], wireless sensor networks [5], bioinformatics [3] and knowledge discovery [4]. Clustering algorithms are mainly categorized into two types, Hierarchical algorithms and Partition algorithms. In hierarchical clustering [6] the given data set divided into smaller sub sets in hierarchical fashion. Hierarchical clustering does not require us to specify the number of clusters in advance and most hierarchical algorithms that have been used are deterministic. Hierarchical algorithms are divided into two types, agglomerative and divisive. Unlike hierarchical, partitional clustering [7] algorithms attempts to directly decompose the data set into a set of disjoint clusters. Much attention is paid in case of partitional clustering techniques and number of clustering algorithms have been proposed. A commonly used partitional clustering method is K-means [1]. It is one of the most used iterative clustering algorithm used in variety of domains because of its simplicity and effectiveness. The K-means algorithm attempts to find the cluster centres, (c1,…,ck), such that the sum of the squared distances (this sum of squared distances is termed the Distortion, D) of each data point (xi) to its nearest cluster centre (ck) is minimized. Here the distortion is defined as follows.

$$D = \sum_{i=1}^{n}\left[\min_{k=(1...K)} d(x_i, c_k)\right]^2 \qquad (1)$$

However, K-means suffers from two major problems namely, the random selection of initial cluster centers and estimation of output number of clusters in advance. The in appropriate selection of initial cluster centers or the k value affects the clustering results significantly. Various attempts [8], [9], [10] have been made to select the initial cluster centers and to estimate the k value exactly. But they do not fulfil all the requirements in terms of efficiency, fastness and time complexity etc. Therefore, we propose a novel algorithm that finds the good seeds to act as initial clusters and to estimate the k value in advance with the help of Voronoi diagram [11]. It is a well known technique from computational geometry, especially popular for nearest neighbor problems. It has been used for cluster analysis and few algorithms [12], [13] have been developed. The Voronoi diagram is used to form the initial cluster centers with the help of voronoi vertices and circles. A threshold limit on the radius of the Voronoi circle is given to form k points that are treated as initial cluster centers to K-means. The proposed algorithm is tested on various synthetic and real world data sets and the results are compared with the classical K-means and improved K-means algorithms to show the efficiency of the proposed method. The rest of the paper is structured as follows. The useful terminologies are discussed in section 2 and the related work is described in section 3. We formulize the proposed algorithm in step 4. Finally experimental results are shown in section 5 followed by conclusion in section 6.

2. Basic Terminologies

We first discuss some terminologies that can help in understanding our proposed algorithm as follows.

2.1 K-means

K-means [1] algorithm finds the clusters by partitioning the given data set by minimizing the squared error between the empirical mean of a cluster and the points in the cluster. Let Ck denote the kth cluster of the data set: {x1, x2,…, xn}. Then if µj is the mean of the cluster Cj, the squared error between µk and the point xi within Cj is as follows.

$$S(C_j) = \sum_{x_i \in C_j} \| x_i - \mu_j \| \qquad (2)$$

The aim of K-means is to reduce the sum of squared error for all the 'K' clusters. i.e., to minimize S(C).

$$S(C) = \sum_{j=1}^{K} \sum_{x_i \in C_j} \| x_i - \mu_j \| \qquad (3)$$

The algorithm is as follows [14].

Step 1: Select K initial cluster centers $c_1, c_2, \ldots, c_K$ randomly from the given n data points $\{x_1, x_2, \ldots, x_n\}$, $K \leq n$.

Step 2: Assign each point x_i, $i = 1, 2, \ldots, n$ to the cluster C_j corresponding to the cluster center c_j, for $j = 1, 2, \ldots, K$ iff $\|x_i - c_j\| \leq \|x_i - c_p\|$ $p = 1, 2, \ldots, K$ and $j \neq p$.

Step 3: Compute new cluster centers $c_1^*, c_2^*, \ldots, c_K^*$ as follows

$$c_i^* = \frac{1}{n_i} \sum_{x_j \in C_i} x_j \quad \text{for } i = 1, 2, \ldots, K.$$

where n_i is the number of data points belonging to the cluster C_i.

Step 4: If $c_i^* = c_i$, $i = 1, 2, \ldots, K$, then terminate. Otherwise continue from step 2.

2.2 Voronoi Diagram

Given a set of points, Voronoi diagram [11] is a partition of space into cells, each of which consists of the points closer to one particular object than to any others. It is formally defined as follows.

Let $S = \{p_1, p_2, \ldots, p_n\}$ be a set of n points in a d-dimensional Euclidean space and $d(a, b)$ denotes distance between the points a and b in this space. Then the Voronoi diagram of S (see Fig. 1) is defined as the subdivision of the space into n cells, one for each point in S. A point u lies in the cell corresponding to the point p_i iff $d(u, p_i) < d(u, p_j)$ for each $p_j \in S$ and $j \neq i$. We denote the Voronoi diagram of S by Vor(S) and the cell corresponding to the point p_i by $V(p_i)$. We call the vertices of a Voronoi diagram as Voronoi vertices. There are maximum $2n$-5 Voronoi vertices in a Voronoi diagram of *n* points. It is obvious from the definition that for each point *pi* ϵ *S*, V(p_i) contains all the points that are closer to p_i than to other points of *S*. For a Voronoi vertex *v*, we define the largest empty circle of *v* (see Fig. 2) with respect to *S*, as the largest circle with *v* as its centre that contains no point of *S* in its interior. We denote this circle by CirS(*v*). The Voronoi vertices have the property that a point *q* is a vertex of Vor(*S*) iff CirS(*q*) contains three or more points of *S* on its boundary. A point *p* is said to be covered by a vertex *q* if and only if *p* lies on the boundary of CirS(*q*).

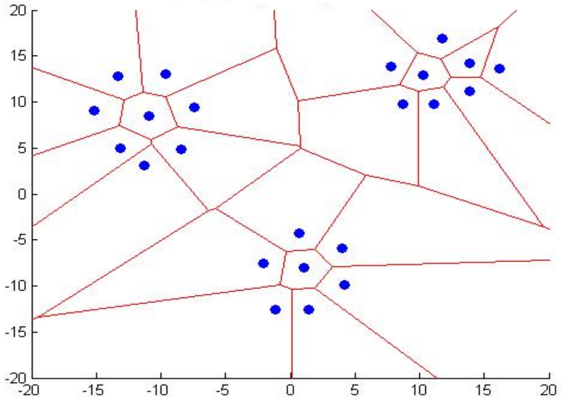

Figure 1. *Voronoi diagram of given points.*

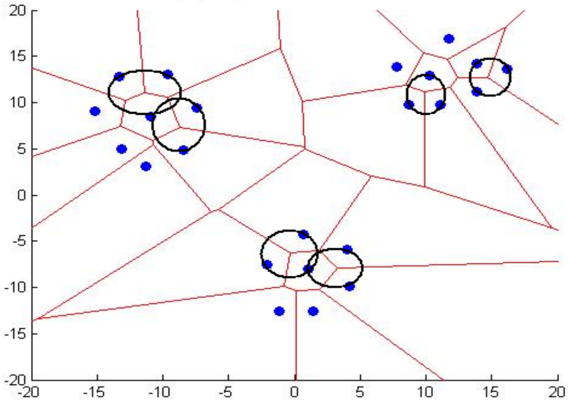

Figure 2. *Voronoi diagram with Voronoi circles (all circles are not shown)*

In our proposed algorithm we use the Vornoi vertices to represent all the given points and then these vertices are further merged to form 'k' number of points where each point represents a cluster center. The merging of the closer vertices is done by reconstructing the Voronoi diagram with these vertices. we input a limit on the radius of the Voronoi circle to terminate the process and the resultant points are the required initial cluster centers for K-means.

2.3 Dynamic Validity Index

Validity index is used to measure the quality of the clusters formed, especially in case of multi-dimensional data. Many validity indices have been proposed so far. In our algorithm, we use dynamic validity index (DVI) [15] defined as follows. Let N be the number of data point, K be the pre-defined upper bound number of clusters, and zi be the center of the cluster Ci. The dynamic validity index is given by

$$DVI = \min_{k=1,2,,,,,K} \{IntraRatio(k) + \gamma * InterRatio(k)\}$$

where

$$IntraRatio(k) = \frac{Intra(k)}{MaxIntra}, InterRatio(k) = \frac{Inter(k)}{MaxInter}$$

$$Intra(k) = \frac{1}{N} \sum_{i=1}^{k} \sum_{x-C_i} \left\| x - z_i \right\|^2, MaxIntra = \max_{i=1,2,\ldots,k} (Intra(i))$$

$$Inter(k) = \frac{Max_{i,j}\left(\left\| z_i - z_j \right\|^2\right)}{Min_{i \neq j}\left(\left\| z_i - z_j \right\|^2\right)} \sum_{i=1}^{k} \left(\frac{1}{\sum_{j=1}^{k} \left\| z_i - z_j \right\|^2} \right)$$

and $MaxInter = \underset{i=1,2,\ldots,k.}{Max} (Inter(i))$

Here, *Intra Ratio* stands for the overall compactness of clusters scaled from *Intra* term, where as *Inter Ratio* represents overall separation of clusters scaled from *Inter* term. The *Intra* term is the average distance of all the points within a cluster from cluster center. Then we have *Inter* term which is composed of two parts, both of them based on cluster centers. The value of *Inter* increases with the increment in *k*.

3. Related Work

3.1 K-means clustering algorithm

K-means algorithm developed by MacQueen [16] is one of the most popular nonhierarchical and squared error clustering technique that belongs to partitioning methods of clustering. It is a very robust technique and its convergence has always been proved. As we have discussed in Section 1 that it sometimes suffers from the global optima due to arbitrary selection of initial cluster centers. It also suffers from the estimation of correct number of clusters in advance. Many researches proposed various methods to overcome these problems, a good review of which can be seen from [9]. A recursive method for the initialization of cluster centre is proposed by Duda and Hart [17]. The algorithm proposed by Fisher [18] generates good seeds by constructing initial hierarchical clustering groups. Both Higgs et al., [19] and Snarey et al. [20] developed a method using MaxMin algorithm to choose a subset of the original database as initial cluster centers. Bradley et al., [21] formed the initial clusters based on the bilinear program, provided that the sum of the distances of each point to its nearest center is minimized. Khan and Ahmed [22] proposed an algorithm for resolving the problem of random selection. Considering all these issues, still there is no universal clustering technique that can initialize the cluster centers for K-means, due to the dissimilar characteristics of various problem domains. MacQueen, [16] introduced an online learning strategy that determines a set of cluster seeds based on the calculation of mean vector. But this method is costly in case of large data sets because of the repetitive calculation of mean vector every time a new point added. Tou and Gonzales [23] recommended another method based on the distance between the successive seeds and a threshold value. But this method entirely depends on the order of the points in the database and a user defined threshold value. Linde et al., [24] proposed a method based on Binary Splitting (BS) which splits the cluster centre using a small random vector. This method is computationally expensive as K-means is to be implemented after each split. Also the cluster quality mainly depends on the selection of random vector which determines the direction of the split. Kaufman and Rousseeuw [25] developed a method which is based on the reduction in the Distortion. Here the seeds that increase the reduction in the distortion are chosen for the next step. Babu and Murty [26] proposed a technique for the near optimal seed selection based on genetic programming. Although this method can find the optimal solution, yet it faces the problem of repetitive run of K-means until given number of clusters formed. This is also not robust in case of very large data bases. Huang and Harris [27] projected a method called Direct Search Binary Splitting (DSBS) which is same as the BS algorithm with a small change. Here the splitting is done efficiently through the Principle Component Analysis (PCA) which is based on the vector of Linde et al., [24] for the splitting. Thiesson et al., [28] introduced a method that depends on the mean value of the whole given data set which creates a set of K-points around the mean of the data. Bradley and Fayyad [29] proposed an initialization approach for K-means in which the given data points are randomly divided into few data sets and then K-means is applied on each set with the initial cluster centers chosen from Forgy's method. They again apply K-means algorithm on the centers of the clusters formed and repeat the step. Finally the centre points left are for the initialization of K-means for the entire dataset.

3.2 Voronoi-based clustering algorithms

The Voronoi diagram [11] is an efficient technique from computational geometry that plays an eminent role for data clustering. It has been especially designed for nearest neighbor problems and applied extensively on cluster analysis. Few clustering algorithms [12], [13] have been developed based on Voronoi diagram. A brief survey of them is as follows. Haowen Yan et al.[30] proposed an algorithm to generate point clusters based on Voronoi diagram by considering four types of information. They are statistical, thematic, topological, and metric information's. Jana et al. [31] proposed another clustering algorithm using Voronoi diagram and the cluster density proposed by Daxin Jiang [32]. In this method the clusters are formed by exploiting the Voronoi diagram as follows. 1) The Voronoi vertices are used as the initial centroids (cluster centres) and the points on its largest empty circles are used to form the initial clusters. 2) Only the neighbouring clusters that share a Voronoi edge are merged to produce the best clusters for the next iteration. Therefore, there is no need of searching the entire set and the overall run time of the proposed algorithm is reduced. Bishnu et al.[12] developed a method with the help of K-means and Voronoi diagram. In the first phase K-means algorithm is used to create a set of small clusters. Then in the next phase the actual clusters are formed with the help of Voronoi diagram. A novel clustering technique for uncertain data has been proposed by Ben kao et al.[33]. They developed few pruning techniques based on Voronoi diagram to reduce the number of expected distance calculation and then formed the clusters. Motivated with all these clustering methods, we propose a method based on K-means and Voronoi diagram.

4. Proposed Algorıthm

The main scheme behind the proposed technique is summarized as follows. Given the set of n data points, say S, the Voronoi diagram Vor(S) is first constructed. First of all, we find the minimum number of Voronoi vertices to cover all the given points. i.e., we represent all the given points by its closer Voronoi vertex. To find such useful Voronoi vertices, the Voronoi circles surrounding all the vertices are traced out. Then these Voronoi circles are sorted in ascending order with respect to the radius of their largest empty circle. We now consider the Voronoi circle with least radius and represent the points on its circumference with its vertex. Since we started with least radius Voronoi circle, this vertex is closer compared to all the other vertices. Then the next least radius circle is taken and the points on its boundary are taken to be represented by its vertex. If any point is already covered by a vertex, we ignore that point and proceed further. Because the Voronoi circles are sorted with respect to their radius in ascending order, hence, the points are covered by its closer vertices. We repeat the same step unless all the given 'n' points are covered by its closer vertices. Now the Voronoi diagram is reconstructed with the help of these Voronoi vertices. and repeat the same process. A limit on the radius of the Voronoi circle is given to terminate the procedure. If there is no Voronoi circle whose radius is less than that limit, then there is no further formation of new vertices to cover the points. We stop the process and store the resultant vertices (assume 'k') in a set. We then run K-means algorithm on the given data set with these 'k' points taken as the initial cluster centers. We now formalize the pseudo code as follows.

Algorithm *VK*-means:
Input: $X[n][d]$, μ
Output: $C_1, C_2, \ldots, C_k$

Functions and Notations used:
S: Given set of *n* points and d dimension
Vor(*S*): It constructs the Voronoi diagram for the data set S and stores the Voronoi vertices
v_i : Voronoi vertex $i = 1, 2, \ldots, 2n-5$ (max.)
CirS(*v*): It finds the largest empty circle of vertex *v*
R(*CirS*(*v*)): It finds the radius of the Voronoi circle *CirS*(*v*).
K-means(S, S´): It runs *K*-means algorithm for the set S of '*n*' points and with the set S´ of '*k*' initial cluster centers.
r: a temporary variable.
μ: Threshold value on the radius of the Voronoi circle to separate the cluster centers.

```
Step 1: Given a set S of 'n' points, construct the Voronoi diagram Vor(S).
Step 2: Sort all the Voronoi vertices $v_i$ in ascending order with respect to the radius of their largest empty Voronoi circle's CirS($v_i$), $i = 1,2, \ldots, 2n-5$ (max.) and store them in an array V[].
Step 3: Repeat steps 4 through 7 for $i = 1, 2, \ldots, 2n - 5$
Step 4: Assign the radius of CirS(V[i]) to 'r', i.e, $r = R(CirS(V[i]))$
Step 5: If $r \leq \mu$ then locate all the points lying on the boundary of CirS(V[i]). If any point is already covered by a circle then ignore that point.
Else go to step 7.
Step 6: Store the vertex V[i] in a set S´.  $i=i+1$
Step 7: If $r > \mu$ then store the uncovered points (if any) in the set S´ and exit the loop.
Step 8: If  $S = S´$ then go to step 9
            Else construct the Voronoi diagram Vor(S') for   the set S' and go to step 2.
Step 9: Call K-means(S, S´) to obtain the set of clusters, say $\{C_1, C_2, \ldots, C_k\}$.
Step 10: Stop
```

Complexity Analysis

Step 1 requires $O(n \log n)$ time for the construction of the Voronoi diagram of the *n* data points. Step 2 also requires $O(n \log n)$ time for sorting. Steps 4 through 6 are repeated at most 2n – 5 time in which each of the steps 4, 5, and 6 requires constant time and thus they require $O(n)$ time in total. Step 7 requires linear time. Therefore steps 2 through 7 require $O(n \log n)$ time in total. However, steps 2 through 8 are repeated a finite number of times, say *k* times in which construction of the Voronoi diagram is the dominating computation. Step 9 requires $O(n\tau)$ to run *K*-means clustering. Therefore the overall time complexity of the proposed algorithm is $O(kn \log n) + O(n\tau)$.

5. Experimental Results

This section establishes the practical efficiency of the proposed algorithm. We tested its performance on a number of data sets. These included both synthetically generated data and data used in real applications taken form UCI machine learning repository. The useful experimental setup to implement the proposed scheme is as follows. We have used Intel Core 2 Duo Processor machine with T9400 chipset, 2.53 GHz CPU and 2 GB RAM running on the platform Microsoft Windows Vista.

We now briefly describe the data sets taken for the experiments.

Synthetic Data

Triple-form data with outliers: There is a circular ring, a rectangle and a triangle. We insert seven outlier points. The size of this data set is 1007.

4–band data: There are four clusters in this data type where all the clusters are in the form of parallel bands. The size taken here is 600.

4-Ldata with outliers: There are four clusters in this data set and they are all of L-shaped. We insert here sixteen outlier points. Each cluster represents two perpendicular lines and size of this data set is 1216.

2-non-convex data: The two clusters of this data set are of non-convex shape with 250 points of size each.

The proposed method is applied on all these data sets and the results are compared with classical *K*-means [16], improved *K*-means [34] and Fuzzy C-means [35]. It can be observed that for the Triple-form data set, the K-means, and Fuzzy C-means are failed to obtain the desired clustering results whereas the improved K-means and our proposed algorithm are able to do so as depicted in Figs. 3(a)-3(d) in which all the points within a cluster are shown by same color. For the rest of the synthetic data sets, the K-means, Fuzzy C-means and the improved K-means all are failed to produce the desired clusters and also unable to detect the outliers. On the other hand the proposed algorithm works well on these data sets as shown in Figs. 4-6. The outliers are shown by small hollow circles in Fig. 3 and Fig. 5. It is important to note that the K-means, Fuzzy C-means and the improved K-means are unable to detect. They treat the outliers as the points of the other clusters as depicted by the same colors as the cluster points. For examples, in Fig. 3(a) all the outliers are the part of the ring cluster. Similarly, in Fig. 3(c), two outliers belong to the ring cluster and the remaining outliers belong to the triangle clusters. Whereas, our proposed algorithm successfully detects the outliers which are treated separately from the cluster points as depicted by the color different from any cluster point.

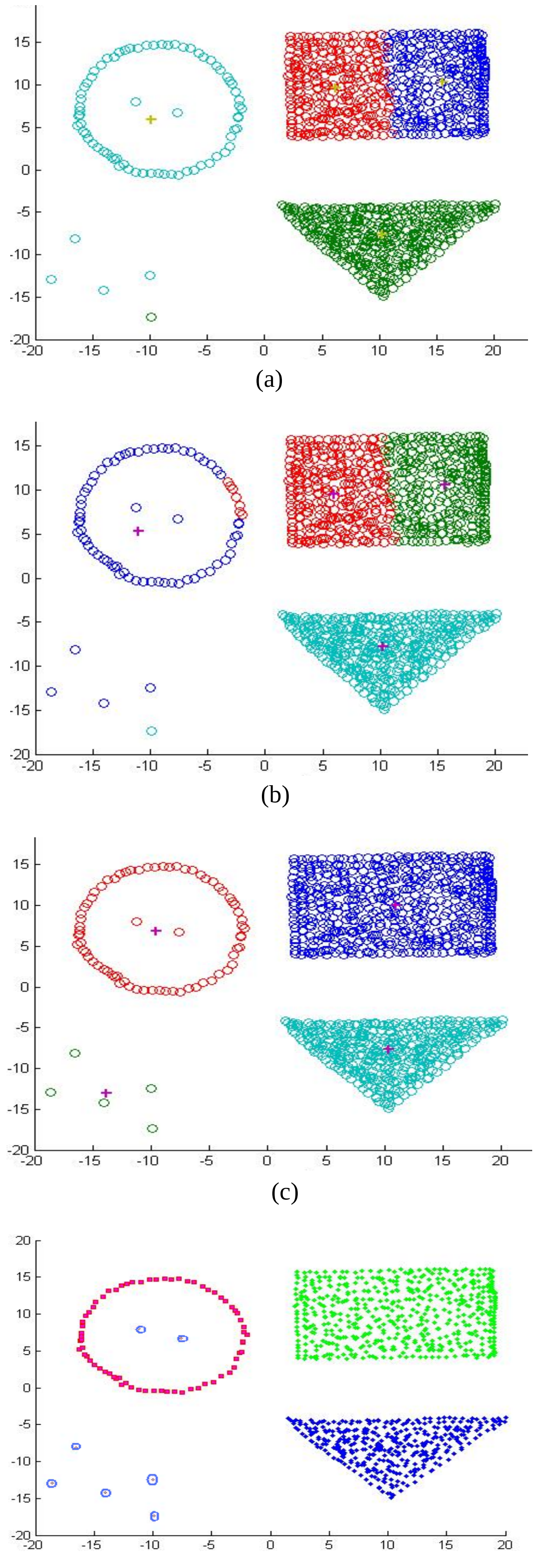

(a)

(b)

(c)

(d)

Figure 3. *Clustering results on Triple-form data of 1007 points: (a) result of K-means clustering; (b) result of Fuzzy C-means clustering; (c) result of Improved K-means clustering; (d) result of proposed algorithm.*

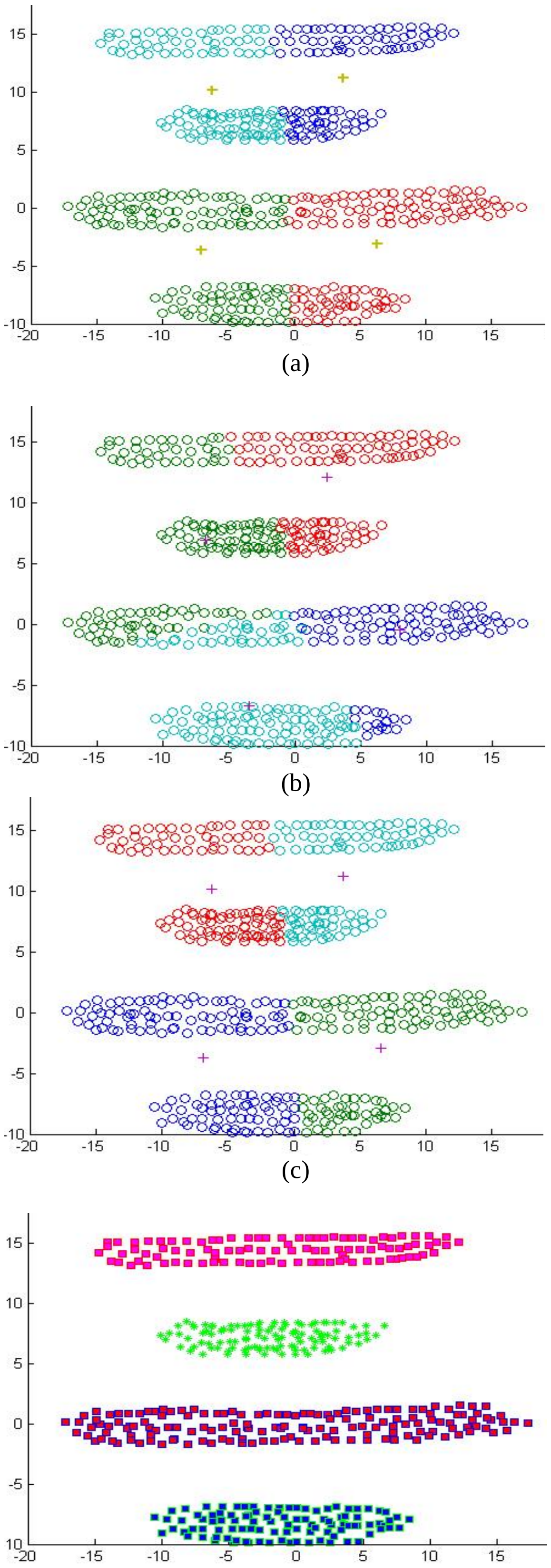

(a)

(b)

(c)

(d)

Figure 4. *Clustering results on 4-band data of 600 points: (a) result of K-means clustering; (b) result of Fuzzy C-means clustering; (c) result of Improved K-means clustering; (d) result of proposed algorithm.*

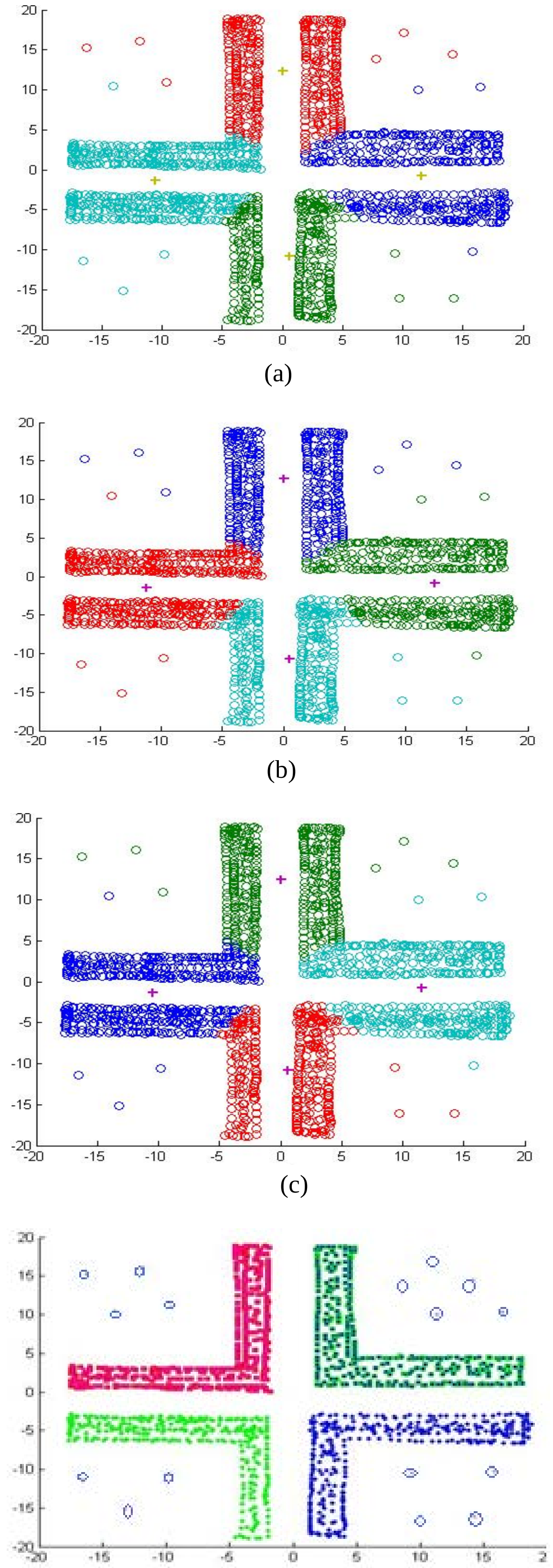

(a)

(b)

(c)

(d)

Figure 5. *Clustering results on 4-L data of 1216 points: (a) result of K-means clustering; (b) result of Fuzzy C-means clustering; (c) result of Improved K-means clustering; (d) result of proposed algorithm.*

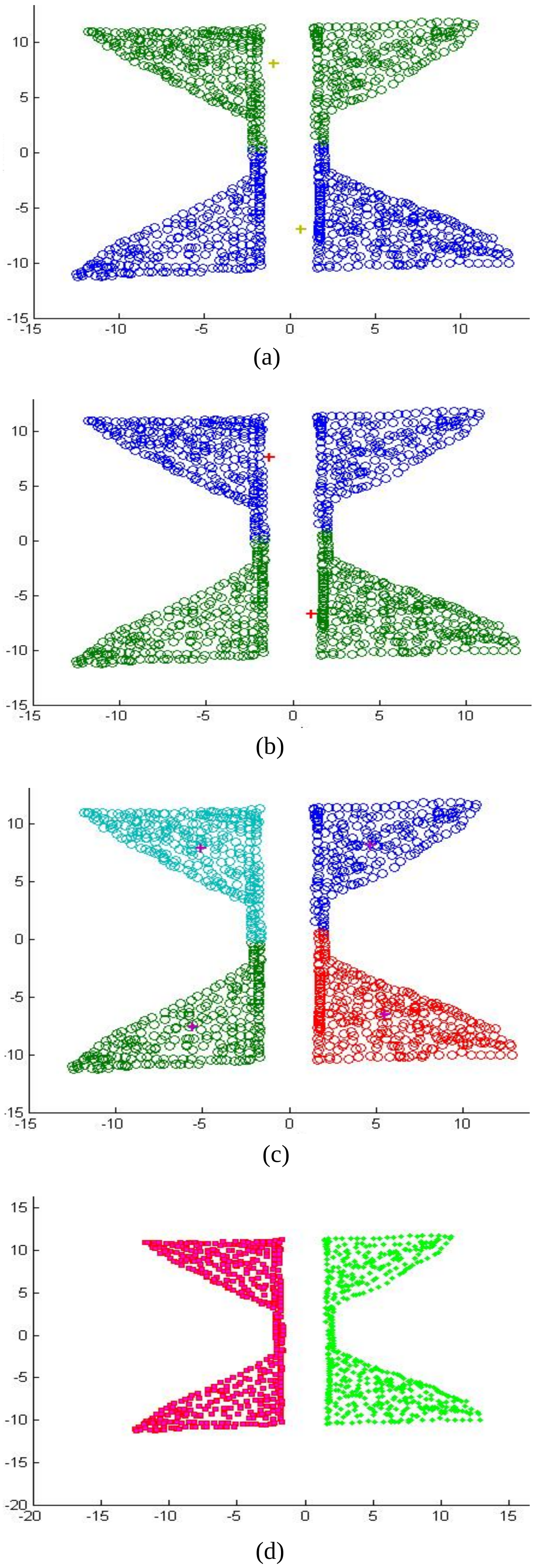

Figure 6. *Clustering results on 2-non-convex data of 500 points: (a) result of K-means clustering; (b) result of Fuzzy C-means clustering; (c) result of Improved K-means clustering; (d) result of proposed algorithm.*

Real World Data

Here we consider few data sets from the UCI machine learning repository [36]. These data sets are multi-dimensional; hence we show the resultant clusters with the help of validity index.

Iris data: This is a famous data set used often in many clustering algorithms. It has three classes namely *Setosa*, *Versicolor* and *Virginica*. The set consists of 150 points with 50 instances for each class. Each point is described by a set of four attributes viz sepal length, sepal width, petal length and petal width. Our objective is to separate the points of different classes.

Spect heart data: This data set describes about cardiac Single Proton Emission Computed Tomography (SPECT) images. Each patient classified into two categories: normal and abnormal. There are 187 instances (SPECT image sets) taken with 22 attributes (binary feature patterns)

Wine data: This data is the result of a chemical analysis of wines to determine the origin of wines. We take the data set of 178 instances with 13 attributes and three classes. The analysis determined the quantities of 13 constituents found in each of the three types of wines. The three classes have 59, 71 and 48 instances respectively. All these classes are separable.

(Statlog) heart data: This dataset is a heart disease database similar to the Spect-Heart data set, but with small difference. Here the two classes represent the absence and presence of cost matrix. The data set taken here is of 270 points with 13 attributes each.

Pima-India-Diabetics (PID) data: This dataset donated by Vincent Sigillito, and is a collection of medical diagnostic reports of 768 examples from a population living near Phoenix, Arizona, USA. They used 576 training instances and obtained a classification of 76% on the remaining 192 instances. Here, the number of classes is two with 576 and 192 instances respectively. The number of attributes is 8.

Soybean (small) dataset: This is a Michalski's famous soybean disease database of 47 instances each of which has 35 attributes and belongs to four classes.

Breast Tissue: This is a dataset with electrical impedance measurements of freshly excised tissue samples from the breast. The number of instances taken here are 106 with 9 attributes per each. Here the numbers of classes is 2.

All these data sets are experimented by the proposed technique and the experimental results are compared with classical *K*-means and improved *K*-

means by means of dynamic validity index [15]. It is obvious to observe that the proposed scheme performs well in all the cases compared to the existing techniques *K*-means, fuzzy-c means and improved *K*-means. The comparison results are shown in table 1 (Appendix-1).

6. Conclusion

In this paper we proposed a novel *K*-means algorithm that solves the major problems faced by classical *K*-means. We solve the problem of random selection initial cluster centers with the help of Voronoi diagram. The initial cluster centers have been traced out iteratively by locating the nearest Voronoi circles of each point. Here we need not input the output number of clusters in advance as the ‘k’ initial cluster centers are automatically located with the help of threshold limit given on the radius of Voronoi circle. The experiments carried out many synthetic and multidimensional biological data sets show the efficient formation of clusters over the existing techniques.

References

[1] A. K. Jain, Algorithms for Clustering Data, New Jersey: Prentice Hall, Englewood Cliffs, 1988.

[2] Z. M. Wang, C.S. Yeng, Q. Song, and K. Sim, “Adaptive Spatial Information-theoretic Clustering for Image Segmentation”, Pattern Recognition, Vol. 42, 2009, pp. 2029-2044

[3] S. C. Madeira, and A. L. Oliveira, “Biclustering Algorithms for Biological Data Analysis: A Survey”, Computational Biology and Bioinformatics, Vol. 1, 2004, pp. 24-45.

[4] A.Y. Al-Omary, and M.S. Jamil, “A New Approach of Clustering based Machine Learning Algorithm”, Knowledge Based Systems, Vol. 19, 2006, pp. 248-258

[5] A. A. Abbasi, and M. Younis, “A Survey on Clustering Algorithms for Wireless Sensor Networks”, Computer Communications, 2007, pp.2826–2841.

[6] J. F. Lu, J. B. Tang, Z. M. Tang, and J. Y. Yang, “Hierarchical Initialization Approach for K-means Clustering”, Pattern Recognition Letters, Vol. 29, 2008, pp. 787-795.

[7] C. Fuyuan, J. Liang, and G. Jiang, “An Initialization Method for the K-means Algorithm using Neighborhood Model”,Computers and Mathematics with Applications, Vol. 58, 2009, pp. 474-483..

[8] S. Ray, and R. H. Turi, “Determination of Number of Clusters in K-means Clustering and Application in Colour Image Segmentation”, in fourth International Conference (ICAPRDT-99), Calcutta, India, 1999, pp. 137-143.

[9] A. K. Jain, “Data Clustering: 50 years beyond K-means*”, Pattern Recognition Letters, Vol. 31, 2010, pp. 651-666.

[10] S. Bandyopadhyay, and U. Maulik, “An Evolutionary Technique based on K-means Algorithm for Optimal Clustering in ℜN”, Information Science Applications, Vol. 146, 2002, pp. 221–237.

[11] Preparata FP, Shamos MI. Computational geometry-an introduction. Berlin Heidelberg, Tokyo: Springer-Verlag; 1985.

[12] Bishnu, P.S. and Bhattacherjee, V. (2009) ‘CTVN: Clustering technique using Voronoi diagram’, Journal of Recent Trends in Engineering, Vol. 2, No. 3, pp. 13-15.

[13] Koivistoinen, H., Ruuska, M. and Elomaa, T. (2006) ‘A Voronoi diagram approach to autonomous clustering’. Paper Presented at the International Conference. Discovery Science. Springer, Berlin. 2006. Spain.

[14] S. Bandyopadhyay, and U. Maulik, “An Evolutionary Technique based on K-means Algorithm for Optimal Clustering in ℜN”, Information Science Applications, Vol. 146, 2002, pp. 221–237.

[15] J. Shen, S.I. Chang, E.S. Lee, Y. Deng, S.J. Brown, Determination of cluster number in clustering microarray data, J. App. Math. and Comp.169 (2005) 1172-1185.

[16] J. B. MacQueen, “Some Methods for Classification and Analysis of Multivariate Observation”, in Berkeley symposium on Mathematical Statistics and Probability, University of California Press. 1967, pp. 281-297.

[17] R. O. Duda, and P. E. Hart, Pattern Classification and Scene Analysis, New York: John Wiley and Sons, 1973.

[18] D. Fisher, “Iterative Optimization and Simplification of Hierarchical Clusterings”, Artificial Intelligence Research, Vol. 4, 1996, pp. 147-179.

[19] R. E. Higgs, K. G. Bemis, I. A. Watson, and J. H. Wikel, “Experimental Designs for Selecting Molecules from Large Chemical Databases”, Chemical Information and Computer Sciences, Vol. 37, 1997, pp. 861-870.

[20] M. Snarey, N. K. Terrett, P. Willet, and D. J. Wilton, “Comparison of Algorithms for Dissimilarity-based Compound Selection”, Molecular Graphics and Modeling, Vol. 15, 1997, pp. 372-385.

[21] P. S. Bradley, O. L. Mangasarian, and W. N. Street, “Clustering via Concave Minimization,

in: M.C. Mozer, M.I. Jordan, and T. Petsche (Eds.).” Advances in Neural Information Processing System, Vol. 9, 1997, pp.368-374.

[22] S. S. Khan, and A. Ahmad, “Cluster Center Initialization Algorithm for K-means Clustering”, Patter Recognition Letters, Vol. 25, 2004, pp. 1293-1302.

[23] J. Tou, and R. Gonzales, Pattern Recognition Principles, MA: Addison Wesley, 1974.

[24] Y. Linde, A. Buzo, and R. M. Gray, “An Algorithm for Vector Quantizer Design”, IEEE Trans. on Commun, Vol. 28, 1980, pp. 84–95.

[25] L. Kaufman, and P. J. Rousseeuw, Finding Groups in Data. An Introduction to Cluster Analysis, Canada: Wiley, 1990.

[26] G. P. Babu, and M. N. Murty, “A Near-optimal Initial Seed Value Selection in K-means Algorithm using a Genetic Algorithm”, Pattern Recognition Letters, Vol. 14, No. 10, 1993, pp. 763–769.

[27] C. Huang, and R. Harris, “A Comparison of Several Codebook Generation Approaches”, IEEE Trans. on Image Process, Vol. 2, No. 1, 1993, pp. 108–112.

[28] B. Thiesson, B. Meck, C. Chickering, and D. Heckerman, “Learning mixtures of Bayesian Networks”, Microsoft Technical Report (TR-97-30), 1997.

[29] P. S. Bradley, and U. M. Fayyad, “Refining Initial Points for K-means Clustering”, in Fifteenth International Conference on Machine Learning, 1998,pp. 91–99.

[30] H. Yan and R. Weibel. An algorithm for point cluster generalization based on the Voronoi diagram. Journal of Computers & Geosciences, 34(8):939-954, 2008.

[31] P.K. Jana M.P. Misra and A. Raj. A Voronoi diagram based clustering algorithm. International Journal of Advanced Computer Engineering, 3(2):79-84, 2010.

[32] D. Jiang J. Pei and A. Zhang. DHC: A Density-based hierarchical clustering method for time series gene expression data. In 3 rd IEEE Symposium on Bioinformatics and Bioengineering (BIBE-2003), Bethesda, USA, pages 1 -8, March 10-12, 2003.

[33] B. Kao S.D. Lee F.K.F. Lee D.W. Cheung and W.S. Ho. Clustering uncertain data using Voronoi diagrams and R-tree index. IEEE Transactions on Knowledge and Data Engineering, 22(9):1219-1233, 2010.

[34] F. Geraci M. Leoncini M. Montengaro M. Pellegrini and M.E. Renda. FPFSB: A scalable algorithm for microarray gene expression data clustering. In International Conference on Digital Human Modeling (ICDHM-07), China, volume 4561, pages 606-615, July 22-27, 2007.

[35] J.C. Bezdek R. Ehrlich and W. Full. FCM: the fuzzy c-means clustering algorithm. Computers & Geosciences, 10(2-3):191-203, 1984.

[36] UCI Machine Learning Repository, http://archive.ics.uci.edu/ ml/ datasets.html.

Appendix 1:

Table 1: Comparison chart of the proposed scheme with *K*-means, Fuzzy *C*-means and improved *K*-means using Intra-Inter ratio validity index.

Name	No of Attributes	Data Size	Cluster No.	Val_index (*K*-means)	Val_index (Fuzzy *C*-means)	Val_index (Improved *K*-means)	Val_index (Proposed algorithm)
Iris	4	150	3	0.2930	0.3223	0.2888	0.0836
S. Heart	22	187	2	2.9122	5.8464	2.3846	0.5101
Wine	13	178	3	0.1895	0.1766	0.1895	0.1153
S. log (heart)	13	270	2	0.2632	0.2991	0.2611	0.0323
P.-India-Dia.	8	768	2	0.1549	0.1828	0.1549	0.0344
Soyabin	35	47	4	0.6324	1.9656	0.7010	0.2843
Breast Tissue	9	106	2	0.0522	0.1111	0.0057	0.0052

International Journal of Computational and Experimental Science and Engineering
(IJCESEN)
Vol. 2-No.1 (2016) pp. 19-24
http://dergipark.ulakbim.gov.tr/ijcesen

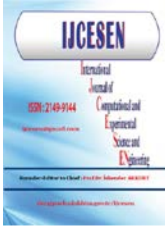

Copyright © IJCESEN

***ISSN:*2149-9144**

Research Article

Microstructure and characterization of titanium alloy (Ti–6Al–4V) and pur titanium prepared by PM[#]

Alaeddine KAOUKA[1]*

[1]Laghouat University, Laboratoire Génie des Procédés, Laghouat –Algeria

* Corresponding Author : a.kaouka@lagh-univ.dz

[#] Presented in ”2nd International Conference on Computational and Experimental Science and Engineering (ICCESEN-2015)”

Keywords
Characterization
titanium alloys
diffusion
DICTRA sofware.

Abstract: The aim of this work is to obtain surfaces with high content of beta enhancing titanium alloy by diffusion process at settled temperatures and times. Two metal alloys are selected, Niobium (Nb) and Molybdenum (Mo). In separate experiments, they are diffused over titanium alloy (Ti–6Al–4V) and over pure titanium (Ti) by using Powder Metallurgy. For this study different experiments were performed, Mo and Nb were diffused in Ti and Ti-64 samples at 1100 and 1200 ºC for 3 and 4 h, respectives. Their microstructure and some mechanical properties such as microhardness were investigated. The experiment succeeds in changing the microstructural properties of the surface of Ti and Ti–6Al–4V samples as characterized by opticla microscopy, SEM and XRD diffraction to confirm the phases obtained, beta and alpha plus beta structures are obtained. In particular, by using diffusion process at 1100 ºC for 3 h. Moreover, the experiment were simulated using DICTRA, these results were compared to the real results of the experiment. DICTRA results were reliable because they were similar to real experiment results.

1. Introduction

Titanium and titanium alloy have involved more attention than other metallic materials with affection due to its capability, performance and protection [1, 2]. In adding its superior corrosion resistance and exceptional raised temperature performance. One of the most important properties of titanium alloy is his lowerstiffness and rigidity compared to other metallic olloys. Titanium and titanium alloy have been used in structural applications for load-bearing sandwich cores in the aerospace and transportation industries and in many other applications.

However, despite these good properties, titanium is used frequently in many applications due to its high raw material and industrial costs [3-4]. Ti-6Al-4V alloy is the most widely used titanium alloy because of their good machinability, high strength, excellent corrosion resistance, and mechanical properties. Thus, Ti-6Al-4V alloy deals the best performance for a variety of weight reduction applications in aerospace, automotive and biomechanical applications. However, holding to their poor wear resistance, their potential applications in relieving engineering tribological components are limited. Hence, the properties of alloy can be developed using the appropriate surface treatment techniques such as ion implantation and low energy high current pulsated electron-beam [5]. The wear resistance of the Ti-6Al-4V alloy can also be improved by producing composite structure using second phase particles.

Powder metallurgy techniques meaningfully donate to the development of effective operating implants. It is found on the limited densification during sintering of metal powders [3]. The process begins by mixing the metal powders with a space holder, followed by the powder mixture uniaxial or isostatic compaction to form a green sample. The sample is subjected to a heat treatment process to eliminate the space holder. Sintering stage at developed temperatures grows sinter neck formation and growth, resulting into densification of the structure and development of structural integrity [1, 5]. This

process based on mechanical alloying of elemental powders tracked by hot association have emerged. In addition, this method is also very effective to prepare a complex alloy in various alloying elements.
However, in this study an attempt has been made to produce fine-grained titanium alloys via a powder technic based on mechanical alloying of powder mixtures followed by Mo/Nb powders. The microstructural of titanium and titanium alloy is exhibitedand discussed. The effect of temperature and time on the microstructure and properties have been also evaluated and the results related to this aspect are presented and discussed.

2. Experimental

In the present study, pure titanium and Ti-6Al–4V alloys were used as initial material. Titanium alloy has a chemical composition of 6% aluminum, 4% vanadium, 0.2% oxygen, and the remainder titanium. Chemical composition of Titanium alloy is shown in table 1.

Table 1. *Chemical composition of Titanium*

elements	Al	V	O	Ti
(wt.%)	6	4	0. 2	Balance

One of the most important properties of titanium is its modulus of elasticity. For the Ti α phase at room temperature, this value is about 115 Gpa, when the temperature increases it decreases linearly to 58 GPa at a temperature close allotropic transformation values [8, 9].
The microstructural characterization of titanium samples were observed by a Leo 1430 VP scanning electron microscopy (SEM) and optical microscopy (Optika B-600). The thicknesse measured by an optical microscopy are averages of at least 12 measurements.
The presence phase analysis was carried out at ambient temperature by Philips X-ray diffraction (XRD) analysis with a Cu Kα (λ= 1.5406 Å) source at 40 kV voltage and 30 mA current ranging from 20 to 90°.
Mechanical properties of the sintered compacts were evaluated by micro hardness measurements at ambient temperature. Vickers micro-hardness was estimated by indentation under load of 4.903 N (HV0.5) and dwelling time of 15 s. The indentation during hardness test was carried out randomly, wherein the distance between the indents was kept at least three times the size of the indent. The representative hardness value of the test specimen was an average of 20 indentations.

3. Results and discussion

XRD analysis was carried out toidentify the phases that compose the alloys. The XRD pattern representative of both the prealloyed Ti–6Al–4V powder and pure titanium blend is shown in Figure 1.

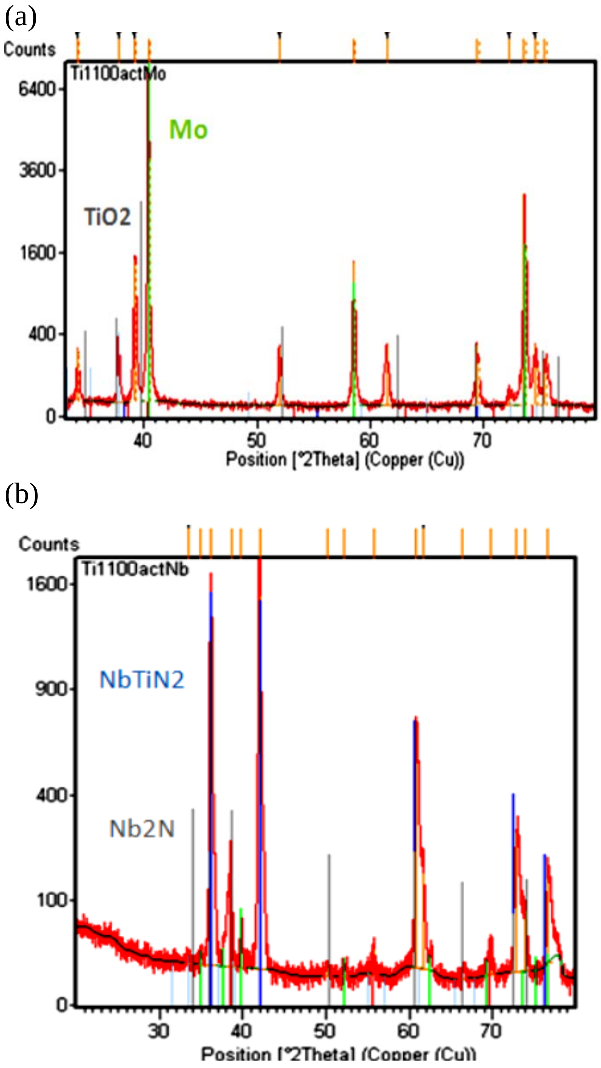

Figure 1.*XRD analysis at 1100°C for 4 h.*
(a) of Ti/Mo (b) of Ti/Nb

The main phase found during the XRD analysis of the powders is the alpha phase, although some beta phase and some aluminium/vanadium phase, indicating that the composition of the prealloyed Ti–6Al–4V powder is not completely homogeneous.
The microstructural evolution of the prealloyed Ti–6Al–4V powder during vacuum sintering over the range 1100-1200 °C. The microstructural analysis of the Ti–6Al–4V prealloyed samples sintered at 1100 °C shows that the sintering of the powder particles was already initiated, in agreement with the results of the dilatometric study were observed to disappear and the residual porosity was mostly irregular in shape. The microstructural analysis also indicates that the main microconstituent is the alpha phase.

Beyond this temperature reaches the value of the beta phase with not only good mechanical properties, but also a good corrosion resistance. The inability to have β phase of pure titanium at room or elevated temperature is not used too much titanium alloys with different elements for stabilizing the β phase. This is where the importance of unalloyed titanium, it can change its properties to suit a particular function and find states coexisting in α and β titanium phase. Titanium alloys are classified by the effect of the titanium alloy, if α phase supports, β, or maintained. This can be seen that α phase stabilizers as Al, N, O, or C phases, which can be seen from the phases diagrams that increasing the nconcentration of these elements in the temperature at which the β phase is greater than 882 °C [10, 11].

.

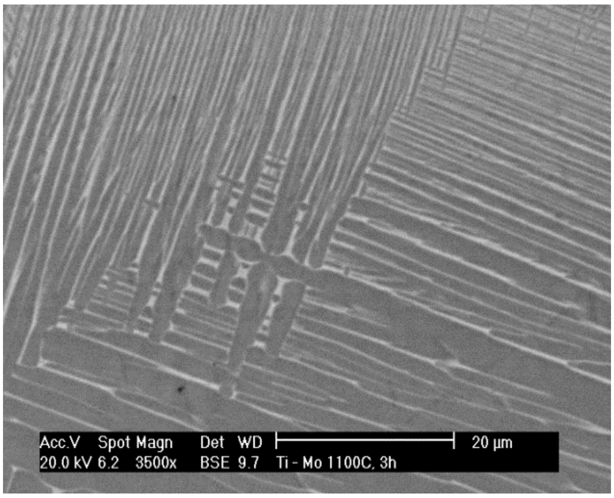

Figure 2. *Microstructural evolution of the prealloyed Ti–6Al–4V/Nb powder sintered under high vacuum at 1200 °C for 4h.*

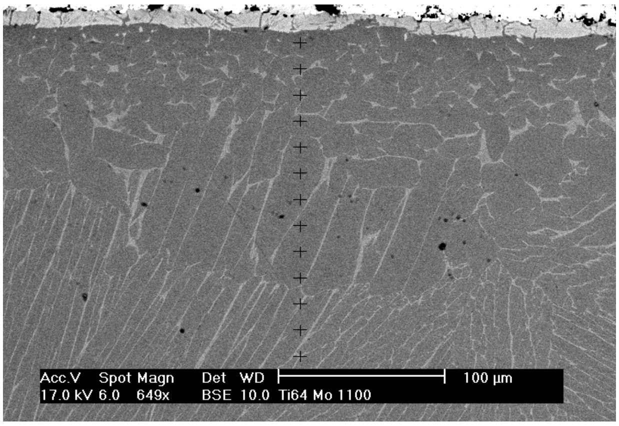

Figure 3. *Microstructural evolution of the prealloyed Ti–6Al–4V/Mo powder sintered under high vacuum at 1100 °C for 4h.*

Titanium alloys used are constituted of more than one phase diagrams ternary and quaternary alloy used instead. The titanium α phase is widely used for parts in contact with corrosive or oxidizing media, while α + β phase of the alloy known for its resistance.

The results of the EDS analysis of the two phases thatconstitute the microstructure of the Ti–6Al–4V alloy resemble those of the compositional analysis, where thevariation in the percentage of the alloying elements is due to the limited area of the zones analysed. EDS analysis of the zone where the diffusionof the alloying elements takes place in the Ti–6Al–4V alloy and pur titanium powderblend specimens during sintering at 1100 °C are similar tothose of the Ti–6Al–4V powder used to obtain the blend becausealuminium diffuses more quickly than titanium, and vanadiumis present only in isolated zones composed of lamellae. The microstructural evolution of the elementallyblended Ti–6Al–4V powder blend during vacuum treatment between 1100 °C and 1200 °C. The necking between the powder particles isinitiated at a sintering temperature of 1100 °C and XRD pattern shows that is representative of thesintered samples, particularly those processed at 1100 °C and 1200 °C.

The initial microstructure of the titanium surface is modified becoming lamellar α + β. Therefore, all the other experiments are simulated in the same manner. Besides in some areas of the part the different directions laminar growth, the meeting of two colonies of α + β formed by diffusion is shown in Figure 2.

The phases detected in the specimens at 1100 °C are titanium alpha and titanium beta which had already been detected in the starting powder. The XRD pattern of the specimens at 1100 °C confirms the results of the microstructural evolution and of the EDS analysis, indicating that the distribution of the alloyingelements is homogeneous because no Al_2V_3 peaks werefound. No significant difference can be observed in the XRD patterns of the specimens sintered at 1200 °C incomparison to those of the samples processed at 1100 °C. In contrast to α titanium properties are due to the orientation of the stress with respect to the workpiece due to the nature of the α structure. Ti alloys with Al as used in this experiment reproduces this effect is because aluminum acts by decreasing the unit cell parameters. The main forms of hard titanium add interstitial elements such as oxygen or nitrogen or the addition of substitution elements such as Al or Z. In the α + β alloys is three types of microstructure: kelp, equiaxed or bimodal containing equiaxed α structure in a matrix of α + β phase.

Figurie 3 shows the cross section of a Ti-6Al-4V sample of in which Mo has spread. At the top of the piece, molybdenum has spread by creating a layer of Ti in β phase, this was the goal of the project. Immediately this an area of phase α + β equiaxial, this is not the original Ti-6Al-4V structure since it has structure laminating. Finally the farthest part area maintains the structure laminating, it shows image of the porous titanium sample, titanium sample processed with space holder displays an interconnected porosity type with few closed pores and a higher pore volume fraction than the sample without space holder.

The properties of titanium with respect to α + β phase, α titanium mainly depends on their composition and then treating mechanism. In contrast to α titanium properties are due to the orientation of the stress with respect to the work piece due to the nature of the α structure. Ti alloys with Al, as used in this experiment reproduces this effect is because the aluminum works by reducing the unit cell parameters.

The main forms of hard titanium add interstitial elements such as oxygen or nitrogen or the addition of substitution elements such as Al and Zr. The α titanium alloys are among the most resistant structural materials than working in a corrosive environment. Especially in an oxidizing environment and weather resistant layer is created, if the room is in reducing environments then this layer is broken if you need to add inhibitors such as palladium. Due to its high performance in many corrosive titanium desalination for ships. As the part is used in heat exchangers, condensers, plants in many cases, in addition to being a corrosive liquid is exposed is at a high temperature that makes it should consider the high temperature corrosion and crevice corrosion. In addition of a little Mo is known to crevice corrosion resistance to corrosion and high temperature increases. However, the molybdenum phase for the α phase can not add more than 1% molybdenum, for if one enters the α + β phase.

In the α + β alloys is three types of microstructure: kelp, equiaxed or bimodal containing and equiaxed α structure in a matrix of α + β phase. For such structures, simply by performing an annealing treatment of the alloy at the end of treatment.

The most important process parameter is the ratio of cooling crystallization process, which will be determine by the characteristics of the lamellar structure and size of α phase, the thickness of layers in the edge or edges β and α zone colonized by the structure α. All these features reduce the cooling rate increases. Although it is also possible to obtain these structures without recrystallization of the material is not a very common form in reality. In the important of the annealing process is no longer the temperature time. A small area colonized by α phase is less effective slip planes causing an increase in the creep strength.

For the formation of these structures further processing is performed at a temperature lower than the temperature of β transits temperature of the α + β sample .In this case, what determines the thickness of the lamellar phase, α is the coolant report from homogenization. These alloys have better mechanical properties than the fully lamellar alloys with similar cooling ratios, except as regards the behavior or propagation of fatigue cracks, in a small area bimodal alpha colonized greater fatigue resistance as shown in Figure 3.

The upper part of the brightest sample of the coating layer is composed of Mo and Cu. In the contact between copper and the porosity sample exists. On the surface of the workpiece is a region where the α and β lamellar titanium coexistence phase, the latter being perpendicular to the direction of the sample surface.

In addition, in some areas of the laminar piece growth was different directions, the meeting of two phases α + β formed colonies presented by diffusion. Pure titanium powder has very high tendency to conglomerate and staff with the vial and balls during mechanical alloying.

The mechanical properties in this case is essentially influenced by the size of titanium grains in α phase over the border size have high creep. These analyzes the shape of α + β alloy is the theory, will later be applied to our special experience. For these small grain structures during the homogenization must have a strong cooling rate in the process.

The main feature of this type of alloy are its mechanical properties and having a high resistance in the tensile test, fatigue and fracture. The main characteristic of beta type alloys is that you can tighten to much higher values than α + β alloys can be worked a little cold. The process of obtaining this type of alloy is α + β equal to the alloy.

To achieve these alloys at temperatures below the temperature of β phase such alloys are used. To create these alloys must be used betagene elements such as Mo, Nb, V, Ni, Cu or Ta.

To improve the properties of these alloys are used to precipitate fine particles of Ti-α in the sample instead of being Ti β only. The ductility of the alloy is greater than β phase. Young's modulus of titanium alloy decreases, this activity is important in biomaterials because of the difference in Young's modulus of the bone.

SEM was obtained to measure the depth of diffusion zone, it was about 60 µm, therefore we can say that the previous calculations correspond to reality. It is due represents the percentage by weight of Mo and Ti with respect to the distance to the sample surface. The depth at which there is relevant percentages Mo about 60 µm.

The addition of activator affects diffusion. In the high surface areas are created and Mo as the distance to the surface decreases the size of these areas increased. One can appreciate that some porosity is because the chlorine has attacked activator part, due to titanium chlorides that form as predicted by thermodynamic calculations.

When the activator is added to the percentage of Mo near the surface of the sample is greater than when it is added but not turn the distance penetrated in the workpiece is lower. Then there one α + β laminar zone where the Nb concentration is decreasing.

Note that the presence of N in the sample, as in previous cases we have to use the activator NaCl. It was attached to the coating in small areas Ti β phase due to the high concentration of Nb DICTRA as predicted in both concentration and diffused away.

The size of the sample surface is increased. Therefore, without a preferred direction has managed to create a phase α + β laminar. Figure 3 shows the electro disposition of titanium with Nb diffusion to 1100 °C for 3 h. By adding N activator experiments in 1100 in contrast no oxide layer, there is a large area with high content of Nb. In this area there Ti in the β phase is the objective of the experiment, at the bottom of this layer is a layer with some of a large N. The analysis of the sample surface shown by XRD the surface is composed of the compounds $NbTiN_2$ and Nb_2N. This result is consistent with the results of the SEM.

Figure 3 shows the cross section of a sample of Ti-64, which has spread Mo. At the top of the piece-disseminated molybdenum creating a layer of Ti in β phase, this was the goal of the project. Immediately this area α + β phase equiaxed, this is not the original structure of Ti-64 since it has laminar structure. Finally the farthest part area holds the laminate structure.

By employing as Ti-64 substrate it has a surface layer rich in Nb, over a layer of oxide with a content of Cu coating. There is a Ti layer with α + β due to the presence of V in the lower part of the oxide layer. The spread of V creates a layer of Ti-α.

The activator in experiments at 1100 °C creates a porous layer due to the attack of Cl Ti as expected due to thermodynamic calculations. activator is more effective in the experiences of Nb and Mo in the gaseous species formed Nb are more likely than those formed of Mo, this experience was calculated and was corroborated. The simulation experiment and approach to the dissemination of Mo and Nb.

Therefore, it has been ratified that DICTRA as a program adapted to simulate the spread if the experiment proper discharge of the defined objective. The diffusion of Mo and Nb in titanium and titanium alloy their original microstructure are changed on the surface becoming α + β phase. DICTRA simulation using the Mo diffusion experiment is not very accurate by the model used, while the model used for calculating Nb itself which corresponds to reality.

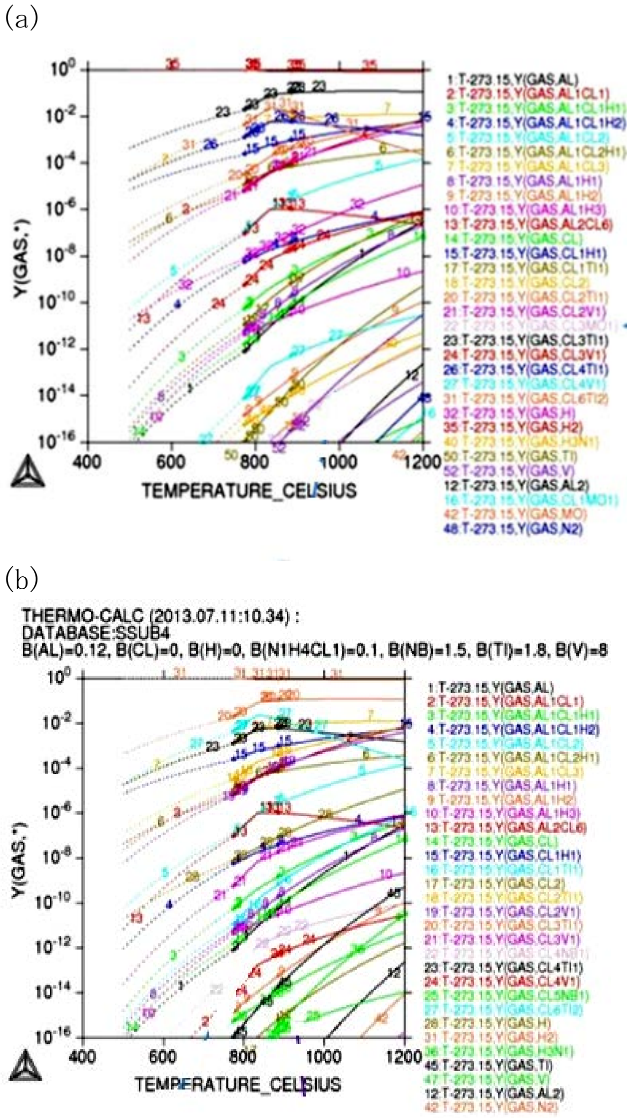

Figure 4. *probable gaseous species in experiments at 1100 °C for 4h. (a) for Mo (b) for Nb.*

Hence, the remaining experiments are simulated in the same manner.

It is achieved create a β phase layer on the surface of the samples. In addition, the microstructure of the sample is changed α + β laminar to α + β equiaxed. The simulation experiment and disseminating coming Mo and Nb as shown in Figure 4.

The activator in experiments to 1100 °C creates a porous layer due to the attack of NaCl.

The activator is effective in experiments in Nb and Mo as the gaseous species, it us formed of Nb more than it is formed of Mo, this resulat was calculated and experiments corroborated it with DICTRA predicted that the Nb would not spread in the experiments at 1100 ° C and dissemination not predicted or using the activator. Instead DICTRA if predicted 30 µm to spread in spreading Mo, but the reality was different because it does not disseminated in any experiment.

Therefore it has been ratified DICTRA as an appropriate program to simulate spread if the experiment is properly defined fulfilling the target.

3. Conclusion

The following conclusions can be obtained from the results of characterisation of the prealloyed Ti–6Al–4V and elementally blended powders and their microstructural evolution:

– The titanium powder metallurgy industry needs morereliable powders that can be usedto obtain final products or that can be employed as masteralloys to add the alloying elements desired.

– By using a prealloyed powder, the interaction of elementalTitanium with elemental aluminium, which generatesintermetallic $TiAl_3$, is avoided.

– The conventional powder metallurgy route of pressing andsintering can be exploited for the fabrication of titaniumproducts starting from irregular prealloyed powder orelementally blended powder using a master alloy.

– Various relative densities, between 83% and 95%, porestructures and grain sizes can be obtained by selecting aproper sintering temperature, but when the alloying elements have to diffuse to homogenise the composition, aminimum temperature of 1200 °C should be selected.

– Higher flexural strength and hardness in comparison tothe values specified for biomedical devices obtained bymeans of conventional metallurgy are obtained.

Acknowledgement

Author thanks the financial support of Algerian Ministry of Science through the Project J0300820120017 and Laghouat university.

References

[1] B. Gasser “Design and Engineering Criteria foraTitanium Device” Titanium in Medicine Springer Germany 2001.

[2] W. Ho, C. Ju, J. Chern Lin “Structure and properties of cast binary Ti–Mo alloys” Biomaterials 20 (1999) 2115–2122.

[3] C.H. Park, J.Park,J.Yeom “Enhanced mechanical compatibility of submicrocrystalline Ti -13Nb–13Zr alloy” Mater. Sci. Eng. A 527 (2010) 4914–4919.

[4] M. Peters, J. Hemptenmacher, J. Kumpfert, C. Leyens “Structure and properties of titanium and titanium alloys” Titanium and Titanium alloys – Fundamentals and Applications, WielyVCH, Weinheim (2003) 1-3.

[5] S. Nang, R. Banerjee, Stechschulte“Comparison of microstructural evolution in Ti–Mo–Zr–Fe and Ti–15Mo biocompatible alloys” Mater. Sci. Mater. Med. 16 (2005) 679–685.

[6] M. Karthega, V.Raman, N. Rajendran“Influence of potential onthe electro-chemical behaviour of titanium alloys in Hank’s solution” Acta Biomate. 3 (2007) 1019.

[7] L. Bolzonin, P.G. Esteban, E.M. Ruiz-Navas, E. Gordo “Mechanical behaviour of pressed and sintered titanium alloys obtained from prealloyed and blended elemental powders” mechanical behavior of biomedical materials 14 (2012) 29–38.

[8] R. Karre, Manish K. Niranjan, Suhash R. Dey, First Principles theoretical investigations of low Young’s modulus beta Ti-Nb and Ti-Nb-Zr alloys compositions for biomedical applications, J. Mater. Sci. Eng. 50 (2015) 52-58.

[9] C. shang, M. Bououdina, Z.X. Guo, Structural stability and dehydrogenation of (MgH_2+Al, Nb) powder mixtures during mechanical alloying, J. Mater. Tran.,11 (2003) 2356 - 2362.

[10] K. Tokumitsu, Mechano-chemical reaction of Niobium with decalin and teralin Hydrogenation of Niobium with Decalin and teralin, Catalysis Today 28 (1996) 99-103.

[11] J.J. Xu, H.Y. Cheung, S.Q. Shi, Mechanical properties of titanium hydride, J. Alloys and Compounds 436 (2007) 82-85.

International Journal of Computational and Experimental Science and Engineering (IJCESEN)
Vol. 2-No.1 (2016) pp. 25-29
http://dergipark.ulakbim.gov.tr/ijcesen

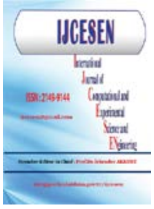

***ISSN:* 2149-9144**

Copyright © IJCESEN

Research Article

Steady state analysis of DFIG wind turbine using Matlab#

Gazmend KABASHI^1, Skender KABASHI^2*, Besnik SARAMATI^3 and Valon VELIU^4

^{2,3} Universit of Prishtina,Department of Physics, Prishtina -Kosovo
^{1,4}Universit of Prishtina,Department of Electrical Enginering, Prishtina –Kosovo,

* Corresponding Author : skender.kabashi@uni-pr.edu

Presented in ”2nd International Conference on Computational and Experimental Science and Engineering (ICCESEN-2015)”

Keywords
DFIG
MATLAB
Power Balance
Wind Energy

Abstract: In this paper the steady state electric circuit of the DFIG is developed, deriving the steady state model electric equations along with its physics. By means of these model equations, Matlab m-file for steady state calculations is developed. The modes of operation of the machine for different rotor speeds are presented and analyzed. Finally, based also on the Matlab calculations, a detailed performance evaluation of the DFIG is carried out, developing steady state performance curves that can reveal current, voltage, power balance, power losses, depending on the specific operating mode of the machine.

1. Introduction

Over the last years, there has been a strong penetration of renewal energy resources into the power system. Wind energy generation has played and will continue to play a very important role in electric energy sector for the coming years. Doubly fed induction generator (DFIG) based wind turbines have arisen as one of the leading technologies for wind turbine manufacturers, demonstrating that it is a cost effective, efficient, and reliable solution [1]. This machine, a key element of the wind turbine, is also known in the literature as the wound rotor induction machine, or asynchronous machine. It presents many similarities with the widely used and popular squirrel cage induction machine However, despite the parallelism of both machines, the DFIG requires its own specific study for an adequate understanding. DFIG used for wind turbines is basically a standard, wound rotor induction generator with a voltage source converter connected to the slip-rings of the rotor [2]. The stator winding are coupled directly to the grid and the rotor winding is connected to power converter as shown in figure 1. This configuration is especially attractive as it allows the power electronic converter to deal with approximately 30% of the generated power, reducing considerably the cost and the efficiency compared with full converter based topologies. Most manufacturers adjust the synchronous speed to be centred in the middle of the variable speed operation range 1500 rpm for two pole generators in wind turbines with a variable speed range from 1000 to 2000 rpm), which means that the machine, working at sub-synchronous and hyper-synchronous speeds with positive and negative torques, needs to be fed by a four-quadrant power electronic converter [3]. The standard power electronic converter used in this application is a back-to-back converter composed of two three-phase inverters sharing the DC bus. At present, most manufacturers uses two-level converters with standard IGBTs in order to reduce the cost for the 1.5 to 3 MW wind turbines; but for the most powerful offshore ones (3 to 10 MW), three-level converters are expected to be the best option.

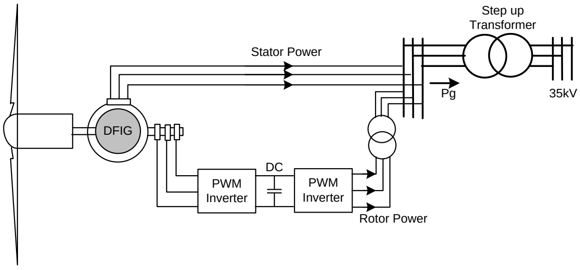

Figure 1. *Double-Fed Induction Generator.*

2. Steady state DFIG model

To investigate the power balance and eficiency of DFIG in stady state operation regime the equivalent circuit shown in figure 2 can be used. The rotor quantities are referred to the stator. The reverse rotor current direction is used to facilitate the analysis of DFIG wind turbine, where the rotor circuit is connected to a power converter system with bidirectional power flow. The rotor side convertor is modeled as equivalent impedance. In developing model it is assumed that the induction generator is symmetrically structured and three phase are balanced, and the magnetic core of the stator and rotor is linear with negligible magnetic resistance. In this paper is considered the case that the generator operates with an Maximum Power Point Tracking scheme, and its mechanical torque is proportional to the square of the rotor speed [4,5].

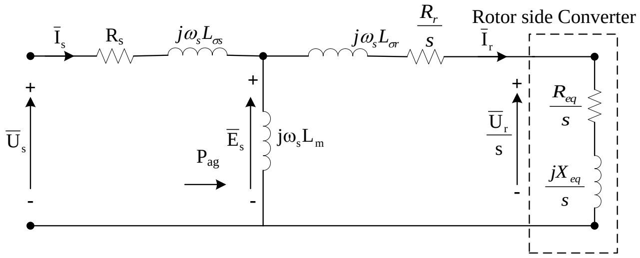

Figure 2. *Steady state equivalent circuit of the DFIG*

To investigate steady state analysis of DFIG we assumed that stator operates with $\cos\varphi = 1$.The air-gap power, stator current and magnetizing voltage branch of inductive generator can be calculated by expressions:

$$P_{ag} = \frac{\omega_s T_m}{p} = 3 \cdot (U_s - I_s R_s) \tag{1}$$

$$I_s = \frac{U_s \pm \sqrt{U_s^2 - \frac{4 R_s \omega_s T_m}{3p}}}{2R_s} \tag{2}$$

$$\bar{U}_m = \bar{U}_s - \bar{I}_s (R_s + j\omega_s L_{ls}) \tag{3}$$

For $\cos\varphi = 1$, where inductive machine operating in generation mode for the stator voltage and current we can write:

$$\bar{U}_s = U_s \angle 0^0 \text{ and } \bar{I}_s = I_s \angle 180^0 \tag{4}$$

The magnetizing current is given by:

$$\bar{I}_m = \frac{\bar{U}_m}{j\omega_s L_m} \tag{5}$$

The rotor current and voltage are given by:

$$\bar{I}_r = \bar{\bar{I}}_s - \bar{\bar{I}}_m \tag{6}$$

$$\bar{U}_r = s\bar{\bar{U}}_m - \bar{\bar{I}}_r (R_r + js\omega_s L_{lr}) \tag{7}$$

The equivalent impedance of rotor side converter can be calculated by:

$$\frac{\bar{U}_r}{\bar{I}_r} = R_{eq} + jX_{eq} \tag{8}$$

3. Matlab m-file for power balance analysis of DFIG in steady state operation regime

. We considered 5 MW, 950 V, 50 Hz, 1170 rpm, wind turbine of DFIG type which parameters are shown in table 1. The purpose of this example is to assess specific numerical calculations and graphical presentation of the impact of the rotor slip, to the electrical and mechanical variables as well as the power balance, power losses of DFIG-s. Application program Matlab is used for the calculation and graphical and numerical presentation [7]. For this case the specific m-file in Matlab is developed based on 5 MW DFIG parameters and from steady state equations obtained by the equivalent model of DFIG shown in figure 2. The m-file program automatically calculate and graphically present the diagrams of selected complex variables versus of rotor speed ωr which changes in the range (600- 11200) rpm with speed increment of $\Delta\omega_r = 1$ rpm. This program can also be used for DFIG with different size and capacity, if we know in advance its parameters.

Table 1. *5 MW, 950 V, 50 Hz DFIG parameters[4]*

Generator Type	DFIG, 5.0 MW, 950 V
Rated mechanical power	5 MW
Rated stator voltage, U_s	950 V
Rated stator current, I_s	2578.4 A
Rated rotor current, I_r	3188.7 A
Rated Rotor Speed	1170 rpm
Nominal Rotor Speed	670 – 1170 rpm
Rated Slip	-0.17
Number of Pole Pairs, p	3
Rated Mechanical Torque T_m	40.809 kNm
Stator Winding Resistance, R_s	1.552 mΩ
Rotor Winding Resistance, R_r	1.446 mΩ
Stator Leakage Inductance, L_{ls}	1.2721 mH
Rotor Leakage Inductance, L_{lr}	1.1194 mH
Magnetizing Inductance, L_m	5.5182 mH

Bellow is presented m-file script for steady state calculations of DFIG in Matlab:

```
% MATLAB m-file  for steady state analysis of 5MW, 950V,50Hz DFIG wind turbine
 Ub=950/sqrt(3); Ib=3118.7;  % Base [V] and  [A]
Us_=548.5+0i;  % Stator phase to ground  [V]
Rs=0.001552; Rr=0.001446;    % Stator and rotor winding resistance [ohm]
ws=2*pi*50;p=3;     % Stator frequency [rad/s] and number of poles
Los=0.0012721;Lor=0.0011194;     % Stator and rotor leakage inductance  [H]
Lm=0.0055182;     % Magnetizing inductance [H]
wrt=600:1:1200;  % Range and Step time calculation
wr=2*pi*p*wrt/60;   %angular electrical frequency of rotor  [rad/s]
Tmn=-(1000/1150)^2*40809; % Rated mechanical torque for s=0 [Nm]
s=(ws-wr)/ws      % slip
Tm=(wr/ws).^2*Tmn   % Mechaniqal torque  [Nm]
Is_=-(Us_-sqrt(Us_.^2-(4*Rs*ws*Tm)/(3*p)))/(2*Rs)*exp(i*pi)         % Stator  current [A]
Is=abs(Is_)      % Magnitude [A]
Ispu=Is/Ib        % Stator current pu.
thetaIs_=angle(Is_)*180/pi    % stator current angle [degree]
Um_=Us_-Is_*(Rs+i*ws*Los)    % Magnetizing branch voltage [V]
Um=abs(Um_)       % Magnitude [V}
thetaUm=angle(Um_)*180/pi       % Magnetizing branch voltage [degree]
Im_=Um_/(i*ws*Lm)    % Magnetizing current [A]
Im=abs(Im_)        % Magnitude [A]
thetaIm=angle(Im_)*180/pi  % Magnetizing current angle [degree]
Ir_=Is_-Im_      % Rotor current [A]
Ir=abs(Ir_)      % Magnitude [A]
Irpu=Ir/Ib        % Rotor current [pu.]
thetaIr=angle(Ir_)*180/pi  % Rotor current [degree]
s1=s;
Ur_=s1.*Um_-Ir_.*(Rr+i*s1*ws*Lor)    % Rotor voltage phase to ground [V]
Ur=abs(Ur_)        % Magnitude [V}
Urpu=Ur/Ub        % Rotor voltage [pu.]
thetaUr=angle(Ur_)*180/pi  % Rotor voltage angle [degree]
Zeq_=Ur_./Ir_ % Zeq of Rotor S.Conv. [ohm]
Req=real(Ur_./Ir_)
Xeq=imag(Ur_./Ir_)
powfac_rot=angle(Zeq_)*180/pi    % Rotor power factor angle [degree]

%POWER BALANCE
Prot=(3*(Ir).^2).*Req      % Rotor power [W]
Pstator=3*Us_.*abs(Is_).*cos(angle(Us_)-angle(Is_))  % Stator power [W]
deltaProt=3*(Ir).^2*Rr  % Rotor power losses [W]
deltaPstator=3*(Is).^2*Rs  % Stator losses [W]
Pg=Pstator-Prot     % Pg of 5 MW  DFIG [W]
Pmek=Pg+abs(deltaProt)+abs(deltaPstator)   % Rotor mechanical power [W]

%Graphical results
subplot(5,1,1);plot(s,thetaUr,s,thetaIr,s,powfac_rot);
subplot(5,1,2);plot(s,Irpu,s,Ispu,s,Urpu);
subplot(5,1,3);plot(s,Req,s,Xeq);
subplot(5,1,4);plot(s,deltaProt,s,deltaPstator);
subplot(5,1,5);plot(s,-Prot,s,Pstator,s,Pg);
```

4. Simulation results and discussion discussions

After m-file MATLAB execution we have the graphical results and numerical results as shown in figures 3,4, 5 and table 2

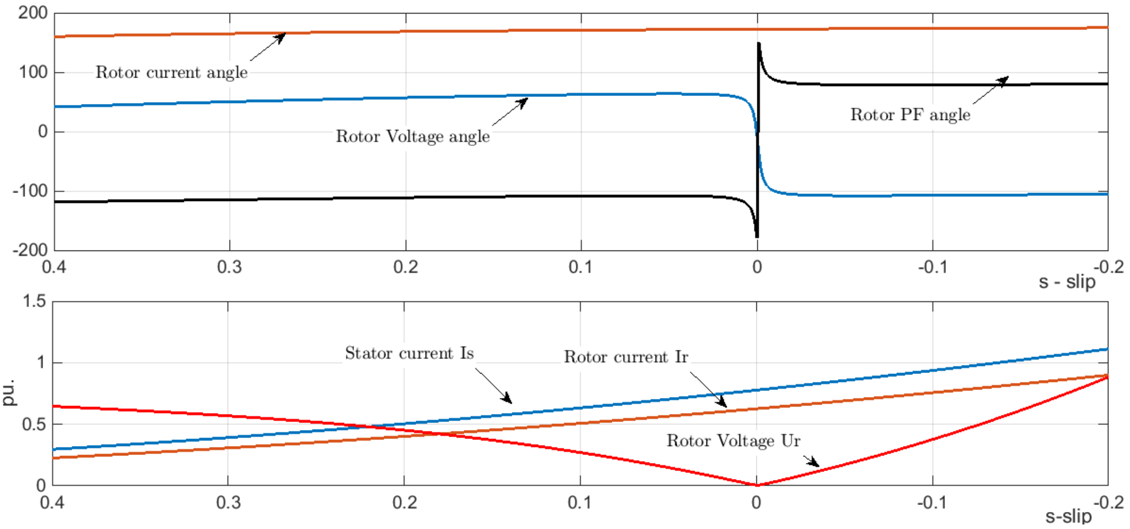

Figure 3 *Voltage and currents versus generator slip s.*

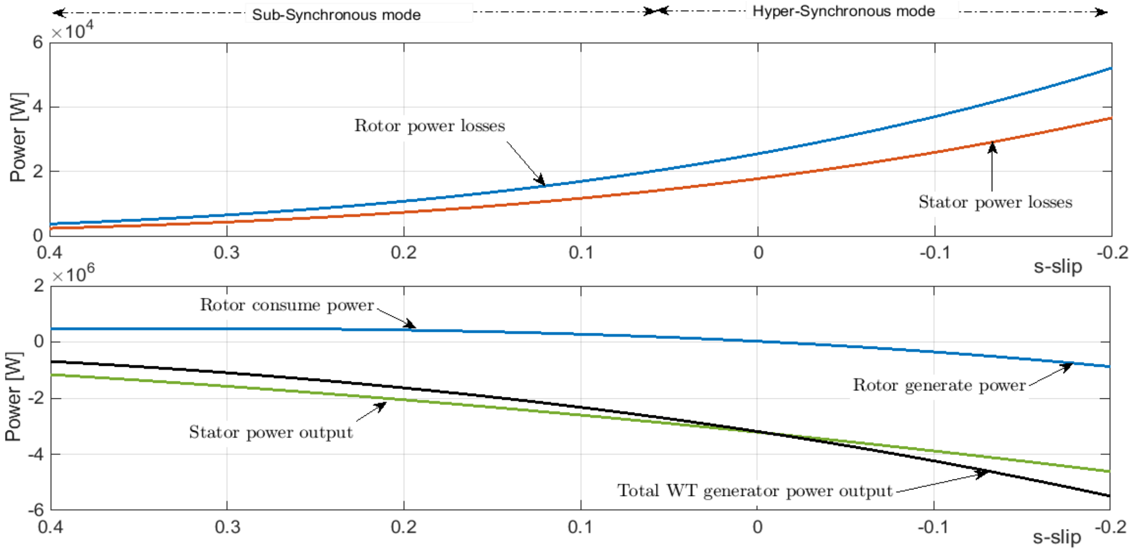

Figure 4 *Rotor, stator and generator power versus generator slip (s) for* $\cos\varphi = 1$

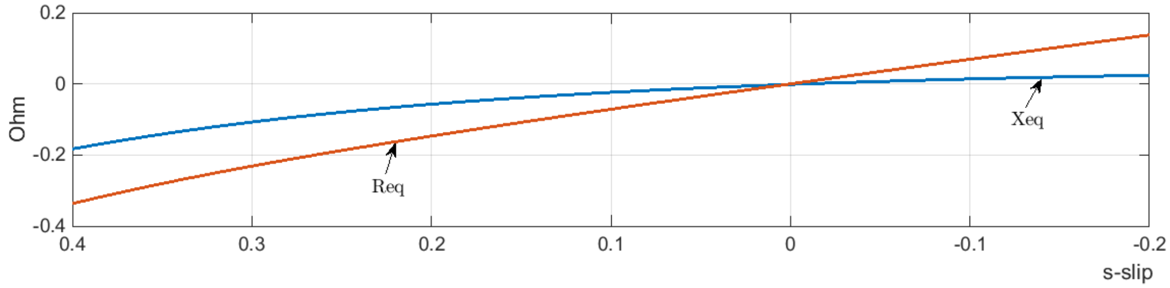

Figure 5 *Rotor side converter equivalent impedance versus generator slip (s) for* $\cos\varphi = 1$

Table 2 *Power output, losses and efficiency of DFIG for different rotor speeds*

Speed [rpm]	s-slip	Pg [kW]	ΔP_r [kW]	ΔP_S [kW]	Efficienc [%]
1170	-0.17	5000	43	47	98.4
1000	0	3188	17.8	25.5	98.6
800	0.2	1636	7.3	10.7	98.8
670	0	963	5.5	3.6	99.0

Table 3 *Voltage and current phases of DFIG for different rotor speeds*

Speed [rpm]	$\underline{Us}$ [V]	$\underline{Ur}$ [V]	$\underline{Is}$ [kA]	$\underline{Ir}$ [A]
1170	$548e^{j0}$	$398e^{-j105}$	$2668e^{j57}$	$3298e^{j174}$
1000	$548e^{j0}$	$3.5e^{-j7}$	$1953e^{j180}$	$2424e^{j172}$
800	$548e^{j0}$	$248e^{j57}$	$1252e^{j180}$	$1573e^{j168}$
670	$548e^{j0}$	$326e^{j47}$	$248e^{j57}$	$1127e^{j163}$

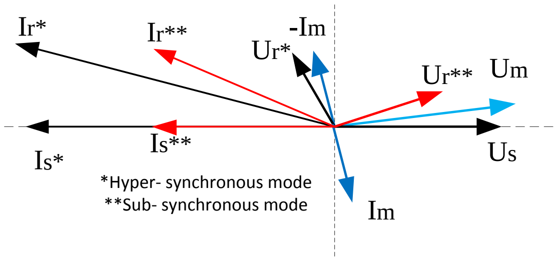

Figure 6 *Phase diagram of DFIG obtained by table 2 results*

It is essential to note that the generator slip s, respectively, the rotational speed of wind turbine determines operating character of DFIG. Analysing the graphical and numerical results, from figure 3 it can be shown that with the increase of the rotor angular speed from 600 rpm (s = 0.4) to the synchronous speed 1000 rpm (s = 0), the rotor voltage U_r decreases gradually near to the zero, and above synchronous speed the rotor voltage increases almost linearly to the certain value. It should be noted that the rotor calculated values of current and voltage are referred to the stator, which means that the real values of voltage and current in the rotor for the given 5 MW DFIG , should be transformed through rotor/stator winding ratio u = $U_{rn}/U_{sn}=381/548.48=0.694$.

In figure 3 is shown also the phase angle of rotor voltage, rotor current and rotor power factor angle. In sub-synchronous mode of operation the power factor angle of rotor is negative, indicating that the rotor absorbs power from the grid, while in the hyper-synchronous mode of operation rotor inject power to the grid.

When DFIG operates at synchronous speed ($s = 0$) induction generator behave like synchronous generator. The rotor absorbs only small amount of power which is needed for excitation, and practically does not share power with the grid as is shown in figure 4. For $s=0$ the rotor leakage reactance and equivalent reactance of RSC are both zero. In this case the DFIG generated power is transferred through stator.

The rotor and stator losses increase proportionally to the square of the rotor and stator currents. In the sub-synchronous mode of operation the DFIG generated power $Pg < Ps$, due to the rotor power consumption, while in the hyper-synchronous operation both rotor and stator generate power and $Pg > Ps$ The results presented above confirm the advantages of the DFIG wind turbine concept. In contrast to the constant speed wind turbine, DFIG generates power even for $s > 0$.

In figure 5 is shown the diagram of the equivalent resistance and reactance of the rotor side converter in dependence to the slip s. When the DFIG operates in the sub-synchronous mode the equivalent resistance of RSC is negative, indicating that rotor absorbs active power from RCS, while when DFIG operates in hyper-synchronous mode equivalent resistance is positive, meaning that an active power is delivered from rotor to the RSC, respectively to the grid. The negative sing of equivalent impedance of RSC is not a physical concept, but mathematically shows the change of rotor power flow direction.

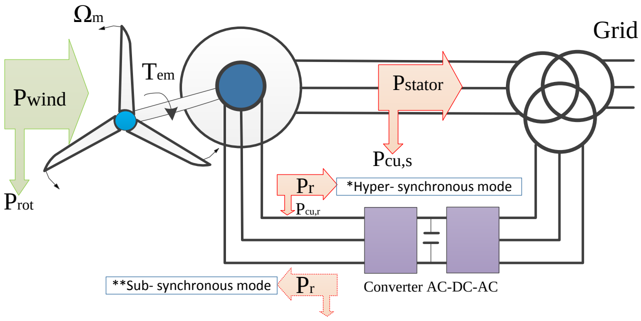

Figure 7 *Power balance illustration of DFIG based on different operational modes*

In table 3 are presented numerical results of DFIG power balance, and figure 6 shows phase diagrams of current and voltages obtained by table 2 numerical results corresponding to the operation modus of DFIG.

Figure 7 illustrates power balance of DFIG depending of operational regime in regard with sub or hyper synchronous mode.

5. Conclusion

In this paper, the steady state equivalent circuit for DFIG is presented and analysed, and the rotor side converter (RSC) is modeled by an equivalent impedance. The operating principle of the doubly fed induction generator (DFIG) with unit power factor operation are presented and analyzed. For the study case the 5 MW DFIG wind turbine is selected and based on the mathematical equations the Matlab m-file is developed. Finally, based on the Matlab calculations, a detailed performance evaluation of the DFIG is carried out, developing steady state performance curves of current, voltage, power balance, depending on the specific operating mode of the machine.

References

[1] Skender Kabashi, Sadik Bekteshi, Skender Ahmetaj, Gazmend Kabashi, Dimitrij Najdovski, Aleksander Zidanšek, et al. “Effects of Kosovo’s energy use scenarios and associated gas emissions on its climate change and sustainable development” Applied Energy, 2011, vol. 88, issue 2, pages 473-478

[2] G.Kabashi K.Kadriu A.Gashi, S.Kabashi, G,Pula, V.Komoni “Wind Farm Modeling for Steady State and Dynamic Analysis” , World Academy of Science, Engineering and Technology , www.waset.org/journals, pp 262-267.

[3] Thomas Ackermann, “Wind Power in Power Systems”. John Wiley & Sons, The Atrium, Southern Gate, Chichester, West Sussex PO19 8SQ, England, 2005

[4] BinWu, Yongqiang Lang, Navid Zargari, Samir Kouro, Power conversion and control of wind energy systems Published 2011 by John Wiley & Sons, Inc., Hoboken, New Jersey.

[5] A. E. Fitzgerald, Charles Kingsley,Jr. , Stephen D. Umans, Electric Machinery, McGraw-Hill Book Company, 1992, ISBN 0-07-112946-4.

[6] R. Abari at all. Doubly fed induction machine : modeling and control for wind energy generation. IEEE Press, 2011, 445 Hoes Lane Piscataway, NJ 08854

[7] Wolf Dieter Pietruszka, MATLAB und Simulink in der Ingenieurpraxis. Modellbildung, Berechnung und Simulation, B. G.Teubner Verlag / GWV Fachverlage GmbH, Wiesbaden 2006, ISBN 978-3-8351-0100-5

International Journal of Computational and Experimental Science and Engineering (IJCESEN)
Vol. 2-No.1 (2016) pp. 30-37
http://dergipark.ulakbim.gov.tr/ijcesen

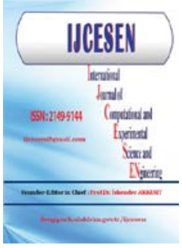

Copyright © IJCESEN

***ISSN:* 2149-9144**

Research Article

Need of Traceable Force Measurements in Steel Industry in Meganewton Level Forces[#]

Sinan FANK*, Bülent AYDEMİR

TÜBİTAK Ulusal Metroloji Enstitüsü, P.O. Box 54, 41470, Gebze-Kocaeli, Turkey,

* Corresponding Author : sinan.fank@tubitak.gov.tr

[#] Presented in ”2nd International Conference on Computational and Experimental Science and Engineering (ICCESEN-2015)”

Keywords
Force transducer
traceability
force machine
calibration

Abstract: In mechanical engineering, aerospace industry, energy industry, builting industry, safety engineering and testing, forces with nominal values in excess of 15 MN are measured. When we come to steel industry, need of MN level force measurements reach up to 100 MN level forces. Especially in rolling, pressing and extrusion process in steel and iron industry uses the MN level forces which are used in process control and development of high quality products. For this reason, MN level force should be measured reliably and accurately in iron and steel industry for repeatable products. In order to get reliable and accurate measurement results from the force measuring devices, they need calibrations traceable to international force standards. In this study, needs on MN level force measurements in iron and steel industry and subjects on traceable force measurements will be discussed.

1. Introduction

In recent years, It is understood that the process control is much more effective, efficient and productive during the manufacturing process of the products instead of one by one control of the finished products. Beside this, measurement systems are essential to perform process control in production line for continuous control to keep the production rate in high levels and to decrease the number of unexpected or waste products. For these reasons, force measurement is one of the most important parameter in process control, especially in steel industry. Competition in industry oblige the producers applying test on their products to present more reliable and high-quality products to the society to increase the market share and reliability. In these tests, different type material testing machines (MTM) and their equipments are used to check technical specifications of the materials and finished products. These MTMs measure the applied forces on the materials and products during tests. In order to get reliable measurement results from the MTMs and other test equipments, traceable force measurements are very important to get accurate and reliable results for all applications. Traceable measurements mean applying calibration of the measurement/test devices using well known reference standard to determine measurement uncertainty of them [1-4].

Nowadays, the force measurements are needed in many field of industry. Especially accurate force measurements are required in many applications. These include the determination of the strength of materials, quality control during production, weighing, and consumer safety. For example, force measurement systems are used to determine when a missile has developed sufficient thrust to be released for take off and in auto safety tests. In the aircraft industry, force measurements are required to test the structural integrity of aircraft components

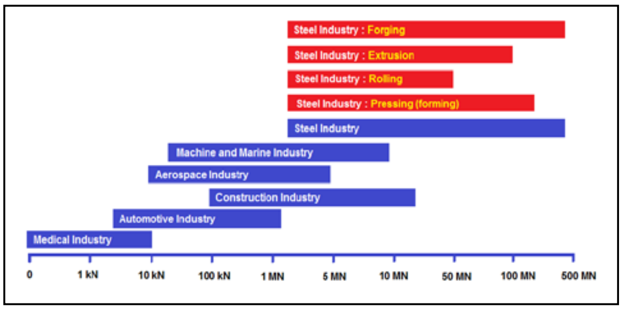

Figure 1. *Need of force measurement in different industries*

and structures. They are used to test the structural integrity of the wings, fuselage, and fasteners used in aircraft production. Similarly, accurate force measurements are required to determine the weight of vehicles, tanks, bins, ladles and hoppers. Force sensors (load cells) are used in electronic balances to measure weight. Such balances include those used to weigh trucks on highways, freight cars on railroads, many weighing applications and the flow of materials in a production process [5-6].

In steel industry, forging, rolling, pressing and extrusion process need also accurate force measurements. Automated industrial processes such as rolling mills require accurate force measurement to control roll pressure on bar steel, plates, sheet metal, etc. for the production of required technical specifications and repeatable products manufactured in different times ordered by costumer. Need of force measurements in different industry are shown in Figure 1.

A measurement technology offering high accuracy is a prerequisite today in steel industry for modern rolling, pressing and extrusion process. The constant striving to achieve optimum process quality and the highest possible productivity is essential goal of modern production units.

A truly measured force is crucial in achieving correct setting of production systems for optimum force distribution, correct force application to the material is beneficial to save of energy of production systems and less waste products and time consuming and etc.

In order to be able to make reliable and accurate force measurements using force measuring devices (force proving instruments) such as force transducers, load cells, dynamometers, proving rings, the traceable calibration of them are necessary and very important for reliability of the measurement results. For the calibration of force proving instruments well known standard forces should be generated by the force standard (calibration) machines (FSMs).

MegaNewton (MN) level force measurements are needed in numerous fields of industry such as aerospace, machine, marine, railroad and all other industries need higher forces up to 30 MN [3]. Especially in metal industry, MN level force measurement reaching up to 100 MN (10.000 tons-force) are used to control the processes in rolling, extrusion and pressing operations to specify a quality standard and to improve the productivity. In this study, MN level force applications especially in metal industry and the importance of traceable force measurements on controlling the process will be explained.

2. Need of MN Level Force in Steel Industry

A branch of heavy machine builting and steel industry produces various metal products (ranging from machine parts to household items) by forging, rolling, pressing and extrusion. The processes are based on the deformability of the materials, that is, on their ability to change their shape without destruction under the influence of external forces. Conditions favourable for plastic deformation are selected according to the fundamental principles of the theory of metal working by pressure. The value of forging and stamping methods is that the shape of the stock changes as a result of redistribution of metal rather than removal of excess metal, as in machining, which makes possible a sharp reduction in waste and a simultane ous increase in the strength of the material [7-8].

Therefore, metal working by pressure is used for the manufacture of very critical machine parts: 80-90 percent of the parts in aircraft and up to 85 % of the parts in automobiles (in terms of total weight) are made by pressing. Forging and pressing machines are more efficient than metal cutting machines; for example, the capacity of cold-heading machines is 5-6 times greater than that of automatic turning lathes, and metal waste is reduced by a factor of 2-3. For each million tons of rolled metal processed, 250,000 tons of metal can be saved with the use of mechanical stamping. [7]

Forging Forces

Forging process in which the workpiece is shaped by compressive forces applied through various dies and tooling. It is used for products weighing up to 200 tons. Hydraulic forging presses with forces of 2-200 Meganewtons (MN), or 200-20, 000 tf. Forging stock is formed directly by the upper face of a stamp or by very simple accessories and forging tools. Presses are used for forming, forging and stamping processes. Mechanical presses crank or eccentric shaft driven, or knuckle-joint for very high forces; stroke limited apply forces on 2.7-107 MN (300-14,000 tf) forces. Hydraulic Presses constant speeds, load limited, longer processing times, higher initial cost than mechanical presses but require less maintenance apply forces on 125 MN (14,000 tf) open die, 450 MN (50,000 tf) closed die. Friction screw presses–flywheel driven, energy limited (if dies do not completely close, cycle repeats) apply forces on 1.4-280 MN (160-31,500 tf) [7-8].

Pressing (Forming) Forces

In order to forming of the metallic plate and sheet material, pressing is essential tool for metal industry.Pressing is a method of producing products made from various types of profiles, sections, bars, and pipes in which the forging stock is placed in a special container, from which it is extruded by a punch (press plunger) through the opening of a die that has the shape of the intended product. Application of known pressing forces during pressing process is very important for determination of optimum force and it causes high quality products with low energy consumption. At the same time causes long life moulding due to low friction forces with optimum force application. Pressing is done on hydraulic presses with forces up to 200 MN (20,000 tf) [7].

Rolling Forces

Metal rolling is one of the most important manufacturing processes in the modern world. The large majority of all metal products produced today are subject to metal rolling. Metal rolling is often the first step in creating raw metal forms. Metal rolling is plastically deformed by compressive forces between two constantly spinning rolls. This force act to reduce the thickness of the metal and affect its grain size. The ingot or continuous casting is hot rolled into a bloom or a slab; these are the basic structures for creation of a wide range of manufactured forms. At a rolling mill, blooms and slabs are further rolled down to the intermediate parts such as plate, sheet, strip, coil, billets, bars, and rods. Many of these products will be starting materials for subsequent manufacturing operations such as forging, sheet metal working, wire drawing, extrusion and manufacturing. Blooms are rolled directly into I beams H beams, channel beams and T sections for structural applications. Rails are rolled directly from blooms. Plates and sheets are rolled from slabs and are extremely important in the production of wide range of manufactured items. It is important to understand the significance of metal rolling in industry today [8]. Rolling is done on rolling machines with forces up to 60 MN (6,000 tf) [7].

Figure 2. *A wiev from forging press and proces*

Extrusion forces

is the process by which a block/billet of metal is reduced in cross section by forcing it to flow through a die orifice under high pressure (compression force).

In general, extrusion is used to produce cylindrical bars or hollow tubes or for the starting stock for drawn rod, cold extrusion or forged products. Most metals are hot extruded due to large amount of forces required in extrusion. Complex shape can be extruded from the more readily extrudable metals such as aluminium.

Figure 3. *185 MN forging press*

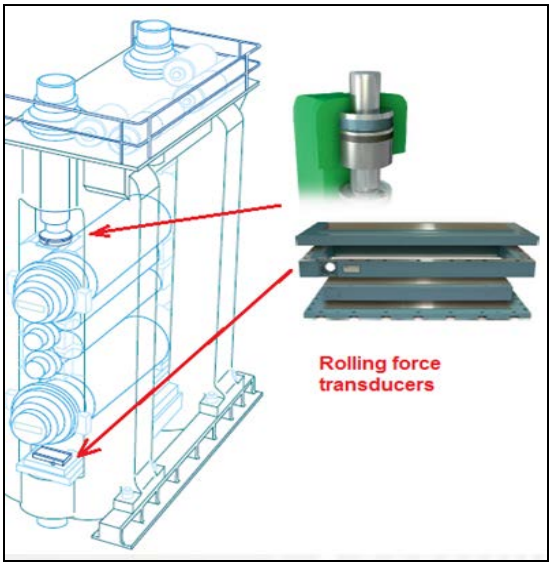

Figure 4. *ABB Rolling force transducers and their placement on the roll machine (1.6 MN to 60 MN)*

Figure 5. *Examples of extrusion presses and values*

Advantages of force measurement in metal processing

Generally compression forces are applied on the work piece by rolling, forging and pressing (forming) processes. Work piece subject to force by roller or press heads or forging hammers and its thickness reduced after every force application, so force is important for the control of the process. The advantages of force measurements in metal processing are given below:

- Increase in productivity
- Overload protection,
- Minimization of the problems which are causing from unknown forces,
- Obtaining the defined dimensions of the products, Improved product protection,
- Providing of quality standard and traceability,
- Providing of reliability in metal processing,
- Adjustment of the strain of sheet metals,
- Producing repeatable (similar technical specifications) products in different times,
- Low energy consumption due to optimum force application,
- Increasing in the usage life of processing machines such as roller, presses, extruders and hammers.
- Decreasing defects on the work pieces due to desired force application,
- Obtaining desired technical specifications from the work piece,
- Reduced energy consumption and waste.

Figure 6. *Rolling force measuring equipment*

The problems caused by uncontrolled force applications on the metal forming process

- Causing defects on the die, heads, hammers, bearings and spinning rolls of the metal forming machines due to overload force applications,

- Causing undesired product dimensions due to low or high force applications
- Causing wavy edge formations in metal sheets,
- Causing shortening of the life of machine due to overload force applications,
- Causing undesired mechanical properties in the work piece when suitable forces are not applied
- Causing cracks and microcracks on the products due to overload force application
- Metal forming processes cause some defects during process without force control.. Surface defects commonly occur due to impurities in the material, scale, rust or dirt. Internal defects caused by improper material distribution in the final products. Defects such as edge cracks, center cracks, and wavy edges are all common with metal forming processes of metal manufacturing. (8)

Force measurements in metal sheet pressing and hot or cold forging are important for high quality control, repeatability, non damaged production, low energy and for the use of time.

Figure 7. *Force applications in forging press*

Also force applications are necessary for forming metals such as in metal bending(edge bending-bending, bowingly elongation, spring back) deep drawing, stretch forming and ridge composing operations and in these operations force implementations play the leading role.

3. Traceable Force Measurements

Figure 8. *Force in stretch forming of steel sheet*

Traceable calibration of the force proving instruments are necessary and very important for reliability of the measurements. For the calibration of them, well known standard forces should be generated by force standard (calibration) machines (FSMs). Different type force standard machines are used for calibration of force proving instruments in many national metrology institutes. Decision about type selection of force standard machines directly depends on the required accuracy of force generation and budget limitation of the institute or country. The most accurate forces can be generated by dead weights with direct application. But direct application of dead weights requires considerable builting space, when capacity of forces exceeds 100 kN. Dead weight force standard machines are quite expensive due to their high production cost. Cheaper solutions can be found for establishment of force scale in the country depending on the required accuracy and capacity. Some of these solutions are lever or hydraulic amplification of dead weights and built-up force standard machines, which amplifies the forces by hydraulic ram [1-2].

In the field of force, NMIs (National Metrology Institute) and calibration laboratories in industry use force standard machines with dead-weights, hydraulic amplification, lever amplification, a reference transducer or a built-up system (BUS) to cover the force range from low to high nominal values of 1 N up to 15 MN. Already the calibration of transducers on different calibration machines can show - depending on the transducer principle and the force introduction - significant deviations up to several per cent which are related to parasitic effects from the interaction of the force or moment vector with the calibration machine and from the different loading profile of the machines and the sensitivity of the transducer to these effects. This can result in significant contributions to uncertainty in applications. The user in industry, however, has no information thus far on how to take these effects into account. Currently, the calibration result considers only the calibration and not the use of the transducer in industrial applications [3]

Solution offered for the measurement of high forces

1. With single force transducer

   The single force transducer is manufactured by the producer but higher forces over the 15 MN it has faced with traceable calibrations due to lack of higher capacities force standard machines.

2. With many transducers combining built-up force transducers

   Built-up system is good solution to reach higher forces combining 3 or 9 or 27 pieces of single calibrated transducers. For this reason, the built-up systems are getting more and more popular as it is an effective method to increase the higher ranges. Each transducer are calibrated by force calibration/standard machine to get traceability and combined in triangle form to establish built-up system.

Figure 9. *Combining three 1 MN force transducers for 3 MN built-up transducers*

For example, 3 force transducers with a nominal force of 1 MN each, it can measure compression force with a nominal force of 3 MN. Three single 1 MN force transducers are combined between lower and upper plate in triangle shape in parallel shown in Figure 9. Electrically a junction box switches the output signals of the three transducers in parallel [5].

Measurement uncertainty of the built-up system, an expanded relative uncertainty value, W, for single force transducer can be calculated [10-11]

$$w_c = \sqrt{\sum_{i=1}^{8} w_i^{\,2}} \qquad (1)$$

w1 is the relative standard uncertainty associated with applied calibration force;

w2 is the rel. std. uncertainty associated with reproducibility of calibration results;

w3 is the rel. std. uncertainty associated with repeatability of calibration results;

w4 is the rel. std. uncertainty associated with resolution of indicator;

w5 is the rel. std. uncertainty associated with creep of instrument;

w6 is the rel. std. uncertainty associated with the drift in the zero output;

w7 is the rel. std. uncertainty associated with the temperature of the instrument;

w8 is the rel. std. uncertainty associated with interpolation.

In order to develop measurement uncertainty of built-up force transducer, relative standard uncertainty associated with long-term stability of force transducer winsta should be added to the equation (1) , then relative uncertainty of single built-up force transducer, wbu-ft [12-13] can be calculated as equ. (2)

$$w_{bu-ft} = \sqrt{w_c^2 + w_{insta}^2} \qquad (2)$$

Combination of each single built-up force transducer creates built-up system (BUS) with parallel connection shown in Fig.9. Relative uncertainty can be calculated as a summation of uncertainty of single built-up force transducer. Number of single force transducer (n) can be selected as 3 or 9 or 27 according to the targeted built-up force machine capacity. The relative uncertainty of built-up system, w_{BUS} can be calculated as equ. (3). The coefficients of this fit are then multiplied by the coverage factor k =2 relative uncertainty value, W_{BUS}, for any force (F) within the calibration range.

$$w_{BUS} = \sqrt{\sum_{i=1}^{n} w_{bu-ft}^{2}} \qquad (3)$$

Expanded standard uncertainty of the built-up system (U_{BUS}) is calculated as given in eq. (4)

$$W_{BUS} = k \times w_{BUS} \quad \text{and} \quad U_{BUS} = W \times F \qquad (4)$$

In order to calibrate high range force transducer over the force scale of NMI of the country a single force transducer is calibrated using built-up system as it shown in figure 10. As a result that high capacity force measurement needed by the verification of the machines used in metal industry such as extrusion, pressing, forming and forging machines can be performed by using built-up system for traceable force measurements.

Figure 10. *Calibration of 5 MN single force transducer using 9x540 kN built-up transducer [NPL]*

3. Conclusion

The force measurements are needed in many field of industry. Especially accurate force measurements are required in many applications. A measurement technology offering high accuracy is a prerequisite today in all industry including metal industry for modern rolling, pressing and extrusion process. In order to be able to make reliable and accurate force measurements using force measuring devices, traceable calibration of them are needed and very important for reliability of the measurements. For the calibration of them, well known standard forces should be generated by force standard (calibration) machines (FSMs). Traceable force measurement can be done using built-up system in MN level forces in steel industry with 5×10^{-4} to 5×10^{-3} measurement uncertainty [11]. This cause to increasing products quality, decreasing defects on products, increasing operating safety, decreasing products cost and obtaining similar products for subsequent orders it means producing repeatable products. Traceable force measurement in MN level in steel industry causes to increase product quality and competitiveness in steel market as well.

References

[1] S.Fank, B. Aydemir, B. Force metrology Training document, TUBITAK UME, Gebze-Kocaeli,Turkey, April 2012

[2] TUBİTAK UME (Ulusal Metroloji Enstitüsü) "Meteroloji Kitabı", 1. Basım Şubat 2013, ISBN 978-975-403-731-9

[3] Dr. R. Kumme, EMRP Project document "SIB63 Force Force traceability within the meganewton range, years :2013-2016ü

[4] S.Fank, B.Aydemir "Mega Newton Seviyesindeki Kuvvetlerin Çelik Endüstrisinde Uygulama Alanları ve İzlenebilirlik İhtiyacı" Metal Dünyası Dergisi, sayı 263, Mayıs 201

[5] A. Schäfer, Increased Requirements for Higher Nominal Forces, Necessities and Possibilities to Measure Them, Sensor and Test Conference, 2011, 252-25

[6] Guide to the Measurement of Force, The Institute of Measurement and Control, 87 Gower Street London, Published in 1998, revised in 2013 ISBN 090445728

[7] Forging and Stamping Industry, The Great Soviet Encyclopedia (1979).

[8] Metal-Forging Processes and Equipment, "Manufacturing Engineering and Technology", Kalpakjian & Schmid, 6/e, 2010

[9] Prof. J.S. Colton, Lecture notes, Deformation Processing & Forging Introduction, ME 6222: Manufacturing Processes and Systems Georgia Institute of Technology, 2009

[10] INTERNATIONAL STANDARD, ISO 376- Metallic materials- Calibration of force proving instruments used for the verification of uniaxial testing machines (Fourth edition 2011-06-15)

[11] Calibration Guide, EURAMET cg-4 Version 2.0 (03/2011), Uncertaınty of Force Measurements.

[12] D.-I. Kang, H.-K. Song and J.-T. Lee, Establishment of Large Force Standards Based On Buılt-In Force Transducers and Built-Up System, XVI IMEKO World Congress, Vienna, AUSTRIA, 25 - 28 September 2000

[13] S. Fank, Li, Qingzhong, 1999, Built-up force standard machines, UME (National Metrology Institute) Force Laboratory, Gebze, Kocaeli,Turkey

International Journal of Computational and Experimental Science and Engineering (IJCESEN)
Vol. 2-No.1 (2016) pp. 38-43
http://dergipark.ulakbim.gov.tr/ijcesen

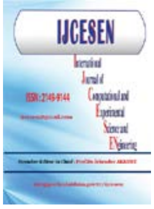

ISSN: **2149-9144**

Copyright © IJCESEN

Research Article

Calculation of measurement uncertainty for elasticity module of automobile deadening panels

Bulent AYDEMIR[1*], Sinan FANK[2]

[1]TÜBİTAK UME National Metrology Institute, Force Laboratory, Gebze-Kocaeli-TURKEY
[2]TÜBİTAK UME National Metrology Institute, Force Laboratory, Gebze-Kocaeli-TURKEY

* Corresponding Author : bulent.aydemir@tubitak.gov.tr

Presented in ”2nd International Conference on Computational and Experimental Science and Engineering (ICCESEN-2015)”

Keywords
Compression testing
Measurement uncertainty
Elasticity module

Abstract: All manufacturers need to develop their products applying test to get better performance and higher quality them before distributing the competitive market. In order to get long working life without losing performance of the materials, different tests are applied on the material to determine modulus of elasticity and rupture/deformation stresses using material testing machines. In order to develop repeatable and high quality products, test results should be known very well. The measurement uncertainty of test results should be calculated adding the all influencing parameters during tests.

In this study, parameters which have effects on the quality of compression testing are causes the increase measurement uncertainty of test results, Standard measurement uncertainty of modulus of elasticity should be calculated to give reliable results to customer.

This study details the work, findings and calculations of the measurement uncertainty of automobile deadening panels after compression testing on the material are presented. Influencing uncertainty parameters on the test results are taken into account and explained in detail.

1. Introduction

The material supply and related industries are worth trillions US $ each year over the world. In all cases, the measurement of the material properties by mechanical testing is very important for use and developing new materials.

The quality of the mechanical parts such as bolts, machines elements, aircraft parts etc. is controlled by testing the material properties (such as the tensile strength, compression strength, elasticity module, lower yield stress, proof stress, impact strength, Brinell, Rockwell and surface hardness, elongation after fracture). Each of these properties is measured according to an appropriate test method for tensile properties. [1]. Several tests are necessary during development process of the products. The compression and tensile testing are applied on the materials used in research studies, in civil engineering, military applications, materials development, automotive, ship and aircraft industry. In order to make precise and accurate compression testing, all influencing parameters on the test results must be analyzed very well. In this way, such parameters can be controlled and lower measurement uncertainty can be achieved in order to make true conformity assessment for defected parts resulting in less scrap.
For the acoustic insulation inside vehicle bodywork, specify characteristics the panel materials used. Fiat procedure specification 9.55655 is defined the modes and the equipment to be used for testing such characteristics [2]. However, the available procedure for panel materials does not provide an uncertainty budget and do not present the calculation of measurement uncertainty.

This study explains the calculations of measurement uncertainty for compression testing of panel materials. The calculation model can also be used for compression testing of all other materials.

2. Material and Test Conditions

Porous material properties and photo are given bellow [2]. The porous material specimens are prepared circular shape at diameter of 99 mm for compression test.

Table 1. Properties of porous specimens

Properties	Material	
	Porous 700	Porous 1000
Mass (g/m^2)	> 700	> 1000
Thickness (mm)	12 to 15	17 to 21

Figure 1. Test specimens

The porous material specimens were prepared mechanically in accordance with the Fiat procedure specification 9.55655 [2]. The experiments conducted with a Zwick Z250 tensile machine at the National Metrology Institute in TUBITAK. The force accuracy class of the machine was “class 0.5”

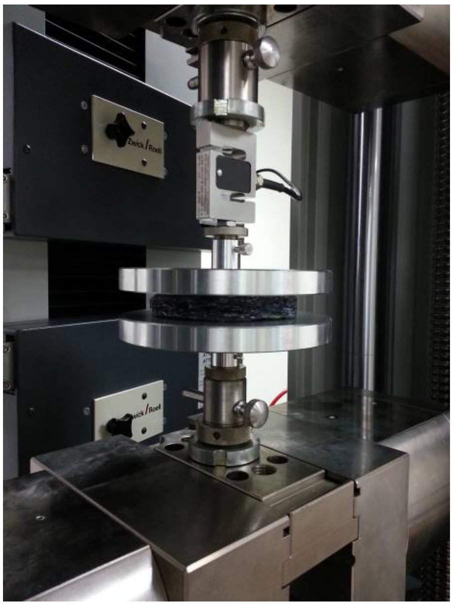

Figure 2. Test specimens, test conditions and test machine

according to EN ISO 7500-1 standard [3]. Its extensometer was used together with machine for strain measurement. The extensometer accuracy class of the machine was “class 0.5” according to EN ISO 9513 standard [4]. All tests performed at 23 ± 1°C and 50 ± 10 % humidity. The compression test was carried out with test speed of 5 mm/min.

3. Uncertainty Analysis

Material testing machine is calibrated according to EN ISO 7500-1 for requirements of its force measuring system [3]. The calibration certificates of the testing machine mentions only that they meet EN ISO 7500-1 standard requirements for force measuring system of the testing machine. This standard requires that the indication of the testing machine has to be correct to within specified limits given in those standards [5]. Adding, extensometer of material testing machine is calibrated according to EN ISO 9513 [4].

In order to determine combined uncertainty of test results of porous material or any materials first take in to account the calibration uncertainties of the testing machine used to measurement of compression force and extensometer used for measurement of thickness of tested specimens. Then, the standard deviation of the uncertainty of elasticity module measurement is calculated in the 3 test results for porous 700 materials.

Figure 3. Measurement of test specimens dimensions by caliper

Sensitivity coefficients are essentially conversion factors that allow one to convert the units of an input quantity into the units of the measured [5-9]. Sensitivity coefficients measure of how much change is produced in the measured by changes in an input quantity. Mathematically, sensitivity coefficients are obtained from partial derivatives of the model function f with respect to the input quantities. In particular, the sensitivity coefficient c_i of the input quantity x_i is given by which expresses mathematically how much f changes given an infinitesimal change in x_i [5-9].

$$c_i = \frac{\partial f}{\partial c_i} \qquad (1)$$

In this case, it can be determined the model function of the elasticity module for find to the measurement uncertainty of elasticity module as below [2];

$$E = \frac{h \bullet \Delta F}{A \bullet \Delta h} = \frac{h \bullet \Delta p}{\Delta h} \qquad (2)$$

$$\Delta P = \frac{\Delta F}{A} \qquad (3)$$

Where E is the elasticity module in N/m^2, h is sample thickness in m, ΔF is load variation on sample in N, A is sample surface in m^2, h_i is variation of h thickness due to F variation of load in m, ΔP is pressure variation of F load on sample in N/m^2.

The sensitivity coefficients, c_h , $c_{\Delta p}$ and $c_{\Delta h}$ can be obtained easily as follows:

$$c_h = \frac{\partial E}{\partial h} = \frac{\Delta p}{\Delta h} \tag{4}$$

$$c_{\Delta p} = \frac{\partial E}{\partial \Delta p} = \frac{h}{\Delta h} \tag{5}$$

$$c_{\Delta h} = \frac{\partial E}{\partial \Delta h} = -\frac{h \bullet \Delta p}{\Delta h^2} \tag{6}$$

Once, all of the values of the uncertainty contributor u_i have been estimated and reduced to one standard deviation, and the sensitivity coefficients c_i have been determined. It is usually necessary only to "root-sum-square" their products, i.e., take the square root of the sum of the squares of the uncertainty estimates multiplied by the squares of their corresponding sensitivity coefficients, in order to determine combined standard uncertainty u_c

$$u_c = \sqrt{\left[((c_1.u(x_1))^2 + ((c_2.u(x_2))^2 + ...\right]} = \sqrt{\sum_{i=1}^{N}[c_i \bullet u(x_i)]^2} \tag{7}$$

Measurement uncertainty for elasticity module (u_E) can be written as follows,

$$u_E = \sqrt{c_h^2 \times u_h^2 + c_{\Delta p}^2 \times u_{\Delta p}^2 + c_{\Delta h}^2 \times u_{\Delta h}^2} \tag{8}$$

c_h : Sensitivity coefficient for initial sample thickness measurement

$c_{\Delta p}$: Sensitivity coefficient for difference pressure measurement

$c_{\Delta h}$: Sensitivity coefficient for difference thickness measurement

u_h : Measurement uncertainty of initial sample thickness measurement taken directly from calibration certificate of extensometer of material testing machine

$u_{\Delta p}$: Measurement uncertainty of pressure measurement taken directly from calibration certificate of force of material testing machine

$u_{\Delta h}$: Measurement uncertainty of thickness measurement taken directly from calibration certificate of extensometer of material testing machine

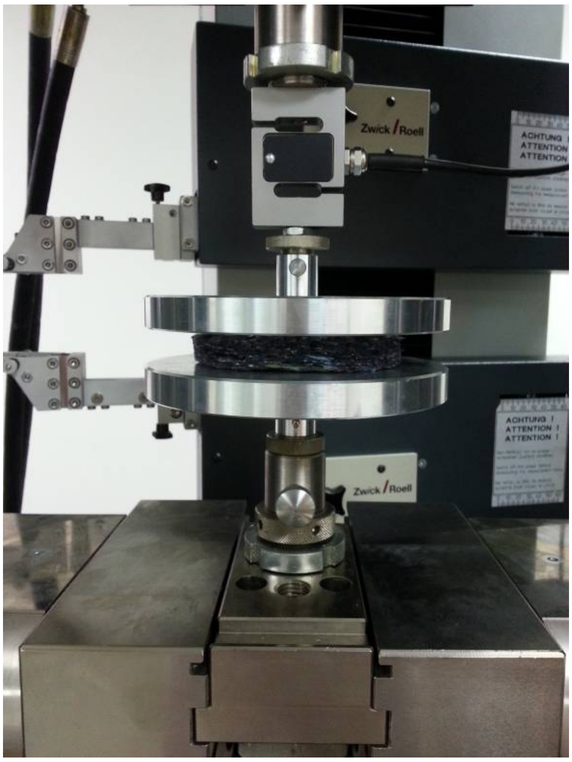

Figure 4. Measurement of test specimen during compression testing

The two error sources that are measurement of specimens' thickness and measurement of compression force have already been added into the measurement uncertainty calculations. The calculations of other effects are very difficult due to determination of all influencing parameters. Instead of uncertainty calculations for listed all error sources, the standard deviation of the test results can be used to calculation of measurement uncertainty of all other parameters mentioned in the listed error sources. The test data covers the influencing parameters. The standard deviation of test data gives the standard uncertainty of testing (u_{test}) as a combined uncertainty of the above error sources;

$$u_{test} = \frac{s_{test}}{\sqrt{n_{test}}} \tag{9}$$

S_{test} : standard deviation of the test results of five test bars for tensile strength,

n_{test} : number of test results for tested bars

$$s_{test} = \sqrt{\frac{\sum_{i=1}^{n}(X_i - \overline{X}_{test})^2}{n_{test} - 1}} \qquad (10)$$

X_i : value of the tensile strength measurement

$\overline{X}_{test}$: Average of the tensile strength measurement

Then, combined uncertainty (U_c) can be calculated the measurement uncertainty for elasticity module (u_E) and test uncertainty (u_{test}) as shown in below;

$$u_c = \sqrt{u_E^2 + u_{test}^2} \qquad (11)$$

Estimated expanded uncertainty (U_{exp}) can be calculated as;

$$U_{\exp} = k \times u_c \qquad (12)$$

4. Sample Calculations

The test result of the three test specimens tested in material testing machine are given in Table 2. The calculation of measurement uncertainties of the test results using equations from (2) to (12) are given in Table 3.

u_h and $u_{\Delta h}$ are taken from calibration certificate of extensometer of material testing machine. $u_{\Delta p}$ is also taken from the calibration certificate of material testing machine.

The average elasticity modules are 1949,03 – 3004,84 - … N/mm^2. The elasticity module and uncertainty in the result of test no 1 are shown 1949,03 N/mm^2 ± 74,09 N/mm^2.

5. Conclusion

Analysis of the uncertainty sources incorporated during measurements of the compression test of the porous material has been performed. All sources of uncertainty have been investigated in detail. Examples illustrate the importance of uncertainty sources relevant to the variability of the parameters measured from a series of tests specimens in same porous material. The test results were reported with the calculated uncertainty values, and their impact is studied. It is expected that this will provide the automotive industry with selecting better material for safety and longer life of their end product as well as conducting further improvements. Besides, the given uncertainty calculation model in the measured properties following specific test procedures can be a guide for better testing procedures.

References

[1] Evolving Needs for Metrology in Material Property Measurements, Report of the CIPM Working Group on Materials Metrology (WGMM), October 2007

[2] Fiat Group Automobiles normazione, FLAT AND PREFORMED SOUND DEADENING PANELS PROCUREMENT SPECIFICATION, 9.55655, Date:01/17/2008

[3] EN ISO 7500-1, Metallic materials – Verification of static uniaxial testing machines, Part 1: Tension/compression testing machines-Verification and calibration of the force-measuring system, 2004

[4] EN ISO 9513, “Metallic materials − Calibration of extensometers used in uniaxial testing”. 2012

[5] Room Temperature Tensile Testing: A method for Estimating Uncertainty of measurements, http://midas.npl.co.uk

[6] Aydemir, B., Fank, S., Malzeme Deneylerinde (Çekme-Eğme) Ölçüm Belirsizliğinin Hesaplanması Eğitim Dokümanı - G2KV-100, 2011, G2KV-100, Haziran 2011, TÜBİTAK UME

[7] Fank, S., Aydemir, B., Calculation of measurement uncertainty for cellulose based transformed board material in tensile testing, 2012, International Journal of Metrology and Quality Engineering, Volume 3, Issue 01, January 2012, pp 15-18

[8] Aydemir, B., Fank, S., Proficiency test report for tensile and flexural strength, 2011

[9] Aydemir, B., Fank, S., Vatan, C., Proficiency technical protocol for tensile and flexural strength, 2011

Table 2. Compression test results for porous specimens

Sample No	Test No	Load pressure	Force to be applied	Relevant thickness	Present load increments	Relevant settling increments	Elasticity Module
		p, [N/m^2]	F, [N]	h_i [mm]	Δp, [N/m^2]	Δh [mm]	E, [N/m2]
1	1	100	0,770	20,19	100	1,01	1999
	2	200	1,539	19,18	400	2,69	3002
	3	500	3,849	17,50	900	4,22	4306
	4	1000	7,697	15,97	1400	5,21	5425
	5	1500	11,546	14,98	1900	5,93	6469
	-	2000	15,395	14,26			
2	1	100	0,770	20,19	100	1,07	1887
	2	200	1,539	19,12	400	2,84	2844
	3	500	3,849	17,35	900	4,45	4083
	4	1000	7,697	15,74	1400	5,49	5149
	5	1500	11,546	14,70	1900	6,25	6138
	-	2000	15,395	13,94			
3	1	100	0,770	20,20	100	1,03	1961
	2	200	1,539	19,17	400	2,55	3169
	3	500	3,849	17,65	900	4,36	4170
	4	1000	7,697	15,84	1400	5,28	5356
	5	1500	11,546	14,92	1900	6,06	6333
	-	2000	15,395	14,14			

Table 3. Calculations of sensitivity coefficients and uncertainties of the testing

Test No	$E_{average}$	E_{STD}	u_{test}	c_h	$c_{\Delta p}$	$c_{\Delta h}$	u_h	$u_{\Delta p}$	$u_{\Delta h}$	u_E	u_C	U_{exp}
1	1949,03	57,02	32,92	97,09	19,61	-1904,04	0,10	0,50	0,01	16,98	37,05	74,09
2	3004,84	162,50	93,82	156,86	7,92	-1242,60		2,00	0,01	27,44	97,75	195,50
3	4186,34	112,20	64,78	206,42	4,63	-956,36		4,50	0,02	36,11	74,17	148,33
4	5310,01	143,98	83,13	265,15	3,83	-1014,41		7,00	0,03	46,38	95,19	190,39
5	6313,35	166,51	96,13	313,53	3,33	-1045,10		9,50	0,03	54,85	110,68	221,36

International Journal of Computational and Experimental Science and Engineering (IJCESEN)
Vol. 2-No.1 (2016) pp. 44-47
http://dergipark.ulakbim.gov.tr/ijcesen

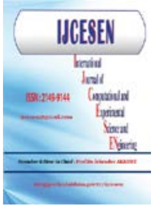

Copyright © IJCESEN

***ISSN:* 2149-9144**

Research Article

Investigation of the Effect of Cutting Parameters on the Cutting Force and Energy in the Bar Cutting Process#

Erdoğan KANCA[1]*, Mehmet DEMİR[1] and Faruk ÇAVDAR[2]

[1] İskenderun Technical University, Mechanical Engineering Department, Hatay, TURKEY
[2] İskenderun Technical University, Dörtyol Vocational School, Machinery Department, Hatay, TURKEY

* Corresponding Author : kancaerdogan@gmail.com

Presented in "2nd International Conference on Computational and Experimental Science and Engineering (ICCESEN-2015)"

Keywords
Bar Cutting
Taguchi
Cutting Force
Cutting Energy

Abstract: In this paper, cutting forces and expended energy which generated in the process of cutting the scrap bars are investigated an experimental study. Parameters affecting the cutting force is defined as cutting speed, the clearance, the cutting tool the radius, the cutting edge length and the bar diameters. In contrast to the preexisting studies is aimed to reduce the cutting forces and expended energy rather than the improvement of the cutting surface in this study. Three different levels of all five parameters are identified as variables. The number of experiments increases proportionally with the number of parameters. In order to use more parameters and perform fewer the number of experiments, this study is designed based on Taguchi L_{27} orthogonal array. The effect of these parameters which influence the cutting force on result is identified through variance analysis (ANOVA). As a result, the appropriate the cutting parameters are found by implementing verification tests.

1. Introduction

Bar cutting is a widely used metal forming processing for many years. The quality and cost of manufactured components has a direct influence on the quality of bar cutting [1]. Conventional bar cutting method has many drawback such as high cutting force, worse surface quality, lower productivity, high cost and waste of energy. To overcome these problems, optimization is emerging as a need during the bar cutting process [1-6-7]. Because bar cutting process very complicated, and energy productivity and cutting force are affected by many factors such as cutting speed [2-7], clearance [4], cutting tool of the radius [5], cutting edge length [6] and bar diameters.

Recently, researchers have shown an increased interest for the bar cutting method and its devices[1], but there is still no study optimization of cutting parameters on scrap shearing machine with the Taguchi method.

In this study, a novel advanced precision bar cutting technology, high-speed and lower energy, is proposed. The cutting force and energy productivity has been analyzed and a new kind of high-speed precision bar cutting machine has been created. The effects of process parameters on the cutting force and productivity energy of the cutting surface has been studied using both methods of Taguchi and ANOVA numerical simulation and experimental study.

2. Experimental

2.1. Materials and Equipment

The aim of this study is to design and construct a compact prototype a scrap bar cutting press which uses electric motor and mechanical re-cocking mechanism. This C type eccentric press has 50 tons capacity.

Firstly it's desired for the press to be able to work in three different speeds and to make it possible three different pulleys had been used and the velocities 120 mm/s, 270 mm/s and 325 mm/s has been obtained. Secondly the press has been designed in a way that the tables of the press can move on the three axes. Thanks to this, it is possible to set the distance between the upper and the lower cutters, modify the sensors in the body of the press and calibrate them precisely as well as fix the parallel alignment problem that occurs between the upper and the lower tables after a while on the C type presses. It's also intended to measure loads and distances in the press so a loadcell has been placed beneath the fixed cutter and a linear rule has been added to the running cutter. A pedal is used to obtain the stored energy in the flywheel when necessary. Additionally by using the pedal, the cutters are put into motion only when the cutting zone is feeded so it can act as a safety measurement as well. For every experiment conducted, a different blade profile was necessary so 27 paired, each pair got different heat treatment, blades had been manufactured.

Load stroke graphs of the each studied materials were obtained in the cutting process. Load versus strokes were measured by using a linear potentiometer and loadcell in this process, *respectively. Area under the load-strokes curve gives* energy that is needed to the cut the materials. The loadcell placed under the lower die provides the value of the load transferred to workpiece. A data logger (2000 data/second) is used so as to transfer the data from linear potentiometer and the loadcell to a computer. A schematic view of this equipment are given in Figure 1.

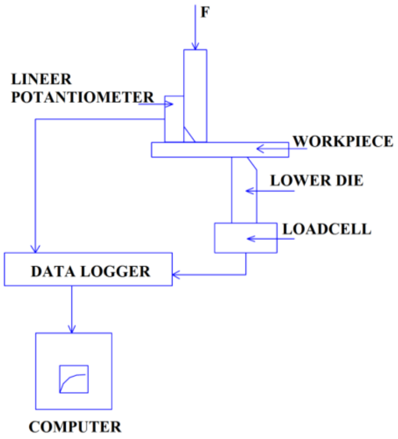

Figure 1. *A schematic view of the data logger, the loadcell and the linear potentiometer*

2.2. Taguchi Method

The Taguchi method is an extremely useful technique for the design of high quality systems, although this method is generally understood as experimental design technique. Furthermore, the Taguchi method is a systematic and efficient approach to determining optimal in terms of performance, quality, and cost during experimental configuration of design parameters [8-9].

The classic design methods are complex structure and difficult to use. In addition, increasing the number of parameters leads to an increased number of experiments. The Taguchi method has become an important method because of presenting solution the aforementioned drawbacks of the other design methods.

The parameters which influence the cutting force called control parameters such as the diameter of cut steel bars, cutting speed, clearance, the radius of the cutting tool and the cutting edge length. In this work, four controllable parameters are considered and each parameter is set at three levels. The parameters and their levels are shown in Table 1.

Table 1*.Control Parameters And Their Levels*

Levels	Speed (mm/s)	Diameter (mm)	Clearance (%)	Radius (mm)	Edge Lenght (mm)
1	120	10	5	0	4
2	270	12	10	0,5	6
3	325	14	15	1	8

3. Results and Discussion

3.1. Cutting Force

The experimental results for cutting force are shown in Table 2. In addition to, the signal-noise ratios (S/N) obtained using Eq.1 are shown in the last column.

$$S/N = -10.log(\frac{1}{n}\sum_{k=1}^{n} y_i^2) \qquad (1)$$

Fig 2. and Table 3. show the S/N ratio graphs in which the horizontal line presents the value of the total mean of the S/N ratio. Basically, if the S/N ratio is bigger, the quality characteristics for the blank is getting better. As per the S/N ratio analysis from graph the levels of parameters to be set for getting optimum value of cutting force.

Figure 2. *S-N Ratio for force*

Table 4 shows the results of ANOVA analysis. The results in this table indicate that diameter is the most effective parameter. To reduce variation, the relative power of a factor is demonstrated percent contribution. If a factor has a high percent contribution, it effects significantly performance. The percent contributions of the cutting parameters on cutting force are shown in Table.4. After the diameter, according to this, speed was found to be the major factor affecting the cutting force (6,4%). A percent contribution of clearance is lower than speed, being (4,6%). The other parameters effect too low cutting force.

3.2 Cutting Energy

Fig 3. and Table 5. show the S/N ratio graphs where the horizontal line is the value of the total mean of the S/N ratio. As per the S/N ratio analysis from graph the levels of parameters to be set for getting optimum value of cutting force.

Table 2. *Experimental results and S/N ratio*

EXPERIMENT NO	SPEED (mm/s)	DIAMETER (mm)	CLEARANCE (%)	RADIUS (mm)	LENGHT (mm)	CUTTİNG FORCE (kg)	S/N RATIO (dB)	CUTTING ENERGY (j)	S/N RATIO (dB)
1	325	10	5	0	4	1628	-64,2331	1628	-64,2331
2	325	10	5	0	6	1535	-63,7222	1535	-63,7222
3	325	10	5	0	8	1546	-63,7842	1546	-63,7842
4	270	10	10	0,5	4	1274	-62,1034	1274	-62,1034
5	270	10	10	0,5	6	1199	-61,5764	1199	-61,5764
6	270	10	10	0,5	8	1245	-61,9034	1245	-61,9034
7	120	10	15	1	4	954	-59,5910	954	-59,5910
8	120	10	15	1	6	913	-59,2094	913	-59,2094
9	120	10	15	1	8	933	-59,3976	933	-59,3976
10	325	12	10	1	4	1982	-65,9421	1982	-65,9421
11	325	12	10	1	6	1751	-64,8657	1751	-64,8657
12	325	12	10	1	8	1840	-65,2964	1840	-65,2964
13	270	12	15	0	4	1793	-65,0716	1793	-65,0716
14	270	12	15	0	6	1699	-64,6039	1699	-64,6039
15	270	12	15	0	8	1619	-64,1849	1619	-64,1849
16	120	12	5	0,5	4	1985	-65,9552	1985	-65,9552
17	120	12	5	0,5	6	1763	-64,9250	1763	-64,9250
18	120	12	5	0,5	8	1675	-64,4803	1675	-64,4803
19	325	14	15	0,5	4	2808	-68,9679	2808	-68,9679
20	325	14	15	0,5	6	2610	-68,3328	2610	-68,3328
21	325	14	15	0,5	8	2735	-68,7391	2735	-68,7391
22	270	14	5	1	4	2757	-68,8087	2757	-68,8087
23	270	14	5	1	6	2850	-69,0969	2850	-69,0969
24	270	14	5	1	8	2887	-69,2089	2887	-69,2089
25	120	14	10	0	4	2423	-67,6871	2423	-67,6871
26	120	14	10	0	6	2401	-67,6078	2401	-67,6078
27	120	14	10	0	8	2073	-66,3320	2073	-66,3320

Table 3. *S/N response table for force*

LEVEL	SPEED	DIAMETER	CLEARANCE	RADIUS	LENGHT
1	-63,91	-61,72	-66,02	-64,25	-65,37
2	-65,17	-65,04	-64,81	-65,22	-64,88
3	-65,99	-68,31	-64,23	-64,60	-64,81
Delta	2,08	6,58	1,79	0,65	0,56
	1	1	3	1	3

Table 4. *Results of the ANOVA*

	DOF	**ADJ SS**	**ADJ MS**	**F**	**P**	**PCR %**
Speed	2	632555	316277	36,86	0,0	6,4
Diameter	2	8549328	4274664	498,23	0,0	86,5
Clearance	2	463817	231909	27,03	0,0	4,6
Radius	2	19917	9958	1,16	0,338	0,2
Edge L.	2	70834	35417	4,13	0,036	0,7
Error	16	137275	8580			1,3
Total	26	9873726				100

Table 6 shows the results of ANOVA analysis. The results in this table indicate that diameter is the most effective parameter. The percent contributions of the blanking parameters on cutting force are shown in Table 6. After the diameter, according to this, speed was found to be the major factor affecting the cutting force (3%). A percent contribution of clearance is lower than speed, being (1,32%). The other parameters effect too low cutting force.

Table 5. *S/N response table for energy*

LEVEL	**SPEED**	**DIAMETER**	**CLEARANCE**	**RADIUS**	**LENGHT**
1	-30,64	-27,86	-31,96	-31,45	-32
2	-32,83	-31,22	-31,52	-32,09	-31,79
3	-31,64	-36,03	-31,63	-31,58	-31,32
Delta	2,19	8,16	0,44	0,64	0,68
	1	1	2	1	3

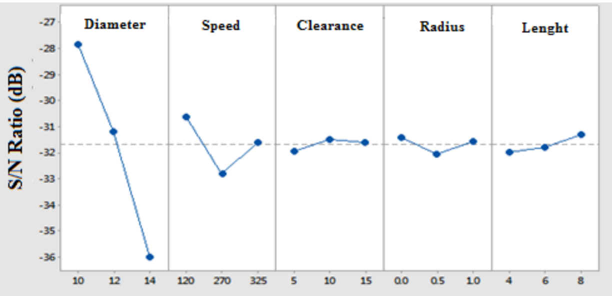

Figure 3. *.S-N Ratio for energy*

Table 6. *Results of the ANOVA*

	DOF	**ADJ SS**	**ADJ MS**	**F**	**P**	**PCR %**
Speed	2	512,41	256,2	8,39	0,003	3
Diameter	2	7261,29	3630,65	118,92	0,0	85
Clearance	2	113,54	56,77	1,86	0,188	1,32
Radius	2	96,07	48,03	1,57	0,238	1,11
Edge L.	2	51,93	25,97	0,85	0,446	0,6
Error	16	488,49	30,53			5,7
Total	26	8523,74				100

4. CONCLUSION

In this paper, experimental studies are performed to investigate the effects of some factors on the bar cutting process. These factors are the cutting speed, the clearance, the cutting tool the radius, the cutting edge length and the bar diameters, especially the cutting force and energy. The Taguchi method which benefits from the time and resources is used to achieve better results during the bar cutting process. The minimum cutting force values cutting speed of 120 mm/s, 10 mm diameter material being cut, the cut-off value of 15 % clearance, no edge radius and cutting edge length of 8 mm was observed in options. The minimum force for these parameters were found to be 871.5 kg by Minitab -17 program. Minimum cutting energy values cutting speed of 120 mm /s, 10 mm diameter material being cut, the cut-off value of 10 % clearance, no edge radius and cutting edge length of 8 mm was observed in options. The minimum energy for these parameters were found to be 12.48 j by Minitab -17 program. When the blanking speed increased, cutting force and energy increased but when the clearance decreased, cutting force and energy increased.

REFERENCES

[1] Chan, L.C., Lee, T.C., Wu, B.J., Cheung,W.M., 1998. Experimental study on the shearing behaviour of fine-blanking versus bar cropping. Journal of Materials Processing Technology, 80-81, 126-130.

[2] Marouani, H., Ismail, A., Hug, A., Rachik, M., 2009. Numerical investigations on sheet metal blanking with high speed deformation. Materials and Design, 30: 3566-3571.

[3] Quazi, T.Z., Shaikh, R., 2012. An overview of clearance optimization in sheet metal blanking process. International Journal of Modern Engineering Research (IJMER), 2: 4547-4558.

[4] Hambli, R., 2001. Blanking tool wear modeling using the finite element method. International Journal of Machine Tools & Manufacture, 41: 1815-1829.

[5] Amol, T., Rahul N., Sagar B., 2013. An overview of factors affecting in blanking processes. International Journal of Emerging Technology and Advanced Engineering. 3: 2250-2459.

[6] Chen, M., Li, H., Li, X., Liu, C., 2007. Characterization of deformation microstructure and fractured surface of plastic shearing of copper bar. Materials Science and Engineering A, 452-453,454-461.

[7] Song, j. l., Li, Y.T., Fu, J.H., Ting, K.L., 2009. Numerical simulation and experiments of precision bar cutting based on high speed and restrained state. Materials Science and Engineering A. 499, 225-229.

[8] Nalbant, M., Gökkaya, H., and Sur, G. 2007. Application of Taguchi method in the optimization of cutting parameters for surface roughness in turning. Science Direct Materials and Design, 28: 1379-1385.

[9] Taguchi, G., Elsayed, A. and Hsiang, T., 1989. Quality engineering in production system, McGraw Hill, New York.

International Journal of Computational and Experimental Science and Engineering (IJCESEN)
Vol. 2-No.1 (2016) pp. 48-51
http://dergipark.ulakbim.gov.tr/ijcesen

***ISSN:* 2149-9144**

Copyright © IJCESEN

Research Article

Characterization of Pore Structure of Different Hardened Cement Pastes[#]

Irida MARKJA[1]*, Thomas BIER[2]

[1]Polytechnic University Tirana, Square Mother Teresa nr. 4, Tirana, Albania
[2]Institute für Keramik, Glas und Baustofftechnik, Leipziger Str.28,Freiberg, Germany

* Corresponding Author : imarkja@fim.edu.al

[#] Presented in "2nd International Conference on Computational and Experimental Science and Engineering (ICCESEN-2015)"

Keywords
Cement Microstructure
MIP
Pore Structure

Abstract:
The goal of this study is to characterize the hardened cement paste at 1, 7 and 28 days using a combination of Mercury Intrusion Porosimetry (MIP), X-Ray diffraction (XRD), Thermal Analysis (TA). Hardened mortars are porous materials their pore structure being developed during hydration as a function of water binder ratio, the binder's chemical reactions and time. Different binder systems and as a consequence different chemical reactions will influence the pore structure. Systems such as Calcium Silicate Hydrate formation, Calcium Aluminate Hydrate formation are investigated with respect to the developing pore structure. MIP was used as a generally accepted technique for deriving porosity and pore size distribution and results correlated to those received from ESEM image analysis.

MIP was used as a generally accepted technique for deriving porosity and pore size distribution and results correlated to those received from ESEM image analysis.

1. Introduction

Hydration reactions are the basic processes behind the development of technological properties in cement based materials. Many of the engineering properties (as strength) are related to porosity. The results of hydration reactions are solid phases and their formation and arrangement results in changes in porosity.

Pore structure is a very important micro structural characteristic in a porous solid, because it influences the physical and mechanical properties, and controls the durability of the material. [1] Cement based materials, such as cement paste, mortar and concrete, are porous materials. The properties of porous materials are strongly affected by the characteristics of their pore system, such as porosity, pore size distribution, connectivity, etc. [2]

Sample were analysed by the following techniques:

- Strength measurement (flexural & compressive strength)
- Mercury Intrusion Porosimetry (MIP)
- X-Ray Diffraction (XRD)
- Thermal Analysis(TG-DSC).

2. Experımental

Materials and Sample preparation

The materials used in this study are Ordinary Portland Cement (*CEM I 42.5 N*), and Calcium Aluminate Cement (*SECAR 51*), Blast furnace slag cement (*CEM III B 32.5 N), *Calcium Sulfoaluminate Cement *(Calumex CSA).*Cement paste samples have been prepared with different water-cement-ratio, specifically: w/c = water demand (cf. Tab.1), w/c =0.4, w/c = 0.5. After mixing, cement pastes were cast into 40*40*160 mm prism molds and placed over water. After 24 hours, the hardened specimens were demoulded and then immersed into water. At the age 1 day, 7 days and 28 days specimens were taken out of water and crushed to a particle size of about ~2 mm for the experiments. The crushed particles were selected deliberately from the middle part of the specimens after strength testing to avoid inhomogeneity of material. The crushed samples were then put in acetone to stop the hydration process; after one hour in acetone the samples were then oven – dried at 50°C for 24 hours. [1]

Table.1 *Water demand (w/d) for the cement used in this study*

Cement	Water demand
CEM I 42.5 R	0.33
Secar 51	0.25
CSA Calumex	0.27
CEM III B 32.5 N	0.34

Characterization techniques

The *strength* of the hardened cement pastes was tested according to the German standard DIN EN 196-1.

Mercury Intrusion Porosimetry (MIP) The characterization of the pore structure of cement paste using MIP is important in understanding the mechanical and transport properties of cement paste. The pore structures obtained by mercury intrusion porosimetry can be characterized by total porosity; pore surface area and average pore diameter are calculated by measuring the amount of mercury intruded into the pore at a given pressure [1]. A PASCAL 240/440 instrument was used to carry out the measurements.

X-Ray Diffraction (XRD) Analyses were performed using a with a X'PERT Pro MPD PW 3040/60 diffractometer (PANalytical Co.) X-Ray diffraction patterns for the powdered samples were analysed with X'Pert High Score software. Quantitative analyses were made with Rietveld method.

Thermal Analysis (TG-DSC) Thermogravimetric analysis or TGA is a technique where the mass (or weight) of a material is measured as a function of temperature or time while the sample is subjected to a controlled temperature program in a controlled atmosphere [2]. Thermal analysis thermo gravimetry (TG) and DSC were conducted using a differential thermogravimetric analyzer Netzsch STA 409 PC/PG. Hydrates were estimated from the weight loss measured in the TG curve between the initial and final temperature of the corresponding DSC/TG peak. The experimental conditions involved an Argon gas dynamic atmosphere of 100 ml min^{-1}, a heating rate of 10°C min^{-1} and a platinum top-opened crucible. Alumina powder (Al_2O_3) was used as the reference material [2, 3].

3. Results

Strength measurement (flexural & compressive strength)

The strengths of four hardened cement pastes at 7days for different water to cement are shown in the Figure 1. The results show that strength decreases with increasing of water to cement ratio.

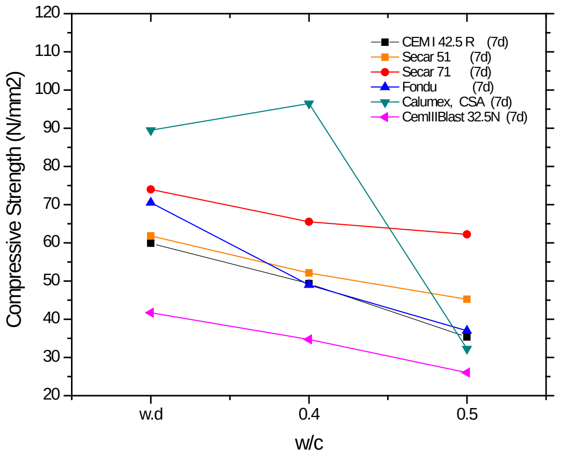

Figure 1 *The strengths of the hardened cement paste (OPC, S51)*

From the strength of each sample in Figure 1 and corresponding pore data in tab.2, it could be seen easily: though the porosity has critical effect on the strength of hardended cement paste, the differences in porosity can not exactly reveal the differences in stength.[3]

Table.2 *The pore structure of the OPC, CAC,BCF,CSA*

Hcp 7d (w/c=0.5)	Total Cumulative volume (cc/g)	Total Specfic surface area (m^2/g)	Average Pore radius (nm)	Total porosity (%)
OPC	0.182	27.69	31.71	28.81
CAC	0.131	15.77	25.46	22.36
BFC	0.224	34.43	39.64	35.74
CSA	0.086	12.56	59.13	14.79

Mercury Intrusion Porosimetry (MIP)

Corresponding pore size distributions as measured by mercury intrusion porosimetry (MIP) are depicted as cumulative distributions in figure 2 (specific volume as a function of pore radius). With increasing time of hydration the curves show for all cements a decrease in threshold radii and pore volumes.

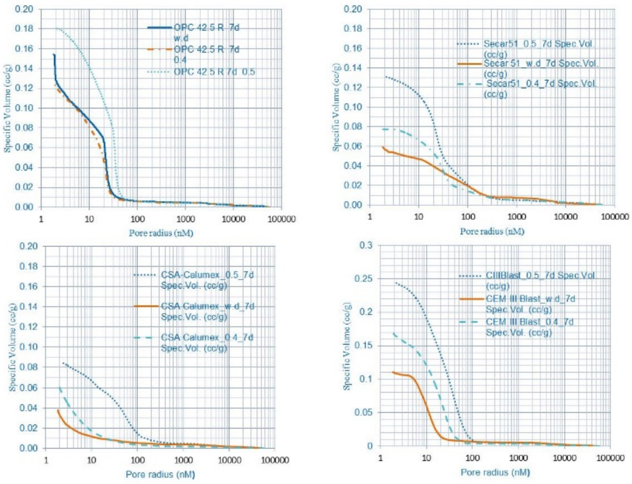

Figure.2 *Cumulative pore size distributions for different cements at 7days (w/c=0.5)*

Thermal Analysis (TG-DSC)

The test results of thermal analyses are represented in Fig.3. In each figure DSC curves are shown at the three water to cement ratios. Hydrates can be estimated from the weight loss measured in the TG curve between the initial and final temperature of the corresponding TG/DSC peak. For each curve two endothermic peaks can be observed up to about 500°C.

The first peak at around 100-120°C is present in each sample and can be associated to CSH and/or ettringite.

The second endothermic peak which was observed for OPC at 450°C can be linked to CH; the one for CAC at 300°C can be associated to CAH and/or AH_3; for BFS at 420°C to CH and for CSA the presence of $Al(OH)_3$ at 280°C is observed [4].

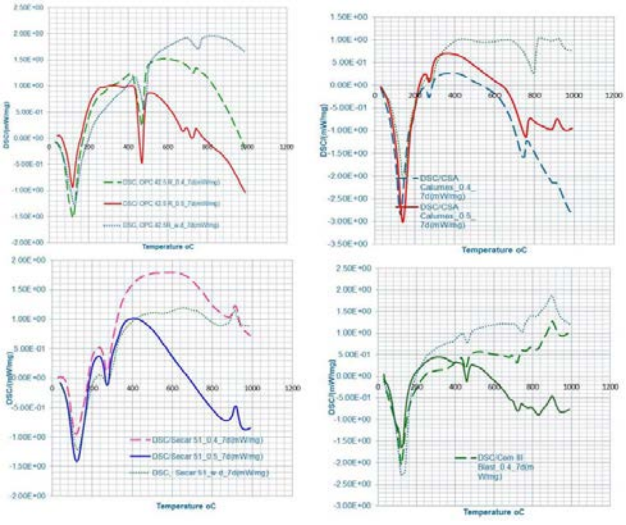

Figure.3 *DSC curves for hardened cement paste for w/d, 0.4, and 0.5 for 7days*

X-Ray Diffraction (XRD)

The hardened cement paste microstructure is examined and XRD patterns are represented respectively in figures 4.

4. Conclusion

From the standpoint of strength, the water/cement ratio porosity relation is undoubtedly the most important factor because it affects the porosity of the cement paste; and we can see from the results that the compressive strength depends on porosity of the materials; we see that the strength decreases with the increasing of water to cement ratio. In addition, the thermal analyses TG-DSC can show the consecutive peaks from each system; is a technique in which the mass of a substance is monitored as a function of temperature or time as the sample specimen is subjected to a controlled temperature program in a controlled atmosphere.

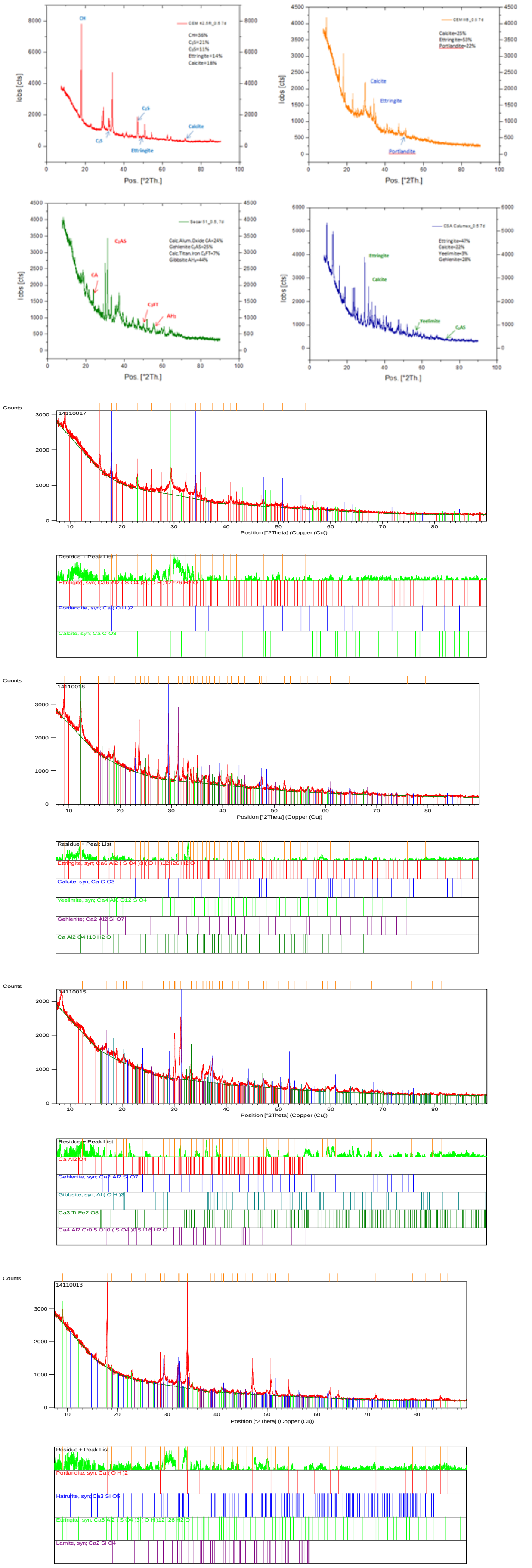

Figure.4 *XRD patterns for Cem III Blast, CSA Calumex, Secar 51, CEM I 42.5 R*

And we can compare the results from XRD pattern analyzing from High Score with TG-DSC results. TG/DSC curves (together XRD) allowed to characterize hydrates formed.

Results from MIP basically show low pore volumes with decreasing water to cement ratio for each cement paste series. However, they show very different shapes for pore size distribution curves (fingerprints) for the four different cement paste systems investigated.

Acknowledgement

Special thanks to Prof. Dr. Thomas BIER. I would like to acknowledge his support and encouragement. And the German Academic Exchange Service – DAAD.

References

[1] Xudong Chen*, Shengxing Wu, Jikai Zhou, Influence of porosity on compressive and tensile strength of cement mortar, Construction and Buildings Materials 40 (2013) 869-874,

[2] Keisuke Takahashi, Effects of Mixing and Pumping Energy on Technological and Microstructural Properties of Cement-based Mortars, 2014

[3] Zh.Wensheng, L.Beixing, W.Hongxia, W.Jiangxiong, Ch.Yimin, Analysis of pore structures and their relations with strength of hardened cement paste

[4] M. Marroccoli, F. Montagnaro,Hydration Properties of Calcium Sulphoaluminate Cements made from Coal Combustion Wastes.

International Journal of Computational and Experimental Science and Engineering
(IJCESEN)
Vol. 2-No.1 (2016) pp. 52-55
http://dergipark.ulakbim.gov.tr/ijcesen

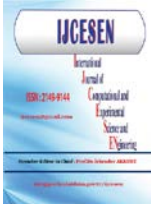

***ISSN:* 2149-9144**

Copyright © IJCESEN

Research Article

Bandwidth Enhancement of Equilateral Triangle Microstrip Patch Antenna with Slot Loading and Dielectric Superstrate[#]

Dilek UZER[1]*, S. Sinan GÜLTEKİN[1], Emrah UĞURLU[2], Özgür DÜNDAR[3], Rabia TOP[1]

[1]Selcuk University, Electrical and Electronics Engineering Department,42250, Konya-Turkey
[2]Third Main Jet Base, Konya-Turkey
[3]Necmettin Erbakan University, Ereğli Kemal Akman Vocational High School,42310, Konya-Turkey

* Corresponding Author: dilek_uzer@selcuk.edu.tr

[#] Presented in "2nd International Conference on Computational and Experimental Science and Engineering (ICCESEN-2015)"

Keywords
Triangular microstrip antenna 1
Bandwidth enhancement 2
HFSS 3
Slot loading 4
Dielectric superstrate 5

Abstract: In this study, effects of slot loading and dielectric superstrate techniques, which are the common bandwidth enhancement techniques in literature, are investigated on an equilateral triangle microstrip patch antenna. From these techniques, slot loading is realized by etching parts with various shapes and dimensions from the patch surface without disturbing the integrity. Dielectric superstrates can be chosen with the same or different from the substrate material of the antenna that have the same dimensions with the substrate and cover the whole patch surface. First, these bandwidth enhancement techniques are applied one by one, then with together on the microstrip patch antenna. The antenna is designed on FR-4 and simulated by HFSS. As slot shapes, Parallel (P), U and O slots are preferred. As superstrate, it is chosen with the same substrate specifications and dimensions. After, parameters of the slots are changed systematically, one parameter in each step and the others are fixed, and the parametric analysis is completed. As a result of this analysis, the optimum dimension, shape and superstrate combinations are found that given the best values for both frequencies and bandwidths. This combination is using with P-slot and superstrate together and this design gives the frequencies and the bandwidths, 1730MHz and 2460MHz, % 2.89 and % 2.03, from simulations, 1840MHz and 2530MHz, %3.804 and % 1.581, from measurements, respectively. In addition, it is seen that simulation and experiment results are compatible with each other.

1. Introduction

Microstrip patch antennas have lots of advantages but, they have very narrow bandwidths which is an undesired feature for present wireless and mobile antenna applications. [1,3]. For this reason, there are most studies on searching new, effective and easy applicable bandwidth enhancement methods [1-14]. The common of these methods are; slot loading on patches [1-7], superstrate adding, using thicker substrates that have lower dielectric constant and using matching networks, etc. [1-17]. From these methods, the simplest and easy applicable ones that after the patch is produced are slot loading and superstrate adding [6,7,10,12]. In slot loading, the aim is extending the current path on the patch surface and resonating the antenna at a lower frequency with the same dimensions.

Similarly, if a superstrate is added on a patch antenna, due to the superstrate specifications, the resonant frequency and bandwidth of the antenna can be changed easily. 1,2,6,7,13].

In here, on triangular microstrip Patch antennas, P, U and O slot adding were realized and superstrate addition was realized on the slotted patches. The slot parameters were tried to determine for bandwidth optimization. Simulation and measurements of the designs were completed in laboratory. In the next sections, the study steps will be explained.

2. Antenna Design

The antennas were designed on FR-4 materials that has a dielectric constant of 4.4 and a thickness of 1.6mm, two faces covered with a 35µm- thickness copper plates. The design frequencies are about 1800MHz and 2400MHz, they could be changed due to the slot dimensions and types. As previous, a simple, no slot antenna was designed. HFSS was used for the simulations [18]. By simulation, the feed point of the antenna was determined, then the antenna was produced with a PCB prototyping machine and measured using a network analyzer. The results of the simple antenna were a pioneer for the later studies. The design of the antenna without slots and with superstrate is given in Figure 1.

2.1 Slot loading

In this step of the study, an equilateral triangular microstrip patch antenna was designed by using parameters from [14]. After simulations and experiments were completed, the return loss results were used for determining the resonant frequency and bandwidth of the antennas. Afterwards, with new P-slot parameters were determined with HFSS simulations and the new antennas were produced. The P-slots were transformed to U-slots and the last slot type, O-slot was applied the antennas. Measurements were repeated for all these new antennas. The new antenna parameters can be seen from Table 1.

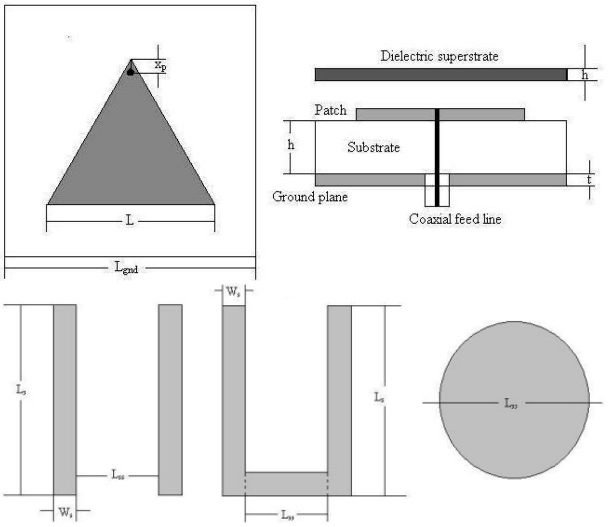

Figure 1. *Microstrip Patch Antenna, with Superstrate Addition and Slot Types*

In the next step, designs with U and O-slots which are common in literature were realized like seen from Figure 1. The U-slots were obtained from the P-slot designs by unifying the two vertical slots with a horizontal slot that has the same width with the other slots and a length named as L_{SS}. For these slot type designs, only two designs that gave the best simulation results were produced and measured.

Table 1. *Antenna Parameters and Results for Antennas with P-Slots from [14]*

No	L_s	W_s	L_{ss}	x_p	L	L_{gnd}	h	ε_r	t
1	17	1	22	20,4	50	75	1,6	4,4	0,035
2	19		18	19,6					
3	21		18	18,7					
4	23		18	18,0					
5	23		16	19,0					
6	23		14	19,8					
7	30		10	21,2					

No	$f_{r1[14]}$	$f_{r1\_sim.}$	$f_{r1\_meas.}$	$f_{r2[14]}$	$f_{r2\_sim.}$	$f_{r2\_meas.}$
1	1838	1750	1920	2743	2480	2750
2	1863	1780	*	2674	2570	*
3	1800	1760	1870	2572	2520	2590
4	1754	1780	1830	2486	2670	2530
5	1802	1790	1860	2552	2550	2550
6	1844	1810	1980	2580	2730	2560
7	1740	1720	2010	2365	2730	2410
No	**BW_1 [14]**	**BW_1 sim**	**BW_1 meas**	**BW_2 [14]**	**BW_2 sim**	**BW_2 meas**
1	1,400	1,714	0,129	1,300	2,016	*
2	1,500	1,685	*	1,300	1,946	*
3	1,600	2,273	0,128	1,400	1,984	1,931
4	1,700	2,247	0,150	1,500	1,498	1,976
5	1,800	2,235	2,151	1,700	1,961	1,176
6	1,800	2,210	11,616	1,700	1,961	1,953
7	1,900	2,210	10,945	1,700	1,961	2,490

Here, all dimensions are in mm, all frequencies are in GHz and all bandwidths are in %.

Where;
U: U-slot design,
O: O-slot design,
P: P-slot design,
L_s: Vertical slot length or the diameter of the O-slot,
W_s: Slot width,
L_{SS}: Horizontal slot length or the distance between Parallel slots,
x_p: The feed point,
L_{gnd}: The ground plane length,
L: The length of triangular patch,
h: The substrate and the superstrate thickness,
ε_r: the dielectric constant of the substrate and the superstrate,
t: the thickness of the copper plates.

2.2 Superstrate addition

In the next step, a superstrate that has the same specifications with the dielectric substrate of the antennas was added on various types slotted microstrip patch antennas. The simulations and experiments were repeated for these superstrated antennas. The antenna design with superstrate can be seen in Fig.1 and 2.

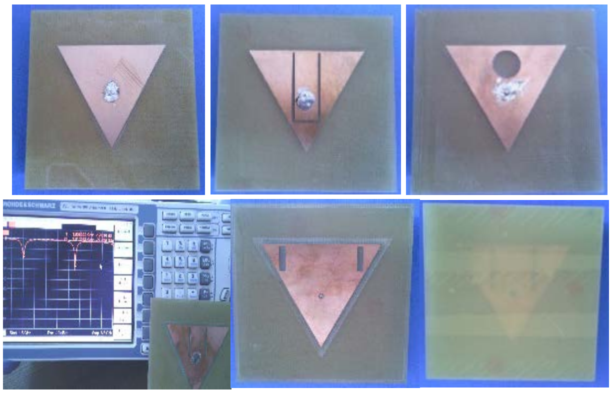

Figure 2. *Application of Designed Microstrip Patch Antennas*

Table 2. *Results for Antennas with P-Slots from [14] added Superstrate*

No	$f_{r1\_sim.}$	$f_{r1\_meas.}$	$f_{r2\_sim.}$	$f_{r2\_meas.}$
1	1710	1870	2410	2680
2	1670	*	2180	*
3	1720	1810	2480	2520
4	1660	1770	2310	2470
5	1670	1800	2320	2450
6	1700	1840	2350	2060
7	1710	2030	2450	2300
No	$BW_{1\_sim.}$	$BW_{1\_meas.}$	$BW_{2\_sim.}$	$BW_{2\_meas.}$
1	2,924	0,128	*	*
2	*	*	2,294	*
3	1,163	0,165	2,016	1,984
4	1,807	0,168	2,165	2,024
5	2,395	1,667	2,155	1,224
6	2,353	1,630	1,702	11,165
7	2,339	11,823	1,224	3,478

3. Results

In this study, a simple equilateral triangular microstrip patch antenna, without any slot, based on antenna parameters from [14], was designed and it was seen that, adding various types of slots on a simple patch can cause more than one or two resonant frequencies different from the design frequency. So the impedance bandwidth of the antenna can be enhanced by this method.

When a superstrate was added on the slotted patch, the first resonant frequency became higher, the second resonant frequency became lower and the first and the second bandwidths became larger than previous designs.
New simulation and measurement results for P-slot designs are given in Table 3. The best results were obtained with the design of using P-slot and superstrate together.

Table 3. *Simulation and Experimental Results of Microstrip Patch Antennas with Slots and Superstrate*

No	Slot Type	L_s	W_s	L_{ss}
1	No Slot	*	*	*
2	U	30	1	10
3	O	*	*	6.5
4	P	22	1	11

No	Slot Type	f_{r1sim}	f_{r1meas}	f_{r2sim}	f_{r2meas}
1	No Slot	1840	1940	*	2080
2	U	1720	1770	3030	3120
3	O	1830	1890	*	*
4	P	1820	1830	2660	2080
No	**Slot Type**	BW_{1sim}	BW_{1meas}	BW_{2sim}	BW_{2meas}
1	No Slot	1,087	4,639	*	2,404
2	U	2,326	2,260	1,650	1,282
3	O	2,186	7,513	*	*
4	P	2,747	3,279	1,880	4,808
No	**Superstrate & Slot Type**	$f_{r1\_sim.}$	$f_{r1\_meas.}$	$f_{r2\_sim.}$	$f_{r2\_meas.}$
1	No Slot	1770	1930	3100	3390
2	U	*	1720	2670	2040
3	O	1740	1870	3130	3360
4	P	1730	1840	2460	2530
No	**Superstrate & Slot Type**	$BW_{1\_sim.}$	$BW_{1\_meas.}$	$BW_{2\_sim.}$	$BW_{2\_meas.}$
1	No Slot	*	1,554	2,258	2,065
2	U	*	2,326	1,873	8,333
3	O	1,724	2,139	1,278	0,893
4	P	2,890	3,804	2,033	1,581

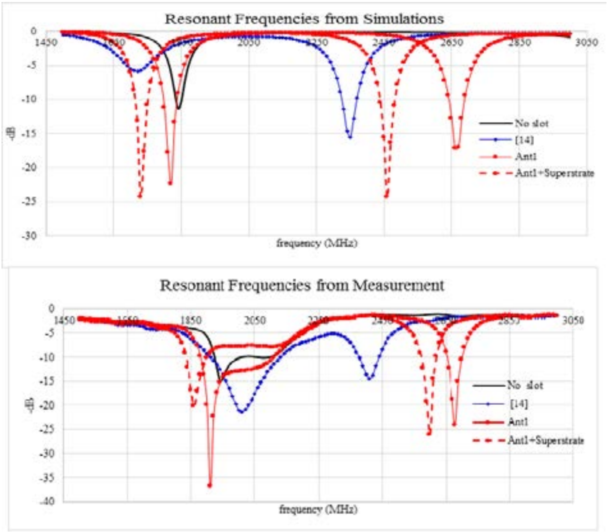

Figure 3. *Comparison of Resonant Frequencies from Simulations and Measurements*

Most of the antennas had a larger value from experimental results than simulation calculations. Experimental and simulation results were compatible with each other in an acceptable degree while the impedance bandwidths showed an increase more than two times of the simulation results.

4. Conclusion

In this study, two common bandwidth enhancement methods in literature are applied to equilateral triangular microstrip patch antennas. One of the methods is slot loading and the other one is adding superstrate. The reason of choosing these methods are that they can applied after the patch antenna produced, easily. These methods are applied to the antennas one by one, then with together. It can be said that using more than one bandwidth enhancement method is more effective. In the study, various types of slots are used for comparison of different slot type effects on resonant frequency and bandwidth of the antennas. The best results are obtained by etching P-slots on the antenna than adding a superstrate with the same dielectric substrate specifications. Simulation and experimental results of the study are compatible. There is small shifting between some of simulations and measurements because of not optimizing the slot and superstrate parameters at the same time, but one after another. More different slot shapes and different superstrates can be applied to microstrip antennas in the next studies. As another topic, the effects of the slot and supertstrate parameters on antenna bandwidth and frequency will be investigated with together in the near future.

References

[1] Garg R., P. Bhartia, I. Bahl, A. Ittipiboon, Microstrip Antenna Design Handbook, Artech House, MA, USA, 2001.

[2] Wong K.L., Compact and Broadband Microstrip Antennas, John Wiley and Sons Inc., 2002.

[3] Balanis C.A., Antenna Theory, Analysis and Design, John Wiley and Sons Inc., 2005.

[4] Kumar G., and K.P. Ray, Broadband Microstrip Antennas, Artech House, Waterhouse, R.B., 2002.

[5] Jackson D.R., Antenna Engineering Handbook, University of Houston the McGraw-Hill Companies, Chapter 7 - Microstrip Antennas, 7-20, 2007.

[6] Siakavara K., “Methods to Design Microstrip Antennas for Modern Applications”, Microstrip Antennas, Prof. Nasimuddin Nasimuddin (Ed.), ISBN: 978-953-307-247-0, InTech, 2011. Available from: http://www.intechopen.com/books/microstrip-antennas/methods-to-design-microstrip-antennas-for-modernapplications

[7] Uzer D., “Investigation on Favorable Methods for Wideband Microstrip Patch Antenna Designs”, Ph.D. Thesis, The Graduate School of Natural and Applied Science of Selcuk University, (in progress)

[8] Wong K.L. and W.H. Hsu, “Broadband Triangular Microstrip Antenna with U-Shaped Slot”, Electron. Lett., vol. 33, (Dec. 4, 1997) 2085-2087. DOI: 10.1049/el:19971472

[9] Lee K.F., S. Lung, S. Yang, A.A. Kishk and K.M. Luk, “The Versatile U-Slot Patch Antennas”, IEEE Antennas and Propagation Magazine, Vol. 52, 1, (2010) 71-88. DOI: 10.1109/MAP.2010.5466402

[10] Luk K.M., K.F. Lee, and W. Tam, “Circular U-Slot Patch with Dielectric Superstrate”, Electron. Lett., Vol. 33, No. 12, (1997) 1001–1002. DOI: 10.1049/el:19970701

[11] Deshmukh A. A., and G. Kumar, “Various Slot Loaded Broadband and Compact Circular Microstrip Antennas”, Micr. and Opti. Tech. Lett., Vol. 48, No. 3, (Mar. 2006) 435–439.DOI: 10.1002/mop.21373

[12] Ramahi O.M. and Y.T. Lo, “Superstrate Effect on the Resonant Frequency of Microstrip Antennas”, Microwave Opt. Technol. Lett. Vol.5, (June 1992) 254-257.DOI: 10.1002/mop.4650050603

[13] Bhattacharyya A. and T. Tralman, “Effects of Dielectric Superstrate on Patch Antennas”, Electron Lett., Vol.24, (Mar 1998) 356-358.

[14] Fang S.T. and K.L. Wong, “A Dual-Frequency Equilateral-Triangular Microstrip Antenna with A Pair of Narrow Slots”, Microwave and Optical Technology Letters / Vol. 23, No. 2, (October 20 1999) 82-84.DOI: 10.1002/(SICI)1098-2760(19991020)23:2<82: AID-MOP6>3.0.CO;2-T

[15] Dahele J.S., and K.F. Lee, “On the Resonant Frequencies of the Triangular Patch Antenna”, IEEE Trans. Antennas Propagat., Vol.35, (1987), 100-101. DOI: 10.1109/TAP.1987.1143960

[16] Chen W., K.F. Lee, and J.S. Dahele, “Theoretical and Experimental Studies of the Resonant Frequencies of the Equilateral Triangular Microstrip Antenna”, IEEE Trans. Antennas Propagat., Vol.40, (1992), 1253-1256.DOI: 10.1109/8.182460

[17] Wong K.L., M.C. Pan, and W.H. Hsu, “Single-Feed Dual-Frequency Triangular Microstrip Antenna with A V-Shaped Slot”, Microwave Optical Technol. Lett. 20 (Jan. 20, 1999),133–134. DOI: 10.1002/(SICI)10982760(19990120)20:2<133: AID-MOP16>3.0.CO;2-9

[18] ANSYS HFSS v14, www.ansys.com